UNIVERSITÀ DEGLI STUDI DI CATANIA
FACOLTÀ DI SCIENZE MATEMATICHE, FISICHE E NATURALI
DOTTORATO DI RICERCA IN FISICA

DARIO NICOLOSI

EVIDENCE OF NUCLEAR RAINBOW IN THE $^{16}O + {}^{27}Al$ ELASTIC SCATTERING @ 280 MEV

PH.D THESIS

PH.D COORDINATOR: PROF. F. RIGGI
TUTOR: PROF. F. CAPPUZZELLO
CO-TUTOR: DR. D. CARBONE

XXVI CICLO 2010-2013

Quando le persone care ci lasciano,
non so realmente dove vanno.
Ma so perfettamente dove restano.
Ciao nonno...

Quando la tempesta sarà finita,
probabilmente non saprai neanche tu
come hai fatto ad attraversarla
e ad uscirne vivo.
Anzi, non sarai neanche sicuro
se sia finita per davvero.
Ma su un punto non c'è dubbio.
Ed è che tu, uscito da quel vento,
non sarai lo stesso che vi è entrato.
Haruki Marukami

Contents

List of Figures

List of Tables

Chapter 1

Introduction

Rainbow is the term which indicates the coloured arc seen in the sky during the rain when the sunlight is not completely obscured by the clouds. This atmospheric phenomenon attracted the interest of many scientists during the decades, and a meaningful theory of the rainbow was developed only recently [7]. Nowadays, it is well known that the processes that led to the formation of this bright arc in the sky are connected to the wave nature of the light and involve absorption-free processes, in particular the refraction-reflection-refraction mechanism undergone by a light ray when it enters a raindrop.

From the nuclear physics point of view, it is well known that nuclei can display wave properties, since they can be diffracted, refracted and be subject of interference. If the elastic scattering process is investigated, and a system characterized by a small absorption is chosen, then, maintaining the similarity with the atmospheric case, it is possible to look for a "rainbow" also in the nuclear case.

The first attempts in this direction were realized by Goldberg *et al.* [4, 8, 9], considering the elastic scattering process of alpha particles on different nuclei. In the measured elastic cross section angular distributions, a clear evidence of a well developed nuclear rainbow was observed for the first time. In the measured distributions, in fact, a huge bump in the elastic cross section at the largest scattering angles was observed, and a behaviour of the data similar to the square of the Airy function, adopted to describe the atmospheric rainbow, was identified. The enhancement of the elastic cross section at the largest scattering angles is what now is commonly referred to as nuclear rainbow. Several years later, the rainbow phenomenon was observed in heavier systems, like the

elastic scattering of ^{12}C on ^{12}C [10–12] and ^{16}O on ^{16}O [1, 13, 14]. The latter represents one of the best systems in which a fully developed rainbow structure has been observed in a wide range of incident energies. Anyhow, the strong absorption which acts when two heavy nuclei come in close contact tends to hide the refractive component of the scattering process. As a consequence, nuclear rainbows were thought to be very difficult to be observed in systems heavier than ^{16}O + ^{16}O.

It is clear that the nuclear potential is the key quantity to deal with for the understanding of this particular feature of the nuclear scattering process. The interaction potential *U(R)* among the colliding partners can be expresses as the sum of a real part *V(R)*, describing the elastic scattering mechanism, and an imaginary part *W(R)*, which takes into account all those processes which remove flux from the elastic channel. Therefore, only those system for which *V(R)* is the dominant contribution of the overall potential *U(R)* will have some chance to manifest a rainbow pattern when the elastic scattering is investigated. At the same time, the observation of a rainbow mechanism in the elastic angular distribution gives access to the real part of the nuclear interaction, allowing its investigation at small distances, where a deep overlap among the nuclear densities of the colliding nuclei is reached. Thus, it becomes evident how the observation of a nuclear rainbow pattern when dealing with an elastic scattering process can provide very useful, precise and, to some extent, unexpected information about the nuclear structure.

In the present work the ^{16}O + ^{27}Al elastic scattering process at an incident energy of 280 MeV is presented. It is organized as follows. In Chapter 1, a general overview of the rainbow phenomenon is given, treating both the atmospheric and the nuclear case. The latter is discussed in details, showing, in particular, the central role of the optical potential for a good comprehension of the phenomenon. It is shown how the conventional approach of the optical model analysis based on a Wood-Saxon shape for the interaction potential is replaced by a more sophisticated description based on the double folding model of the real potential. In this model, the nucleus-nucleus interaction is described in terms of realistic wave functions for the projectile and the target and is strongly dependent on a proper choice of the effective in-medium nucleon-nucleon interaction. This will be shown to be the link between the nuclear rainbow and the equation of state (EOS) of cold nuclear matter.

A description of the theoretical approach used for the data analysis is given in Chapter

2. The experimental elastic angular distributions are compared with a new generation of parameter-free calculations based on the Coupled Channels (CC) formalism [15], using the São Paulo potential (SPP) [16]. This is nothing else but a particular version of the double folding approach for the optical potential, in which the effect of the Pauli non locality is taken into account through a velocity-dependent exponential factor. The SPP/CC model was successfully tested for different systems (^{16}O + ^{27}Al, ^{58}Ni, ^{60}Ni, ^{58}Ni + ^{124}Sn, ^{6,7}Li + ^{120}Sn) in a wide energy range. In particular, for the ^{16}O + ^{27}Al system, the experimental fusion, deep-inelastic and quasi-elastic cross sections are in agreement with the theoretical calculations for $E_{lab}(^{16}\mathrm{O}) < 90$ MeV. Moreover, the SPP/CC calculations predict [17] a nuclear rainbow pattern in the angular distribution for the elastic scattering of ^{16}O on ^{27}Al at 100 MeV (or higher) incident energy, which is strongly connected to the coupling with low-lying target excitations. This is to some extent a surprising result, since, due to the strong absorption, no rainbow features are expected for such a heavy-ion system.

In order to verify these theoretical predictions, an ^{16}O + ^{27}Al elastic scattering experiment was recently performed at the INFN-LNS in Catania, using an ^{16}O beam delivered by the TANDEM accelerator at 100 MeV incident energy. Evidences of nuclear rainbow formation were recognized in the experimental elastic angular distribution of the investigated system. This experiment represents the guideline for the further investigation of the ^{16}O + ^{27}Al reaction at 280 MeV discussed in the present work.

The MAGNEX magnetic spectrometer [18], whose characteristics and principle of operation are described in detail in Chapter 3, is the experimental device used to perform the investigation of the ^{16}O + ^{27}Al system. The experiment was performed at the Catania LNS-INFN laboratory using a 280 MeV energy ^{16}O Cyclotron beam impinging on a 109 μg/cm^2 thick ^{27}Al target. The ejectiles were momentum analysed by MAGNEX and detected by its Focal Plane Detector (FPD) [19]. Five different angular settings were chosen, with the spectrometer optical axis located at $\theta_{lab}^{opt} = 10°$, 13°, 18°, 26° and 34° in the laboratory reference frame with respect to the beam direction. Due to the large angular acceptance of MAGNEX (-0.090 rad, +0.110 rad horizontally, ±0.125 rad vertically in the spectrometer reference frame), these settings cover a whole angular range of about $5° \leq \theta_{lab} \leq 40°$.

Chapter 4 is devoted to the description of the adopted data reduction technique. This is a very complex procedure made up of several steps. The first one consists in the

identification of the ^{16}O ejectiles, since the ^{27}Al(^{16}O,^{16}O)^{27}Al reaction is studied. The identification procedure is based on the standard $\Delta E - E$ technique for the atomic number (Z), while the mass number (A) is determined by the correlation between the measured ion positions at the focus and its kinetic energy. Once the ions track are measured at the focal plane position, it is possible to optimize the spectrometer transport map up to the 10^{th} order. The whole procedure completely characterizes the investigated event, providing the ion kinetic energy and scattering angle in the laboratory reference frame. Starting from these quantities, the excitation energy spectra and angular distributions of the ^{27}Al target are constructed. Spectra up to 85 MeV excitation energy were extracted, showing the population of the ground state and low-lying excited states of the residual nucleus. In particular, the spectra obtained in the $\theta_{lab}^{opt} = 10^{\circ}$ configuration show the population of large structures in a narrow angular range at relatively-high excitation energy, corresponding to the excitation of collective modes of the target nucleus, i.e. Giant Resonances. These modes were observed also in the past in the ^{24,25,26}Mg and ^{27}Al inelastic α scattering [20].

In the final chapter the experimental findings are discussed. A model-independent analysis is presented, showing how the measured elastic angular distribution manifests a rainbow pattern at the largest scattering angles, since the data definitively deviate from the exponential decrease characterizing a strong absorptive system. Then the results of the comparison of the data with the SPP/CC calculations are discussed, both for the elastic and the inelastic distributions. The calculations were performed using the computer code FRESCO [21], which is described in some details. It is shown how the standard rotational model, adopted in the code to describe the coupling potential among the states of the projectile and the target, is not suitable in the case of the ^{27}Al target. Instead, a better agreement with the data is obtained when the weak coupling model [22] is used. Within such a model, the ^{27}Al ground state and the first low lying excited states ($1/2^+$, $3/2^+$, $5/2^+$, $7/2^+$, $9/2^+$) are described as a $1d5/2$ proton hole coupled with the ^{28}Si 0^+ ground state and 2^+ (1.779 MeV) excited state, respectively. Finally, the huge bumps and the broader structures observed in the ^{27}Al excitation energy spectrum measured at forward angles are discussed. These excitations of the target nucleus appear in an energy region which is compatible with the population of the Giant Monopole and Quadrupole Resonances, and their effect can play an important role in the calculation of the theoretical elastic and inelastic distributions.

Chapter 2

The physics of the rainbow

2.1 Atmospheric rainbow

The term "rainbow" is commonly associated with the atmospheric phenomenon observed in the sky during the rain when the sunshine is not completely obscured by the clouds. The scientific description is often supposed to be a simple problem in geometrical optics: actually, this is not the case, since a satisfactory quantitative theory of the rainbow has been developed only in the past few years and involves a deep knowledge about the nature of light.

The single bright arc seen after a rain shower or in the spray of a waterfall is the primary rainbow. Due to the wavelength dependence of the refractive index, the white sunlight is splitted into its constituent spectral colours: in the primary bow the same sequence is always observed, with violet innermost and red outermost. Higher in the sky than the primary bow is the secondary one, in which the colors appear in reversed order. Careful observation reveals that the region between the two arcs is considerably darker than the surrounding sky. Even when the secondary bow is not clearly seen, the primary one shows a lighted side and a dark side. The latter has been given the name Alexander's dark band, since the Greek philosopher Alexander of Aphrodisias, who first described it in about A. D. 200.

Historically, the first attempt to rationally explain the appearance of the rainbow was made by to Aristotle, who described the phenomenon as due to the reflection of sunlight by the clouds. He correctly explained the circular shape of the bow through the reflection of the light at a fixed angle and perceived that this arc is not a fixed material

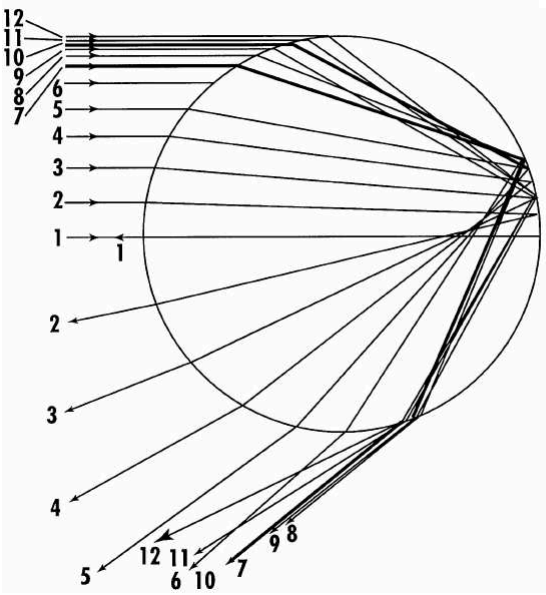

Figure 2.1: Schematic description of the primary rainbow formation. The paths of several light rays entering a spherical droplet with different impact parameters are schematically drawn. The ray numbered 7 is the rainbow ray and defines the minimum angle of deflection in the primary bow (around 42°).

object with a definite location in the sky but rather a set of directions along which light is strongly scattered into the eyes of the observer.

The first modern explanation of the atmospheric rainbow was given by Descartes in 1637 in his book *Les Meteores*. Descartes showed that the primary rainbow is made up of rays entering a water droplet and reflected once from the inner surface. The secondary bow consists of rays which have undergone two internal reflections. In each reflection some light is lost, explaining the reason why the secondary bow is fainter than the primary one. A schematic view of the process is reported in Fig. 2.1.

The light rays undergo a process of refraction-reflection-refraction when entering and leaving the water droplet. The dependence of the deflection angle as a function of the impact parameter is clearly seen in the figure, with rays ranging from the head-on one, with a deflection angle of 180°, to the rainbow ray, with a minimal deflection at about 138°. In terms of negative deflection angles Θ, the rainbow angle is the complementary of this value, $\Theta_R \simeq 42°$. The interesting physics effect is the concentration of many light rays near the rainbow angle Θ_R resulting in an enhanced light intensity followed by a shadow region. From a classical point of view [23], the shadow is due to

the maximum of the *deflection function* $\Theta(b)$, since the intensity of the scattered light is proportional to the first derivative of $\Theta(b)$:

$$\frac{d\sigma}{d\Omega} = \sum_b \frac{b}{\sin\Theta(b) \mid d\Theta(b)/db \mid} \tag{2.1}$$

where b is the classical impact parameter. Equation (2.1) has a divergence at Θ_R: this is often referred to as *caustic* in optics and represents the envelope of a system of rays, always associated with an intensity highlight.

Descartes's theory of the rainbow was inadequate in explaining the existence of this divergence. Moreover, it was unable to explain the presence of a series of alternatively bright and dark bands inside the primary bow, called *supernumerary bows*. The presence of these bows is due to the interference of those rays which have an impact parameter slightly different from the one associated with the rainbow angle. Two rays scattered in the same direction by a raindrop are strictly analogous to the light passing through the two pinholes in Young's experiment. At angles very close to Θ_R the two paths through the droplet differ only slightly, and so the two rays interfere constructively. As the angle increases, the two rays follow paths of increasingly different length, until they interfere destructively, when their difference equals half of the wavelength. The result is a periodic variation in the intensity of the scattered light, a series of alternately bright and dark bands, giving rise to the supernumerary bows. The pattern of these supernumerary arcs, in contrast to the rainbow angle, is therefore dependent on the droplet size, because the scattering angles at which the interference is constructive are determined by the difference between two path lengths.

It was the 19th century when George B. Airy provided the first mathematical model of the rainbow based on the light wave diffraction and interference [7]. The starting point of the Airy's model was the Huygens' principle which regards every point of a wave front as being a source of secondary spherical waves, whose envelopment defines a new wave front and hence describes the propagation of the wave. Airy was then able to express the intensity of the scattered light in the rainbow region in terms of a new mathematical function, nowadays known as Airy's function $A_i(x)$, reported in Fig. 2.2.

He demonstrated the self-interference of the wave front as it becomes folded onto itself during the refraction and reflection within the raindrop: as a consequence, the primary rainbow is the first interference maximum, while the second and third maxima

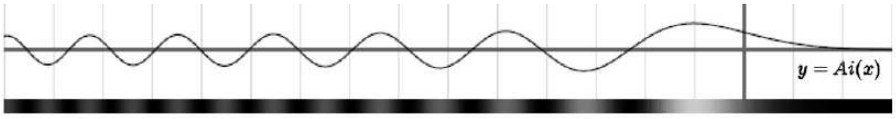

Figure 2.2: The Airy function $A_i(x)$. The argument x is proportional to $\Theta - \Theta_R$. Positive x is on the dark side of the rainbow, located at $x = 0$. Below the intensity of the scattered light, proportional to $A_i(x)^2$. The primary bow, as well as the supernumerary ones, are clearly visible.

correspond to the supernumerary bows. Moreover, Airy's model removed the divergence of the light intensity at the rainbow angle (see Fig. 2.3 for a comparison with other models).

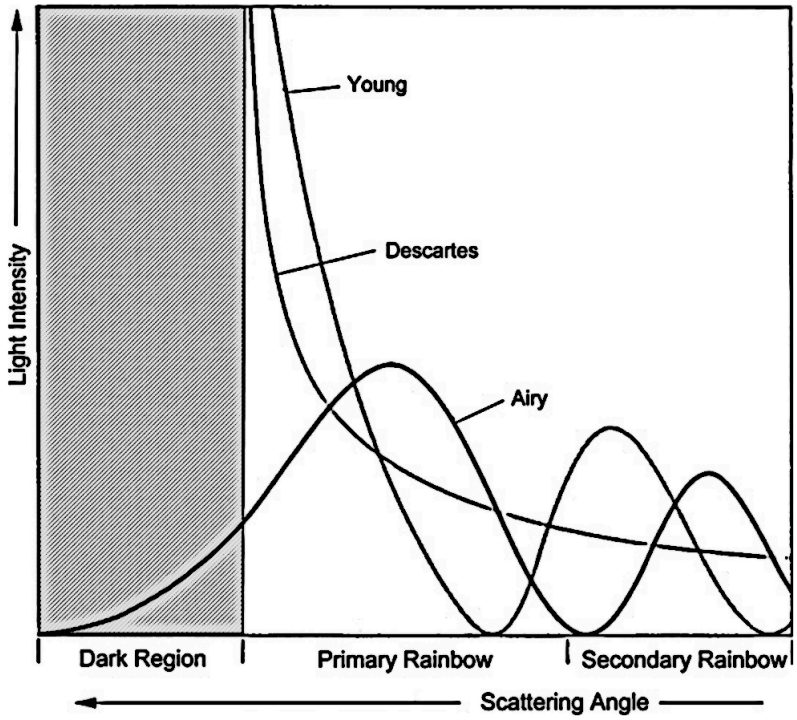

Figure 2.3: Predicted light intensity for the atmospheric rainbow. While the classical solutions by Descartes, Newton and Young give a divergence of the light intensity at the rainbow angle, Airy's model relocates the peaks in the intensity curve providing an explanation for the gradual fading of the rainbow into shadow.

Although more sophisticated models have been developed in the 20^{th} century, Airy's approach remains a very realistic description of the rainbow pattern, widely used to identify the rainbow features in molecular, atomic and nuclear scattering [23, 24].

2.2 Nuclear rainbow

Nuclei are composite objects which can also display wave properties, just like the sun light, therefore they can be refracted, diffracted and be subject of interference. As a consequence, the nucleus-nucleus scattering may also display rainbow features depending on the scattering conditions and binding structure of the partners of the reaction. The atmospheric rainbow is due to processes which do not involve the absorption of light, i.e. reflection and refraction. Following this similarity, the nuclear rainbow is expected to manifest itself mainly in the elastic scattering channel, if a system with small absorption is considered.

The first observation of a rainbow pattern was obtained in the elastic scattering of alpha particles on nuclei at $E_{lab} \approx 140$ MeV by Goldberg *et al* [4, 8, 9], and later on in the elastic scattering of strongly bound nuclei such as ^{12}C + ^{12}C [10–12] and ^{16}O + ^{16}O [1, 13, 14]. For these systems, the absorptive component of the nuclear potential was sufficiently weak for the rainbow effect to appear.

Qualitatively, a nuclear rainbow can be identified by the resemblance of the angular distribution shape to the square of the Airy function followed by an exponential falloff, just as in the case of semiclassical rainbow scattering. An example for the ^{16}O + ^{16}O at 350 MeV is shown in Fig. 2.4.

The most important physics input in the study of the nuclear rainbow scattering is the nucleus-nucleus potential *V(R)*, used in the optical model to describe the scattering process. It is directly connected with the refractive index of nuclear matter, according to:

$$n(R) = \sqrt{1 - V(R)/E} \tag{2.2}$$

Since the potentials are attractive, $(V(R) < 0)$, the refractive index is larger than unity. Due to the dependence of $n(R)$ on the nucleus-nucleus optical potential, the nuclear rainbow pattern is much more difficult to detect and identify with respect to its optic counterpart. Contrary to more common diffraction scattering, which is sensitive only to the nuclear periphery, the dominance of the refraction means that the interaction in the nuclear interior is important: if observed, nuclear rainbows become a unique instrument for studying the nucleus-nucleus interaction at small distances, where the density overlap between the two colliding nuclei can reach values up to twice the nuclear matter saturation value ρ_0.

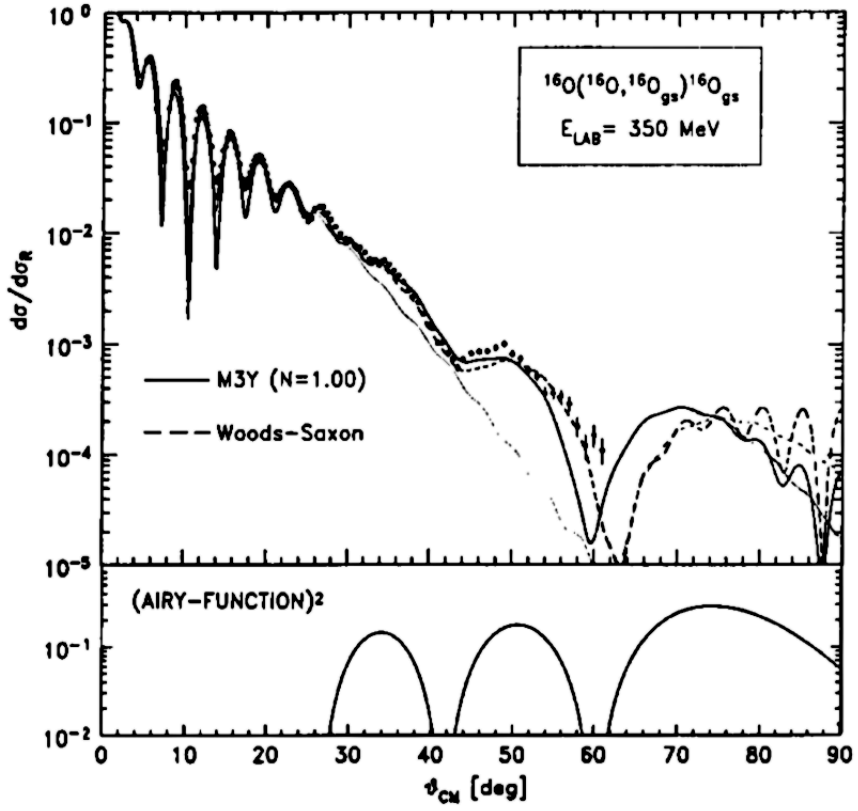

Figure 2.4: Angular distribution of the elastic scattering of ^{16}O + ^{16}O at 350 MeV. The full line and dashed line correspond to optical model calculations with a double folding and a Wood-Saxon potential, respectively. In the lower part of the figure the square of the Airy function $A_i(x)^2$, with $x = 0.0943(\theta - 85°)$ is shown.

2.2.1 Strong vs incomplete absorption

In general, elastic scattering experiments with heavy ions reveal the presence of a strong absorption, i.e. the partial loss of flux from the elastic channel into various non elastic reactions during the collision. In analogy with optics, in which the absorption of light is described through a complex refractive index, the nucleus-nucleus optical potential can be written as the sum of a real part *V(R)*, describing elastic scattering, and an imaginary part *W(R)*, which describes the absorption from the elastic channel:

$$U(R) = V(R) + iW(R) \tag{2.3}$$

This absorption can suppress significantly the refractive structure of the elastic scattering, a situation which is typical for the most heavy ion systems [25], especially those involving medium to heavy nuclei.
The weight of the absorption can be estimated through the elastic *S matrix*. This appears in the quantum mechanical expansion of the elastic nucleus-nucleus scattering amplitude into partial waves series [15]:

$$f(\Theta) = f_C(\Theta) + \frac{i}{2k}\sum_l (2l+1)e^{2i\sigma_l}(1-S_l)P_l(\cos\Theta) \tag{2.4}$$

where $f_C(\Theta)$ is the amplitude of the Coulomb scattering, σ_l is the Coulomb phase shift, k is the wave number and $P_l(\cos\Theta)$ is the Legendre polynomial associated to the angular momentum l. S_l is the scattering matrix element for the lth partial wave, defined as:

$$S_l = \eta_l e^{2i\delta_l} \qquad\qquad 0 \leq \eta_l \leq 1 \tag{2.5}$$

where the reflection coefficient η_l and the nuclear phase shift δ_l are both real. In this contest, $|S_l|$ gives the measure of the absorption strength at a given impact parameter or internuclear distance $R \approx (l+1/2)\hbar/k$. For a strong absorbing system usually is $|S_l| \leq 10^{-4}$ for $l < l_g \approx kR_g$, where R_g is the critical or grazing radius at which the colliding pair begin to experience the strong nuclear interaction that acts between them.
The situation is different when dealing with light heavy ion systems, such as ^{12}C + ^{12}C or ^{16}O + ^{16}O, where the refractive rainbow pattern has been observed. In such cases, the weaker absorption makes possible the observation of elastic scattering events occurring at sub-surface distances, with $l < l_g$. The elastic angular distribution does not show a simple exponential decrease, characteristic of the strong absorptive systems. Conversely, it is larger at large scattering angles, and carries information on the nucleus-nucleus interaction at smaller distances.
In the semiclassical representation, a weak absorption allows to keep the underlying trajectory picture for the scattering system. Some typical trajectories for the elastic wave scattered by an attractive nuclear potential plus a repulsive Coulomb potential are shown in Fig. 2.5.

In the right side of Fig. 2.5 the scattering angle as a function of the impact parameter b or angular momentum $(l+1/2\hbar) = kb$ is the *deflection function* $\Theta(l)$ already

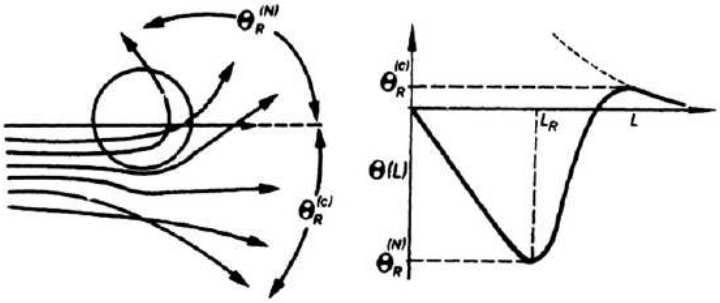

Figure 2.5: Classical picture of the elastic scattering process. Left: trajectories of the nuclear waves elastically scattered by a short-range attractive nuclear potential plus a long-range repulsive Coulomb potential. Right: the corresponding deflection function.

seen in eq. 2.1. Classically, the deflection function is given by [26]:

$$\Theta(b) = \pi - 2\int_{r_{min}}^{\infty} \frac{b/r^2}{\sqrt{1 - b^2/r^2 - V(r)/E_{cm}}} dr \tag{2.6}$$

where *V(r)* and E_{cm} represent the central potential and total energy in the center of mass reference frame, respectively. The r_{min} parameter is the turning point of the trajectory.

In the semiclassical or Wentzel-Kramers-Brillouin (WKB) approximation of quantum scattering, the deflection function is related to the real nuclear phase shifts $\delta(l)$ through:

$$\Theta(l) = 2\frac{d\delta(l)}{dl} \tag{2.7}$$

Looking at the deflection function plot on the right side of Fig. 2.5 and considering again the analogy with optics, the two extrema of $\Theta(l)$ can be identified as the Coulomb ($\Theta_R^{(C)}$) and nuclear ($\Theta_R^{(N)}$) rainbow, respectively. The former is well described in terms of interplay between the Coulomb potential and nuclear potential at the nuclear surface. The nuclear rainbow, on the other hand, is much more difficult to identify and can be properly described only if a realistic choice of the real part of the nucleus-nucleus optical potential is taken also for the internal part.

2.2.2 Nearside-farside decomposition of the scattering amplitude

In the classical picture of Fig. 2.5 more than one trajectory can contribute to the scattering amplitude at a fixed observation angle Θ, as shown in Fig. 2.6.

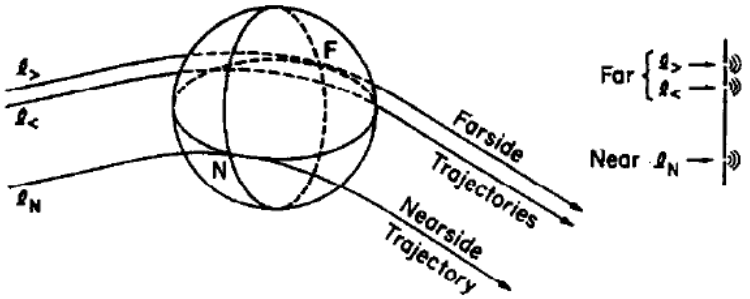

Figure 2.6: Schematic representation of the nearside and farside trajectories, with three semiclassical trajectories that result in the same scattering angle. The right-hand part suggests how the resulting angular distribution is analogous to a three-slit interference pattern.

This figure shows three different trajectories that contribute to the same scattering angle even if deflected from opposite sides of the target nucleus. Those trajectories with positive Θ, which are dominated by the Coulomb repulsion, contribute mainly to the *nearside* scattering while those bent to negative angles, which have undergone the nuclear attraction, contribute to the *farside* scattering. Thus, the more pronounced the nuclear rainbow, the stronger the farside component and the more information on the real part of the nuclear potential can be deduced from the analysis of the elastic scattering process.

It is possible to consider explicitly the contribution of the nearside and farside trajectories to the elastic scattering amplitude using a method developed by Fuller [27]. If the standing wave $P_l(\cos\Theta)$ is decomposed into waves travelling in Θ running in opposite ways around the scattering center, the total scattering amplitude can be written:

$$f(\Theta) = f_{Coul}(\Theta) + f_{nucl}(\Theta) = f_N(\Theta) + f_F(\Theta) \tag{2.8}$$

$$f_N(\Theta) = f_{CN}(\Theta) - \frac{i}{2k}\sum_l (2l+1)e^{2i\sigma_l}(S_l - 1)\tilde{Q}_l^-(\cos\Theta) \tag{2.9}$$

$$f_F(\Theta) = f_{CF}(\Theta) - \frac{i}{2k}\sum_l (2l+1)e^{2i\sigma_l}(S_l - 1)\tilde{Q}_l^+(\cos\Theta) \tag{2.10}$$

where $f_{CN}(\Theta)$ and $f_{CF}(\Theta)$ are the nearside and farside components of the Coulomb amplitude and

$$\tilde{Q}_l^{(\mp)}(\cos\Theta) = \frac{1}{2}\left[P_l(\cos\Theta) \pm \frac{2i}{\pi}Q_l(\cos\Theta)\right] \tag{2.11}$$

with $Q_l(\cos\Theta)$ Legendre functions of the second kind.
An example of the nearside/farside decomposition using the Fuller's method is shown in Fig. 2.7 for the ^{16}O + ^{16}O elastic scattering at 350 MeV [2].

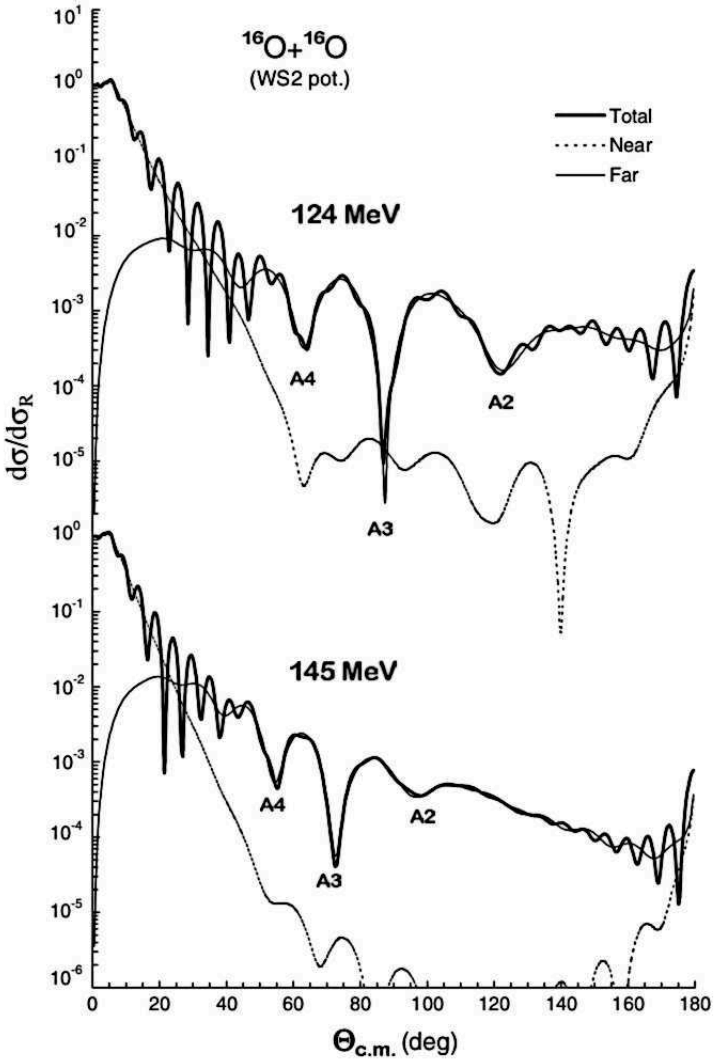

Figure 2.7: Example of the nearside/farside decomposition method. The unsymmetrized ^{16}O + ^{16}O elastic scattering cross section is decomposed in the nearside (dotted lines) and farside (solid lines) components using the Fuller's method for two different incident energies. A(k) indicates the k-th order of the Airy minimum. WS2 is the Woods-Saxon squared potential used to fit the data.

The angular distribution in Fig 2.7 can be fully understood in terms of near-side/farside components of the elastic cross section. The well known Fraunhofer os-

cillation pattern observed at small angles is due to the interference of the nearside and farside amplitude in forward direction. On the other hand, the behaviour of the distribution at large angles is dominated by the farside amplitude, with a well pronounced series of Airy minima both at 124 MeV and at 145 MeV. These minima are due to the interference between the $l_<$ and $l_>$ components of the farside amplitude (see Fig. 2.6), which correspond to trajectories scattered at the same angle Θ with angular momenta $l < l_R$ and $l > l_R$, where l_R is the angular momentum associated with the rainbow angle Θ_R. The $l_<$ component corresponds to small impact parameters (from the relation $(l + 1/2\hbar = kR)$ smaller than the one related to the rainbow angle. As a consequence, the $l_<$ amplitude is more efficiently absorbed than the $l_>$ one. Thus, in a strong absorptive system, the $l_<$ contributions are deeply suppressed and the angular distributions do not show any interference pattern at large angles, just decreasing with an exponential shape. In terms of the complex nucleus-nucleus optical potential *U(R)* (6.2), it is possible to observe a nuclear rainbow pattern in the angular distribution only if the absorptive imaginary part *W(R)* is weak enough for the $l_<$ component to survive in the scattering process, being, at the same time, the real part *V(R)* strong enough to deflect the trajectories to large negative angles Θ, giving rise to the Airy interference between $l_<$ and $l_>$ components.

The nuclear rainbow pattern is therefore produced by the farside trajectories which are governed by the attractive part of the nuclus-nucleus potential. This is the reason why this phenomenon is absent in any scattering process that does not involve a strong nuclear interaction, like the scattering of electrons by atoms.

In the quantal approach, the nearside/farside decomposition can be done exactly using the Fuller's method. However, the oscillating interference pattern at small angles can also be treated in a semiclassical way, using a method based on the strong absorption model [15, 28]. In this model, the nearside and farside components of the scattering amplitude are given by:

$$\sqrt{2\pi \sin\Theta} f_N(\Theta) \sim e^{-i\lambda_g \Theta} e^{(-\gamma_N(\Theta - \Theta_g)} \tag{2.12}$$

$$\sqrt{2\pi \sin\Theta} f_F(\Theta) \sim e^{i\lambda_g \Theta} e^{(-\gamma_F(\Theta + \Theta_g)} \tag{2.13}$$

where Θ_g is the grazing angle associated with the grazing angular momentum $\hbar\lambda_g = \hbar(l_g + 1/2)$. As already said, the oscillating pattern observed at small angles is due to

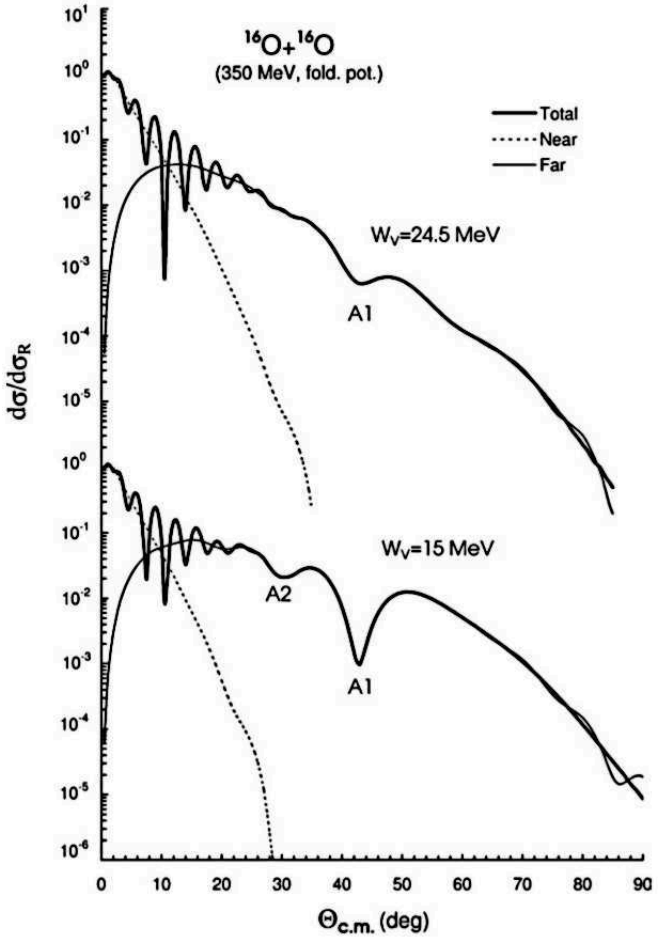

Figure 2.8: The unsymmetrized $^{16}O + ^{16}O$ elastic scattering cross section decomposed in the nearside (dotted lines) and farside (solid lines) components using the Fuller's method with two different depths of the absorptive imaginary part of the folded potential. The Fraunhofer crossover is associated with the deep minimum at $\Theta \approx 10°$.

the interference between $f_N(\Theta)$ and $f_F(\Theta)$, which is governed by the slope parameters γ_N and γ_F and has a typical spacing of $\Delta\Theta \simeq \pi/\lambda_g$. The effect of a real *attractive* nuclear potential is to enhance $f_F(\Theta)$ over $f_N(\Theta)$ giving rise to the so called *Fraunhofer crossover* obtained for an angle

$$\bar{\Theta} = \Theta_g(\gamma_N + \gamma_F)/(\gamma_N - \gamma_F) \tag{2.14}$$

at which $|f_N(\bar{\Theta})| = |f_F(\bar{\Theta})|$, maximizing the amplitude of the oscillations. For peripheral impact parameters, for which $\Theta < \bar{\Theta}$, the nearside component is dominant, with

positive-angle scattering due to the repulsion from the scattering centre. Conversely, for small impact parameters ($\Theta > \bar{\Theta}$), the farside amplitude becomes dominant, with negative-angle scattering caused by the attraction towards the scattering centre. From an experimental point of view, the Fraunhofer crossover manifests itself in the elastic angular distribution as a deep interference minimum (see Fig. 2.8 at small angles). Thus, an accurate experimental measurement of the Fraunhofer crossover can provide an estimation of the refractive and attractive strength of the real optical potential causing it.

2.3 The optical potential

2.3.1 General features

In the previous paragraphs the optical nucleus-nucleus potential has been shown to be the key quantity to be investigated for a deep comprehension of the nuclear rainbow phenomenon. Thus, it is necessary to give a more detailed description of the main approaches used in the treatment of the realistic heavy-ion nuclear interaction.
From a theoretical point of view, the treatment of the elastic scattering reduces to the resolution of the Schrödinger equation:

$$\left[-\frac{\hbar^2}{2\mu}\nabla^2 + U(R) + V_C(R) - E\right]\chi(\mathbf{R}) = 0 \tag{2.15}$$

where μ is the reduced mass of the colliding nuclei, E is the energy of the relative motion in the center of mass system and $V_C(R)$ is the Coulomb potential. $U(R)$ is the complex nucleus-nucleus optical potential, whose imaginary part takes into account the absorption due to all the open inelastic channels during the collision. Using the solution $\chi(\mathbf{R})$ of equation 2.15 and imposing the appropriate boundary conditions, it is possible to obtain the cross section for the elastic scattering process investigated [15]. The choice of the effective nuclear interaction $U(R)$ is the crucial problem to deal with. The simplest way is to adopt a phenomenological potential, in which some parameters can be adjusted in order to obtain the best fit with the experimental cross sections. Among the potentials, the Woods-Saxon shape has been the most widely used in the past, nowadays replaced by its squared version (WS2), which is more physical and closer to the shape of the microscopic approach for the real nuclear optical potential.

A microscopic description of the nucleus-nucleus interaction requires two fundamental ingredients: i) a realistic choice of the nucleon-nucleon interaction for the colliding system and ii) realistic wave functions for the projectile and the target. Even if the two conditions are satisfied, there still remain the inconvenient that the interaction between two composite nuclei is a complicated many-body problem and, therefore, it is not possible to perform a truly microscopic theory like in the nucleon-nucleon case. Only an approximated approach is possible within the framework of the Feshbach reaction theory [29].

In the scattering process between the projectile nucleus a on a target nucleus A the total wave function of the system can be written as:

$$\Psi = \sum_{mn} \chi_{mn}(\mathbf{R}) \psi_m^{(a)}(\xi_a) \psi_n^{(A)}(\xi_A) \tag{2.16}$$

where $\chi_{mn}(\mathbf{R})$ describes the relative motion of the colliding system when projectile and target are in states labelled by m and n, respectively. With this notation, the elastic scattering is described by $\chi_{00}(\mathbf{R})$, since $m = 0$ and $n = 0$ are the labels for the ground states of both the projectile and the target. Inserting this expansion in equation (2.15) and integrating over the internal coordinates ξ_a and ξ_A, an infinite set of coupled equations for $\chi_{mn}(\mathbf{R})$ is obtained. The solution $\chi_{00}(\mathbf{R})$ for the elastic scattering process can be obtained using the Feschbach projection operators [15, 29]. The final result is an expression for the effective interaction between the colliding nuclei in the *elastic channel only*:

$$U = V_{00} + \lim_{\epsilon \to 0} {\sum_{\alpha\alpha'}}' V_{0\alpha} \left(\frac{1}{E - H + i\epsilon} \right)_{\alpha\alpha'} V_{\alpha' 0} \tag{2.17}$$

where $V_{\alpha\alpha'}$ is the first order interaction between the two nuclei, with the label α indicating a pair of internal nuclear states mn. The primed sum runs over all the pair states with the exclusion of the ground state $\alpha = 00$. The first term of equation (2.17) is real and can be evaluated using a double-folding approach [2, 25, 30]:

$$V_{00} = V_F = \left(\psi_0^{(a)} \psi_0^{(A)} | V | \psi_0^{(a)} \psi_0^{(A)} \right) \tag{2.18}$$

where $\psi_0^{(a)}$ and $\psi_0^{(A)}$ are the ground state wave functions of the projectile and the target, respectively, and the round brackets denote integration over all their internal

coordinates ξ_a and ξ_A. Equation (2.17) can be written as:

$$U = V_F + \Delta U \tag{2.19}$$

In this equation, ΔU represents the *dynamic polarization potential* (DPP), which takes into account all the contributions due to the couplings to the non-elastic channels. The imaginary part ImΔU is the main source of absorption, since it describes transitions to the open non-elastic channels, while its real part, ReΔU, also contributes to the total optical potential, even if it is much smaller than V_F [23, 31]. Moreover, ΔU is non local, i. e. $\Delta U = \Delta U(\mathbf{R}, \mathbf{R'})$, because the system that is excited into a non-elastic channel at the position $\mathbf{R}$ returns in general to the elastic channel at another position $\mathbf{R'} \neq \mathbf{R}$.

The first term V_{00} in equation (2.17) is the key quantity for the description of the nuclear interaction when the elastic scattering process is treated. V_{00} can be evaluated within the double folding approach [15, 30, 32]. Indeed, in this model the real part of the nucleus-nucleus optical potential is given by:

$$V_F(R) = \int \rho_1(r_1)\rho_2(r_2)v_{NN}(\mathbf{R} - \mathbf{r}_1 + \mathbf{r}_2)\, d\mathbf{r}_1\, d\mathbf{r}_2 \tag{2.20}$$

where R is the distance between the center of the interacting nuclei, ρ_i are the respective nucleon density distributions and $v_{NN}(\mathbf{r})$ is the effective nucleon-nucleon interaction.

It is clear that the success of the folding model can only be judged meaningfully if i) the effective nucleon-nucleon interaction employed is truly realistic and ii) the nuclear density distributions for the projectile and the target are properly chosen, either directly from electron-nucleus scattering data or from nuclear structure models. A more detailed description of the double folding approach will be given in next chapters, since this method has been adopted in the analysis of the experimental data presented in this work.

2.3.2 The choice of a deep real optical potential

As discussed above, a strong absorption due to the imaginary part of the nucleus-nucleus interaction is usually present when dealing with heavy-ion scattering processes. This is the main reason why the depth of the optical potential has been uncertain for decades. However, careful studies about the rainbow mechanism in α-nucleus [3, 4, 8]

and light heavy-ion [23, 33] scattering seem to support the choice of a *deep* real part of the optical potential.

The optical model analysis of the elastic α-nucleus scattering data has been performed using different shapes of the potential, ranging from the standard Woods-Saxon [4, 9] to those deduced from a model-independent analysis (MIA). Irrespective of the used approach, the result is always a weakly absorbing imaginary potential plus a deep real potential which is close to that predicted by the folding model. The real part of the optical potential for α+^{40}Ca system at 104 MeV using the MIA approach and the double folding one is shown in Fig. 2.9.

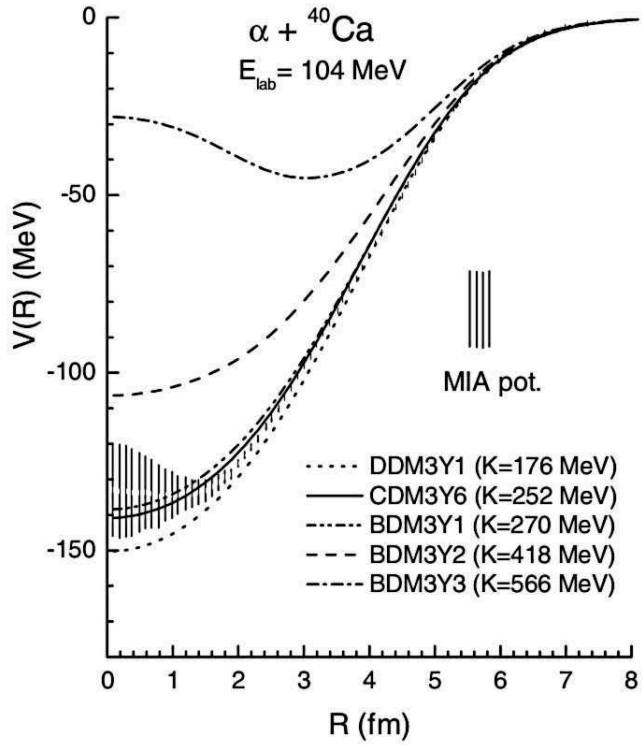

Figure 2.9: Radial shape of the real optical potential for the α+^{40}Ca system at 104 MeV. Model-independent analysis (hatched area) and double folding approach (lines) obtained with different density-dependent nucleon-nucleon interactions. The K values are the nuclear incompressibilities in the Hartree-Fock calculation of nuclear matter.

The comparison between the two approaches shows that the MIA potential agrees best with the double folding potential when most realistic density-dependent nucleon-nucleon interactions are chosen (CDM3Y6 and BDM3Y1, corresponding to realistic

values of the incompressibility K of nuclear matter). Such a comparison is very helpful in justifying the validity of the double-folding approach as a reliable tool to predict the real nucleus-nucleus optical potential.

Even if the strong absorption starts to play a role when increasing the mass numbers of the colliding partners, a rather unique systematization of the optical potential is possible for light heavy-ion systems, like ^{12}C + ^{12}C or ^{16}O + ^{16}O [24, 33]. In ref. [33] it is shown that, in the energy range of 6-100 AMeV, the central depth of the real optical potential is $V(R) \approx 100 - 300$ MeV and the ratio of the real to the imaginary part is $V(R)/W(R) \approx 1$ in the surface region, being $V(R)/W(R) \gg 1$ for both small and large distances R. Actually, such a deep real potential is in agreement with the results obtained with a double folding approach [30, 34, 35], at least when standard values ($200\,\mathrm{MeV} \leq K \leq 300\,\mathrm{MeV}$) of the nuclear incompressibility are used.

The choice of a deep real optical potential is also needed to correctly describe the shape of the low-energy resonances as well as the bound ^{12}C + ^{12}C cluster states in ^{24}Mg [36] and the ^{16}O + ^{16}O cluster states in ^{32}S [37]. In these systems, only a deep real potential can generate the correct number of nodes for the total not Pauli-forbidden cluster state wave function. Therefore, a consistent description of the low-energy resonances as well as the bound cluster states has been achieved only with a deep real optical potential which is a continuation of the deep real potential necessary to explain the nuclear rainbow scattering at higher energies.

2.4 Nuclear rainbow and the connection with EOS

In the refractive elastic scattering process, two nuclei are brought into strong overlap in their ground states during the collision. For elastic scattering at intermediate energy it can be assumed that the densities overlap without disturbance, obtaining a density profile for small internuclear distances which reaches twice the saturation density ρ_0 of nuclear matter. This feature is unique for a quantal system and is not related to compression, which would simultaneously heat up the system. At these small distances, where large density overlaps of the scattered nuclei occur, the folding potential (2.20) is very sensitive to the details of the effective nucleon-nucleon interaction. Moreover, it has been shown [30, 34, 35, 38] that a consistent description of the data can only be obtained with a distinct but rather weak dependence of the nucleon-nucleon interaction on the

density of the nuclear medium. Thus, it can be argued that the density dependence of the nucleon interaction can be probed via the nucleus-nucleus potential, described by (2.20), if the nuclear rainbow is observed, because it scans the nucleus-nucleus interaction at small distances. Moreover, the density dependence of $v_{NN}(\mathbf{r}, \rho)$ enters in the determination of the saturation properties of nuclear matter in Hartree-Fock calculations. As a consequence, the study of refractive nucleus-nucleus scattering gives a unique access to the study of the Equation Of State (EOS) of cold nuclear matter. In Fig. 2.10 a schematic view of this link is sketched.

The EOS describes the variation of the total energy as a function of the nuclear matter density ρ or, more specifically for a finite system, the binding energy per nucleon E/A as a function of density (and temperature). The variation of E/A over a region of densities $\rho/\rho_0 = 0.0$ to 4.0 relative to the saturation value ρ_0 is shown in Fig. 2.11.

The saturation point of nuclear matter is given by $E/A = 17.2$ MeV at $\rho_0 = 0.17\, fm^{-3}$. The variation of $E/A(\rho)$ close to ρ_0 can be well described by a quadratic function. The examples shown in Fig. 2.11 have been calculated with an effective nucleon-nucleon interaction which is density dependent. This allows to reproduce the correct saturation value at ρ_0 and gives various curvatures around this point, the second derivative defining the incompressibility parameter K through the relation:

$$K = 9\rho^2 \frac{d^2\,[E/A]}{d\rho^2}\bigg|_{\rho=\rho_0} \tag{2.21}$$

Different types of the EOS are usually distinguished by different values of the nuclear incompressibility K. Some information on reliable K values are obtained from the analysis of transverse flows and fragments spectra in high energy central heavy ion collisions [39]. However, it turned out that the folding model analysis of high-precision nuclear rainbow scattering data can be used as an independent method to determine the nuclear incompressibility K [35].

A constraint on the K value comes from the observed neutron star masses [40, 41], as shown in Fig. 2.12. The plot in the figure shows the correlation between the radius and the mass of a neutron star given by three model calculations which differ from each other through the nuclear incompressibility K value [41]. Since it is known, from the observed radio pulsar masses, that the mass of a neutron star is about 1.5 solar masses, a realistic K value should lie in the range $210 - 300$ MeV, as shown in Fig. 2.12. The K

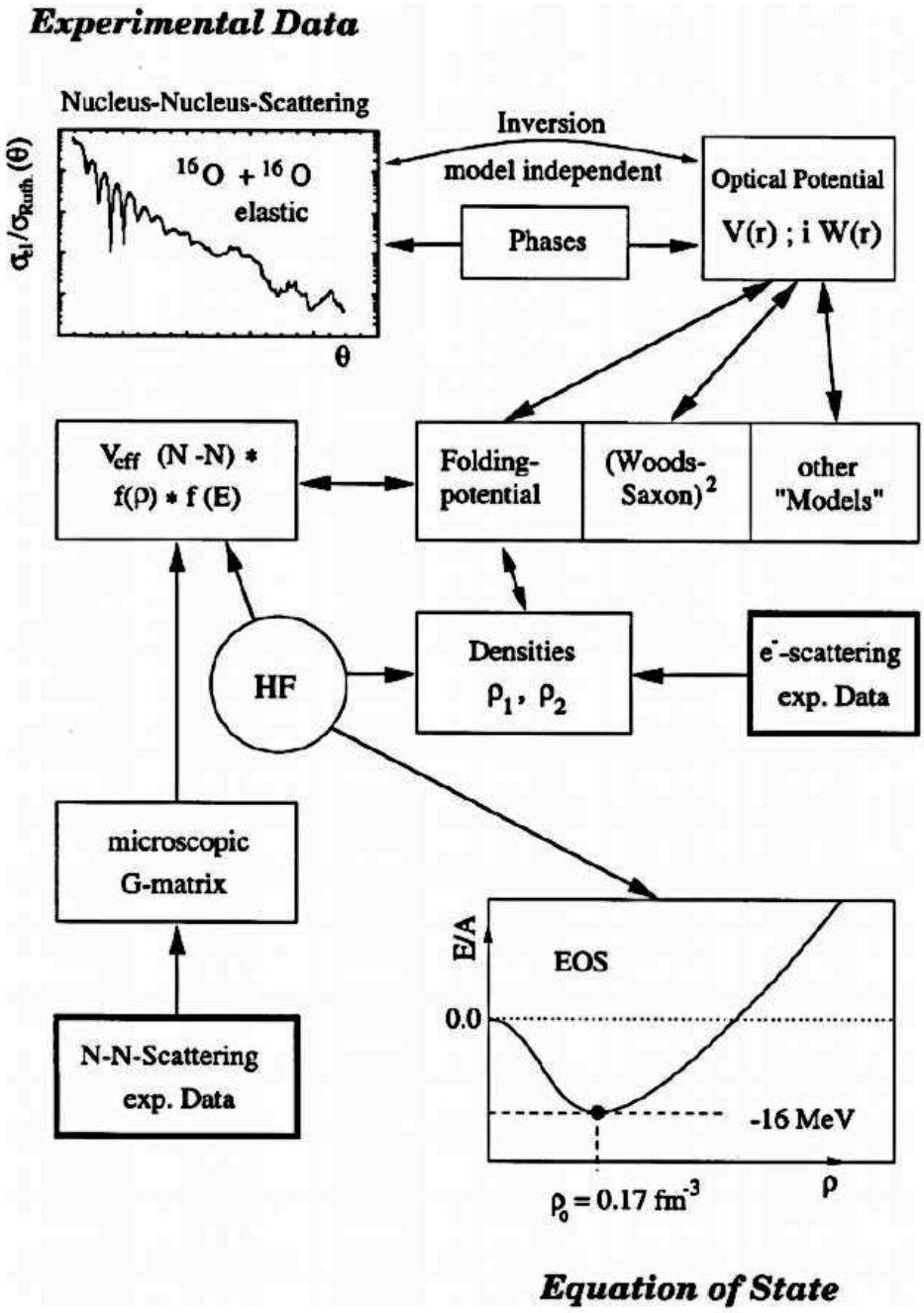

Figure 2.10: The link between the experimental data on elastic scattering, nucleus-nucleus optical potentials, nuclear densities and effective nucleon-nucleon interaction constructed by different theoretical models.

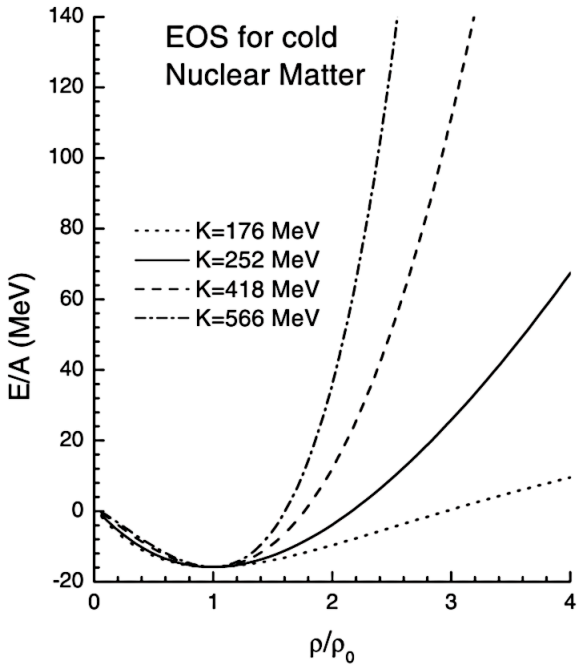

Figure 2.11: Binding energy per nucleon, $E/A(\rho)$, as a function of the density ρ for nuclear matter, obtained by Hartree-Fock calculations. Different density dependent effective nucleon-nucleon interactions, corresponding to different K values, are chosen in order to reproduce the correct saturation energy of nuclear matter.

values extracted from high-energy central heavy ion collisions are, on the other hand, higher, with a typical value of K $\approx 290 \pm 50$ MeV [39].

As discussed above, the nuclear rainbow is linked to the equation of state of cold nuclear matter through the double folding procedure adopted to describe the real part of the optical nucleus-nucleus potential. It is at this stage that the effective nucleon-nucleon interaction comes into play, and different K values are associated with different parametrizations of the in-medium nucleon-nucleon interaction. As an example of this connection, the ^{16}O + ^{16}O system at 350 MeV, which shows one of the clearest nuclear rainbow in the elastic angular distribution (see Fig. 2.14), is reported in Fig. 2.13.

The figure shows how different parametrizations of the effective nucleon-nucleon interaction generate double folded real optical potential which differ mainly at smallest distances, where the density overlap of the colliding partners is larger. The corresponding elastic angular distribution, Fig. 2.14, shows how the CDM3Y6 interaction [35] gives the best fit to the experimental data.

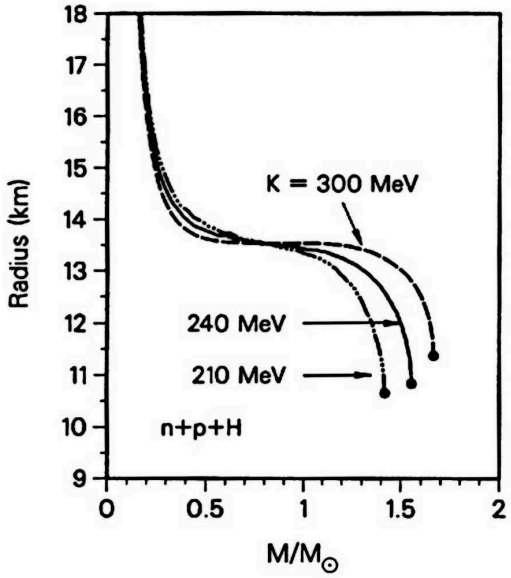

Figure 2.12: Neutron star radius-mass relation given by different EOS's corresponding to different nuclear incompressibilities K. The end point of each curve marks the final value for the neutron star radius.

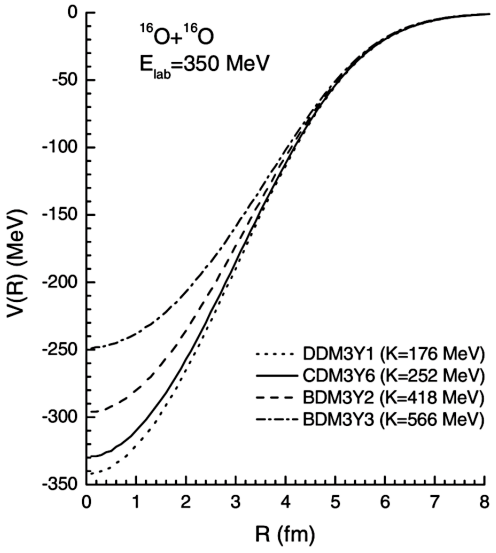

Figure 2.13: The real part of the optical potential for the ^{16}O + ^{16}O system at 350 MeV [1] predicted by the double folding model using four different parametrizations (the same used in Fig. 2.11) for the effective nucleon-nucleon interaction. The corresponding K values are reported in parentheses.

When this best fit version of the density dependent M3Y-Paris interaction is used in

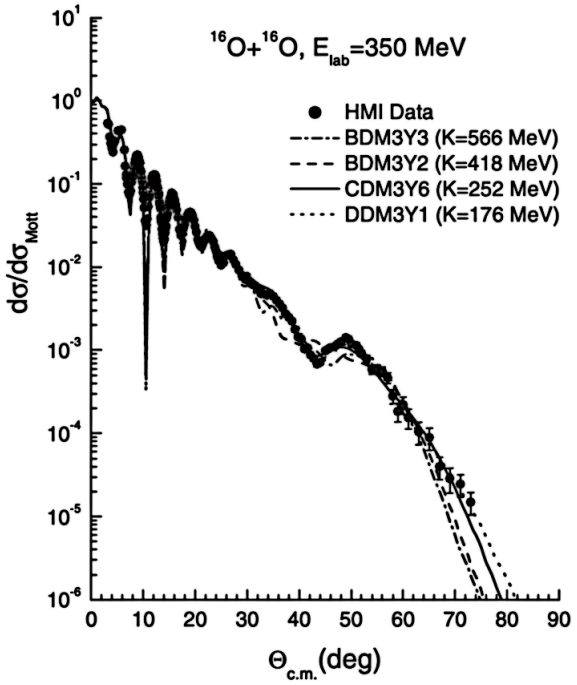

Figure 2.14: Elastic angular distribution for the ^{16}O + ^{16}O system at 350 MeV [1]. The optical potential is composed by a real part given by the double folded potential with the density dependent nucleon-nucleon interactions indicated in the picture. The absorptive imaginary part is taken from [2]. The best fit to the data is obtained with the CDM3Y6 interaction which gives K $\approx$ 252 MeV.

the Hartree-Fock calculation of symmetric nuclear matter, a nuclear incompressibility K $\approx$ 252 MeV is obtained [35]. This value lies in the realistic range $210 - 300$ MeV found from the neutron star mass constraint and therefore returns a "soft" equation of state for cold nuclear matter. A similar result is also obtained in the folding analysis of the refractive elastic α-nucleus scattering data [35, 42].
Thus, it becomes evident how the observation of a nuclear rainbow pattern when dealing with an elastic scattering process can provide very useful, precise and, to some extent, unexpected information about the nuclear structure.

2.5 Brief systematics on nuclear rainbow systems

The final section of this chapter is devoted to a brief review of the main systems in which the nuclear rainbow features were recognized. As already discussed, the pioneering experiment that led to the first observation of the nuclear rainbow was the study

of the $\alpha -$ nucleus elastic scattering at $E_{lab} \approx 140$ MeV by Goldberg *et al.* [4, 9]. Several years later, Put and Paans [3] performed an high-precision $\alpha +^{90}$ Zr experiment, which showed the evolution of the rainbow structure with the incident beam energy (see Fig. 2.15). In the angular distributions shown in figure 2.15 the far-side compo-

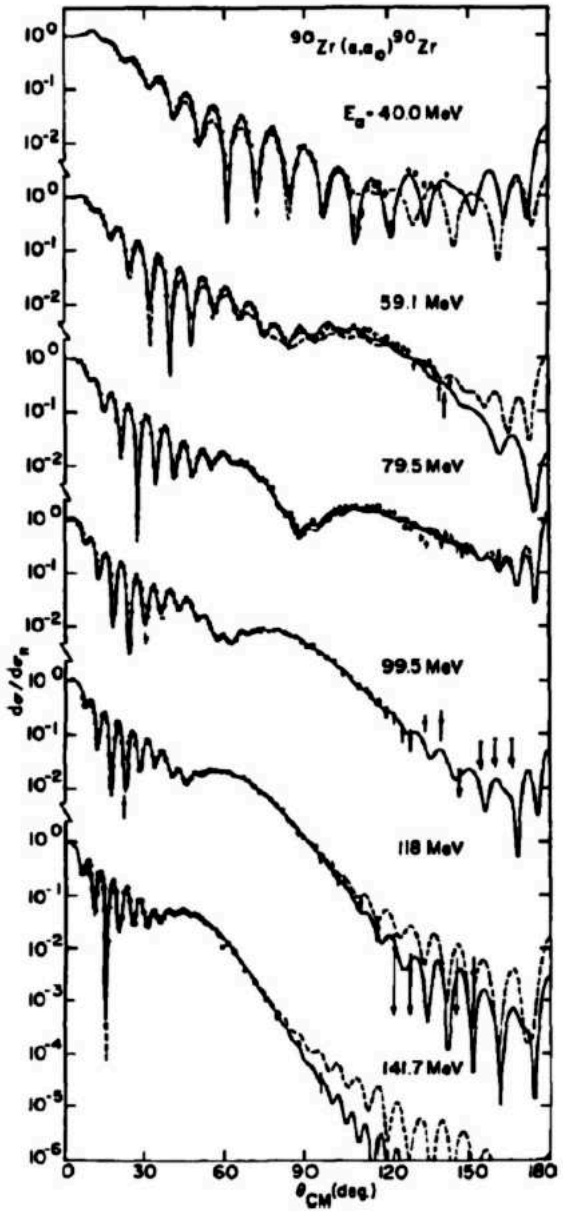

Figure 2.15: Elastic $\alpha +^{90}$ Zr scattering data [3] at several incident energies (the last setting at 141.7 MeV is extracted from [4]). The data are compared with optical model calculations using different parametrizations (solid and dashed lines, respectively).

nent of the scattering amplitude dominates the large angle scattering region already at 59.1 MeV, determining a very pronounced rainbow shoulder at 79.5 MeV. Moreover, a rainbow shift toward smaller scattering angles with increasing beam energy is clearly seen. These data, together with those measured at 141.7 MeV [4], give a very accurate test ground for theoretical models of the $\alpha -$ nucleus optical potential.

A well developed rainbow structure was also observed in the $^{12}C+^{12}C$ elastic scattering in a wide energy range, from about 6 MeV/u up to 200 MeV/u [23]. The main problem when dealing with systems like this is the Mott interference caused by the boson symmetry between two identical nuclei, which results in rapidly oscillating elastic cross sections at angles around $\Theta_{cm} = 90°$, distorting the original Airy structure.

The Mott interference does not affect the elastic scattering of ^{16}O on ^{12}C, and very precise cross section angular distributions for this system were measured by Oglobin *et al.* [5, 43] at several bombarding energies. Their results are presented in Fig. 2.16. These data indicate clearly the diffractive an refractive structure of the angular distributions at small and large scattering angles, respectively. The distributions at $E_{lab} = 132$ and 170 MeV show an enhancement of the cross sections at the largest angles (see Fig. 2.16). This behaviour was explained [44] in terms of $\alpha -$ transfer between the colliding nuclei, which results in additional interference structures at the largest angles. Due to the rather weak absorption, this system was consistently described by the energy-dependent real optical potential given by the folding model.

Finally, evidences of rainbow-like structures were also observed in the elastic scattering of $^{6,7}Li$ at energies up to about 50 MeV/u [45–47] and ^{9}Be at 18 MeV/u [48]. In the latter, the optical model analysis of the elastic angular distributions [48] have identified a strongly damped Airy structure at large angles, which was referred to as the "rainbow ghost". For these light systems the reduced strength of the rainbow pattern, when compared to the $\alpha -$ nucleus case, is mainly due to a stronger absorption associated with the break-up of these α-clustered projectiles [49].

The role of the strong absorption is expected to be more and more important when increasing the masses of the colliding nuclei. Its action naturally tends to hide the rainbow structure in the angular distributions due to the removal of flux from the elastic channel. As a consequence, the rainbow mechanism was thought to be very unlikely for the elastic scattering of systems heavier than $^{16}O + ^{16}O$.

In this work, it will be shown how this is not always true, since a nuclear rainbow

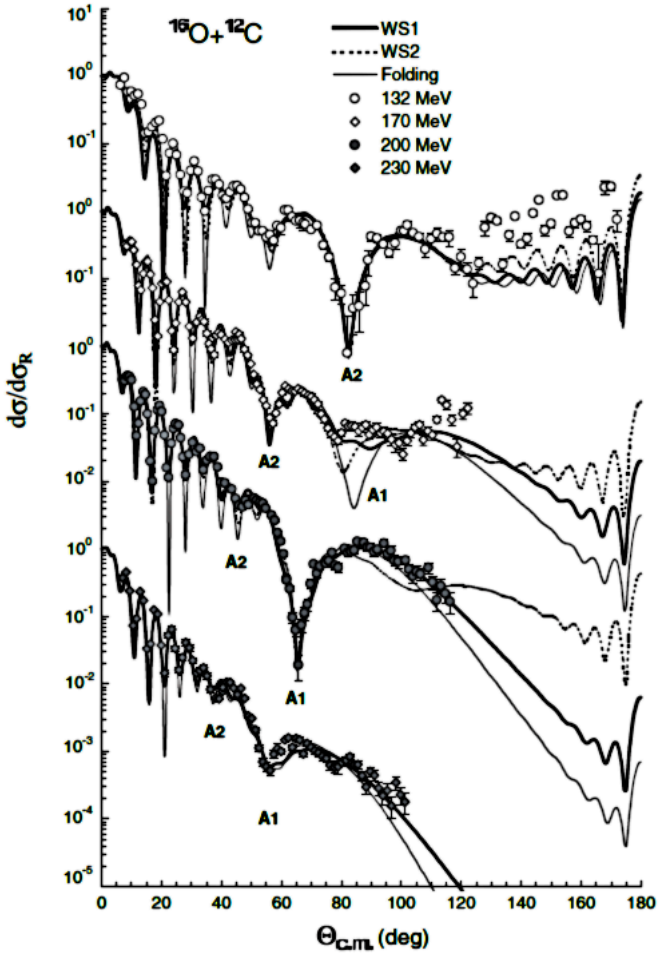

Figure 2.16: ^{16}O +^{12} C elastic angular distributions at E_{lab} = 132, 170, 200 and 230 MeV. The data are compared with two optical model calculations based on two different families of Wood-Saxon potential [5].

structure is identified for the ^{16}O + ^{27}Al elastic scattering at 100 and 280 MeV, as it will be discussed in next chapters.

Chapter 3

Motivation of the experiment

As discussed in the previous Chapter, nuclear rainbow is a very peculiar phenomenon which reveals the nuclear interaction at small distances, where the projectile and target density overlaps can reach values up to twice the nuclear matter saturation value ρ_0. Moreover, it was emphasized how the strong absorption, always present in heavy-ion collisions, tends to hide the refractive component of the scattering process. This represents the main reason why the rainbow features were thought to be very unlikely for systems heavier than ^{16}O + ^{16}O.

Recently, a new generation of parameter-free calculations, using the São Paulo Potential (SPP) [16] combined with Coupled Channels (CC) formalism, has been developed. These calculations take into account dissipative and surface processes in the continuum, like deep-inelastic or break-up reactions, by the introduction of a parameter-free imaginary potential, which is based on the Glauber model. Different systems (^{16}O + ^{27}Al, ^{58}Ni, ^{60}Ni, ^{58}Ni + ^{124}Sn, ^{6,7}Li + ^{120}Sn) were used to test the model in a wide energy range. In particular, for the ^{16}O + ^{27}Al system, the experimental fusion, deep-inelastic and quasi-elastic cross sections are in agreement with the theoretical calculations for $E_{lab}(^{16}\mathrm{O}) < 90$ MeV. Moreover, the SPP/CC calculations predict [17] a nuclear rainbow pattern in the angular distribution for the elastic scattering of ^{16}O on ^{27}Al at 100 MeV (or higher) incident energy, which is strongly connected to the coupling with low-lying target excitations.

In order to verify these predictions, a ^{16}O + ^{27}Al elastic scattering experiment was recently performed at the INFN-LNS in Catania, using a ^{16}O beam delivered by the TANDEM accelerator at 100 MeV incident energy. First evidences of nuclear rainbow

formation were recognized in the experimental elastic angular distribution of the investigated system.
In this Chapter, the experimental results obtained at 100 MeV incident energy will be shown. This experiment, in fact, is the guideline for the further investigation of the ^{16}O + ^{27}Al reaction at the energy of 280 MeV discussed in this work. Before showing the experimental results at 100 MeV, a short description of the theoretical framework used for the comparison with the data, i.e. the São Paulo Potential and the Coupled Channel formalism, will be given for a better comprehension of the results.

3.1 The São Paulo parameter-free double folding potential

In a general treatment, the complex and energy dependent nucleus-nucleus potential can be described as the sum of the real bare (or nuclear) and polarization potentials, the latter containing the contribution arising from non-elastic couplings. In principle, the bare potential between two heavy ions can be associated with the fundamental nucleon-nucleon interaction folded into a product of the nucleon densities of the nuclei [25] (see eq. (2.20)). Both the nuclear and the polarization contributions appear in the integro-differential equation used to describe the motion of the colliding system [16]:

$$-\frac{\hbar^2}{2\mu}\nabla^2\Psi(\mathbf{R})+\left[V_C(R)+V_{pol}(R,E)+i\,W_{pol}(R,E)\right]\Psi(\mathbf{R}) + \int U(\mathbf{R},\mathbf{R}')\Psi(\mathbf{R}')d\mathbf{R}' = E\Psi(\mathbf{R}) \tag{3.1}$$

$\Psi(\mathbf{R})$ is the total wave function of the system and $V_C(R)$ is the Coulomb interaction, assumed to be local. $V_{pol}(R,E)$ and $W_{pol}(R,E)$ are the real and imaginary parts of the polarization potential and, as already stated, contain the contribution arising from non-elastic channel couplings. $U(\mathbf{R},\mathbf{R'})$ is the bare interaction. The dependence on **R** and **R'** means that the interaction is *non-local* and the non locality here is solely due to the Pauli exclusion principle (Pauli non locality) which involves the exchange of identical nucleons between the projectile and the target.
In this context, the São Paulo potential consists in a particular version of the bare nuclear potential. In its standard formulation, the São Paulo parameter-free double

folding potential is expressed in the local equivalent (LE) version [16]:

$$V_{LE}(R,E) = V_F(R)e^{-4\left(\frac{v(R)}{c}\right)^2} \tag{3.2}$$

where $v(R)$ is the local relative velocity between the colliding nuclei, given by:

$$v^2(R) = \frac{2}{\mu}E_k(R) = \frac{2}{\mu}\left[E - V_C(R) - V_{LE}(R,E)\right] \tag{3.3}$$

with μ the reduced mass of the system.

The exponential term in eq. (3.2) is the local velocity dependent correction for Pauli non-locality (PNL), which can also be interpreted as the absolute normalization of the potential [16]. Therefore, in this formulation the effect of the Pauli non locality is equivalent to a velocity-dependent nuclear interaction. $V_F(R)$ is the double folding potential of eq. (2.20), where the heavy-ion nuclear densities are taken from Dirac-Hartree-Bogoliubov (DHB) calculations [50] and from electron scattering experiments [51, 52].

The imaginary part of the potential, which takes into account dissipative processes, is assumed to be simply related to the real one through a proportionality coefficient, independently of the energy and system [17]:

$$W(R,E) = 0.6 \cdot V_{LE}(R,E) \tag{3.4}$$

The reason why it is possible to consider the above proportionality relation can be understood considering a rather physically simple energy window, around $E/A \sim 200$ MeV, where Pauli Blocking (PB) becomes small and PNL is also reduced due to the loss of correlations associated with nucleon exchange between target and projectile for increasing temperature of the composite system. In this energy region [53, 54], the mean free path $\Lambda(R)$ approaches the classical relation:

$$\Lambda(R) = \frac{1}{\sigma_{NN}O(R)} \tag{3.5}$$

where σ_{NN} is the free nucleon-nucleon cross section and the overlap function $O(R)$ is given by:

$$O(R) = \int \rho_1^N(r_1)\rho_2^N(R-r_1)d^3r_1 \tag{3.6}$$

with $\rho_j^N(r_j)$ the ground state nucleon densities and R the distance between the centers of the colliding nuclei.
From the quantum mechanical point of view, the mean free path is related to the imaginary potential $W(R)$ through:

$$\Lambda(R) = \frac{\hbar^2 k}{2\mu W(R)} \tag{3.7}$$

where k is the wave number and μ the reduced mass of the system. Comparing eq. (3.5) with eq. (3.7), the radial dependence of $W(R)$ is the same as that of $O(R)$.
In the zero-range nucleon-nucleon version of the São Paulo potential [16], the overlap density function is related to the double folding potential through:

$$V_F(R) = V_0 O(R) = V_0 \int \rho_1(r_1)\rho_2(R - r_1)d^3r_1 \tag{3.8}$$

where $V_0 = -456$ MeV and $\rho_j(r_j)$ are the nuclear matter densities. Thus, from the above equations, the imaginary part of the nuclear potential is found to be related to the folding potential simply by:

$$W(R) = \eta V_F(R) \tag{3.9}$$

where η has been estimated to be $\eta \approx 0.6$ [17].
The final form of the São Paulo potential, used in the CC calculations, contains also a scaling factor n_r for the real part of the interaction:

$$V_{SPP}(R, E) = V_F(R)e^{-4\left(\frac{v(R)}{c}\right)^2}(n_r + 0.6\,i) = V_{LE}(R, E)(n_r + 0.6\,i) \tag{3.10}$$

where n_r assumes the values of $n_r = 1$ or $n_r = 0.6$ in the case of collisions with tightly-bound or weakly-bound nuclei, respectively.

3.2 The Coupled Channel formalism

In general, the nuclear interaction between a projectile nucleus a and a target nucleus A is fully described by the total wavefunction Ψ, which obeys the complete Schrödinger equation:

$$(E - H)\Psi = 0 \tag{3.11}$$

Starting from the internal states $\psi_a(x_a)$ and $\psi_A(x_A)$ of the projectile and the target, respectively, where the internal variables have been denoted by x, the total wavefunction Ψ can be expanded as:

$$\Psi = \sum_{\alpha} \xi_\alpha(\mathbf{r}_\alpha)\psi_\alpha(x_\alpha) \tag{3.12}$$

where the sum runs over all the internal states of some particular partition $\alpha = a + A$ and the coefficients $\xi_\alpha(\mathbf{r}_\alpha)$ describe the relative motion of the two nuclei a and A when they are in the internal states described by ψ_α.

The sum over α is complete and includes states of a and A in the continuum. Clearly, when dealing with a practical case, it is not possible to take into account the full infinite expansion (3.12). As a consequence, the usual choice is to consider the entrance channel plus a small subset of terms which are supposed to be strongly coupled to it. This means that the total wavefunction Ψ is replaced by a *model* wavefunction Ψ_{model}, defined as:

$$\Psi_{model} = \sum_{\alpha}{}' u_\alpha(\mathbf{r}_\alpha)\psi_\alpha(x_\alpha) \tag{3.13}$$

where the prime index indicates a limited sum. The exact relative motion wavefunctions $\xi_\alpha(\mathbf{r}_\alpha)$ are replaced by the $u_\alpha(\mathbf{r}_\alpha)$ functions: even if they have the same asymptotic behaviour at large $\mathbf{r}_\alpha$, they can differ considerably at short distances.

Since just few terms of the infinite expansion (3.12) are included in (3.13), the model may only represent a small part of the total wavefunction. The coupling between the model part and the rest is represented in an average way by the use of collective interactions, in particular by the use of complex optical potentials.

Starting from this background, the Coupled Channel (CC) method consists in the solution of a relatively small set of coupled equations that results from considering a model wavefunction with a limited number of terms. In the usual scattering situation, some boundary conditions are adopted for the relative motion wavefunctions $\xi_\alpha(\mathbf{r}_\alpha)$. In particular, ξ_α for the entrance channel has the asymptotic form of a plane incident wave plus outgoing spherical waves while all the other $\xi_{\alpha'}$ have outgoing waves only. The total Hamiltonian of the system is expressed as the sum of the internal Hamiltonians for the nuclei a and A, the kinetic energy of their relative motion and their mutual interaction:

$$H = H_\alpha + K_\alpha + V_\alpha \tag{3.14}$$

Multiplying from the left by one of the ψ^*_α, integrating over the internal x_α coordinates and using the orthonormality property of the ψ_α:

$$(\psi_\alpha|\psi_{\alpha'}) = \int \psi^*_\alpha(x_\alpha)\psi_{\alpha'}(x_\alpha)dx_\alpha = \delta_{\alpha\alpha'} \tag{3.15}$$

the infinite set of coupled equations for the channel function $\xi_\alpha(\mathbf{r}_\alpha)$ is obtained, of which a representative one is:

$$[E - \epsilon_\alpha - K_\alpha - (\alpha|V_\alpha|\alpha)]\,\xi_\alpha(\mathbf{r}_\alpha) = \sum_{\alpha\neq\alpha'} \left(\alpha|V_\alpha|\alpha'\right)\xi_{\alpha'}(\mathbf{r}_\alpha) \tag{3.16}$$

The interaction matrix elements, responsible for the excitation from the initial state α to the final state α', are given by:

$$\left(\alpha|V_\alpha|\alpha'\right) \equiv \int \psi^*_\alpha(x_\alpha)V_\alpha(\mathbf{r}_\alpha, x_\alpha)\psi_{\alpha'}(x_\alpha)dx_\alpha = V_{\alpha\alpha'}(\mathbf{r}_\alpha) \tag{3.17}$$

The N-state approximation of the CC method is derived from eq. (3.16) considering a finite number N of equations, chosen depending on the physics of the investigated phenomenon. Of course, this is equivalent to keeping only N terms in the expansion (3.12), i.e. using the model function (3.13). In this case, a finite set of coupled equations is obtained, having the form:

$$[E - \epsilon_\alpha - K_\alpha - (\alpha|V_\alpha|\alpha)]\,u_\alpha(\mathbf{r}_\alpha) = \sum_{\alpha\neq\alpha'} \left(\alpha|V_\alpha|\alpha'\right)u_{\alpha'}(\mathbf{r}_\alpha) \tag{3.18}$$

The interaction matrix elements have the same form as in (3.17), except that V_α is now the model effective interaction in the α channel corresponding to the model function (3.13). In practical CC calculations N is generally small, often $N = 2$: even in this case, the partial wave expansion may result in a very large number of partial-wave coupled equations to be solved.

3.3 The ^{27}Al(^{16}O,^{16}O)^{27}Al reaction at E_{lab} = 100 MeV

As already discussed, CC calculations performed with the São Paulo optical potential predict a nuclear rainbow structure for the ^{16}O +^{27} Al system at 100 MeV. In order to verify the reliability of the theoretical predictions, the ^{16}O +^{27} Al elastic scattering

process was experimentally investigated at the INFN-LNS in Catania. The $^{16}O^{8+}$ primary beam was accelerated at 99.2 MeV incident energy by the Tandem Van de Graaff accelerator and focused on a self-supporting ^{27}Al thin target. The ^{16}O ejectiles were momentum analysed by the MAGNEX magnetic spectrometer [18]. Exploiting its large momentum (20%) and solid angle (50 msr) acceptance, very accurate excitation energy spectra, elastic and inelastic angular distributions were obtained. A complete description of the apparatus and of the adopted data reduction procedure will be given in next Chapters.

The experimental elastic angular distribution for the ^{16}O +^{27} Al system at $E_{lab} = 100$ MeV is shown in Fig. 3.1.

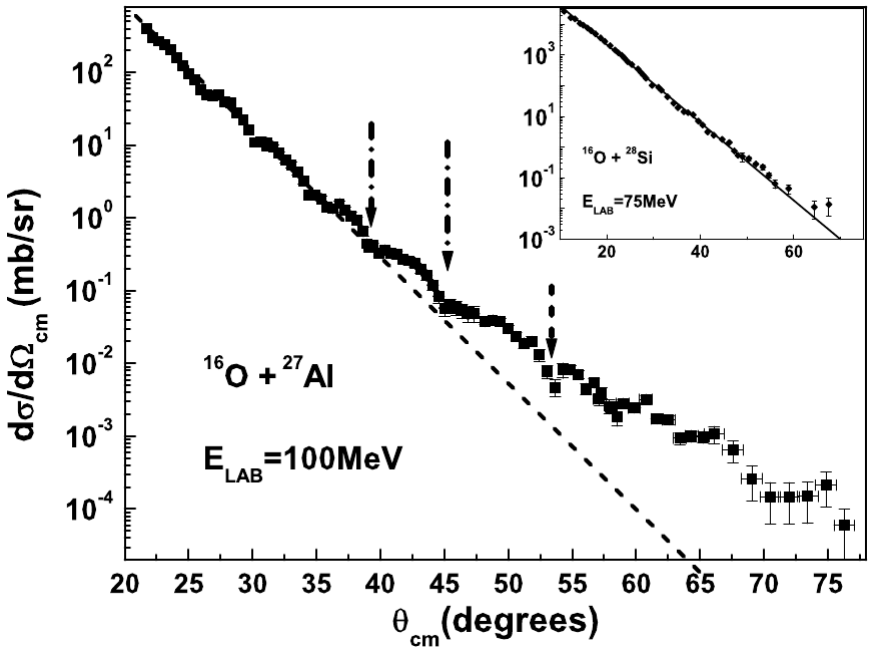

Figure 3.1: Experimental elastic angular distribution for ^{16}O +^{27} Al at 100 MeV. The dashed line is a linear fit in the $22° \leq \theta_{cm} \leq 35°$ angular interval. Airy-like minima are indicated by the arrows. The inset shows elastic angular distribution data for ^{16}O+^{28} Si at 75 MeV , extracted from ref. [6], together with a linear fit in the $10° \leq \theta_{cm} \leq 70°$ angular interval (solid line).

The straight line in the figure corresponds to a linear least squares fit to the elastic cross sections in the $22° \leq \theta_{cm} \leq 35°$ angular range, where the cross section oscillations are connected to the Fraunhofer diffraction pattern. The slope of the angular distribution systematically deviates from the straight line for increasing backward an-

gles, starting from about $\theta_{cm} \sim 40°$. The observed minima, indicated by the arrows, followed by broad structures are consistent with the far-side component of the nuclear rainbow phenomenon. Such behaviour is not present in the ^{28}Si case at $E_{lab} = 75$ MeV (see the inset in Fig. 3.1), the largest energy for which there are experimental data in a sufficiently wide angular range up to now. Anyhow, CC calculations with the São Paulo potential predict, also in this case, the appearance of a rainbow structure at higher energies, at least 6 MeV/u.

The elastic and inelastic angular distributions were compared with the CC/SPP theoretical predictions obtained using the computer code FRESCO [21]. The results are shown in Fig. 3.2. Considering the absence of adjustable parameters, the agreement between the experimental data and the theoretical predictions is good. A slight difference in the phase of the oscillations is observed in both the elastic and inelastic distributions. The coupled channels calculations were performed considering four of the first five low lying collective states of the ^{27}Al target ($1/2^+$, $3/2^+$, $7/2^+$ and $9/2^+$). These states can be described by the weak coupling model [22], considering a $1d_{5/2}$ proton hole coupled with the 2^+ rotational state of the ^{28}Si core. The $5/2^+$ excited state was not included in the calculations, as it was assumed to have a minor role in the coupling scheme due to level repulsion from the ^{27}Al ground state, having same spin and parity.

In the upper panel of Fig. 3.2 the comparison between the CC results (solid line) and the standard OM predictions (dashed line, no couplings) is shown. The comparison shows clearly the crucial role of the inelastic couplings for a better description of the data. In fact, the CC results remain in the same landing $10^{-5} \leq \sigma/\sigma_{Ruth.} \leq 10^{-6}$ over a large angular region, starting from $\theta_{cm} \sim 60°$, while the OM calculations present an exponentially decreasing behaviour. It was then concluded that such a rainbow-like pattern is a consequence of the couplings [55].

Additional calculations including the Pauli Blocking (PB) effect, which reduces the imaginary absorptive potential, were performed and the results are shown in the insets of Fig. 3.2 for the angular range $20° \leq \theta_{cm} \leq 35°$. The introduction of the PB effect improves the agreement with the phase of oscillations at forward angles, but fails at the backward ones, corresponding to smaller impact parameters, where the density overlap between the colliding nuclei is larger.

The calculated S-matrices for the inelastic and elastic scattering as a function of the

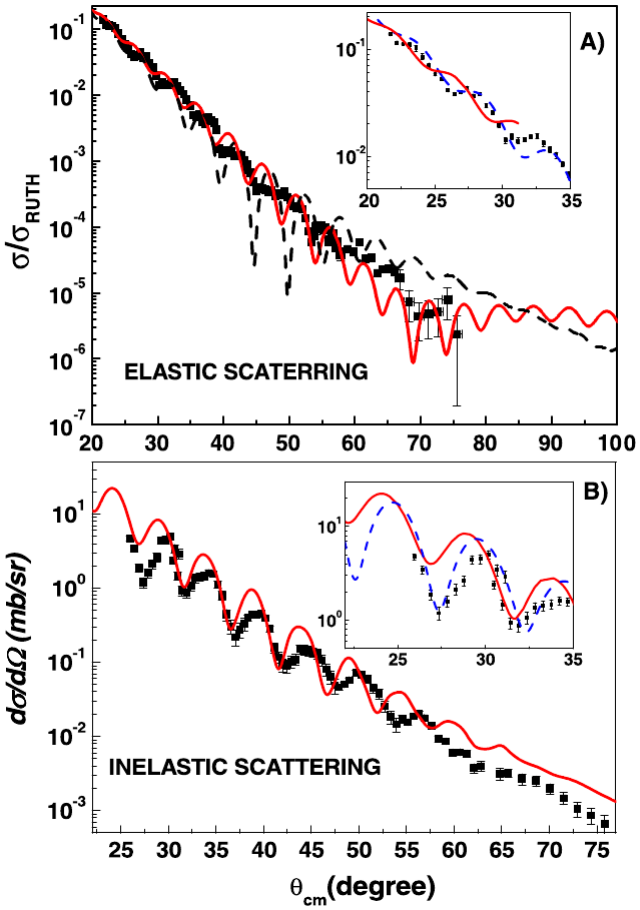

Figure 3.2: Experimental angular distributions for the (A) elastic and (B) inelastic (^{27}Al low-lying states) scattering, as compared with the corresponding theoretical CC predictions (solid lines) and with OM calculations without couplings (dashed line). The insets show expansion regions for which Pauli Blocking (PB) corrected calculations (dashed lines) are also presented (see text).

orbital angular momentum L are shown in Fig. 3.3. The elastic S-matrix was calculated within the CC approach (closed squares) and the standard OM approach (open squares). A difference of almost two orders of magnitude is observed in the region of low angular momenta, dominated by the strong absorption. The reduction of the absorption predicted by the CC calculations with respect to the OM results corresponds to an addition of flux in the elastic channel, which gives rise to the bump in the angular distribution at the largest angles (see Fig. 3.2, upper panel), thus generating the rainbow structure.

In the lower panel of Fig. 3.3 the deflection function (eq. (2.7)) for the ^{16}O +^{27} Al

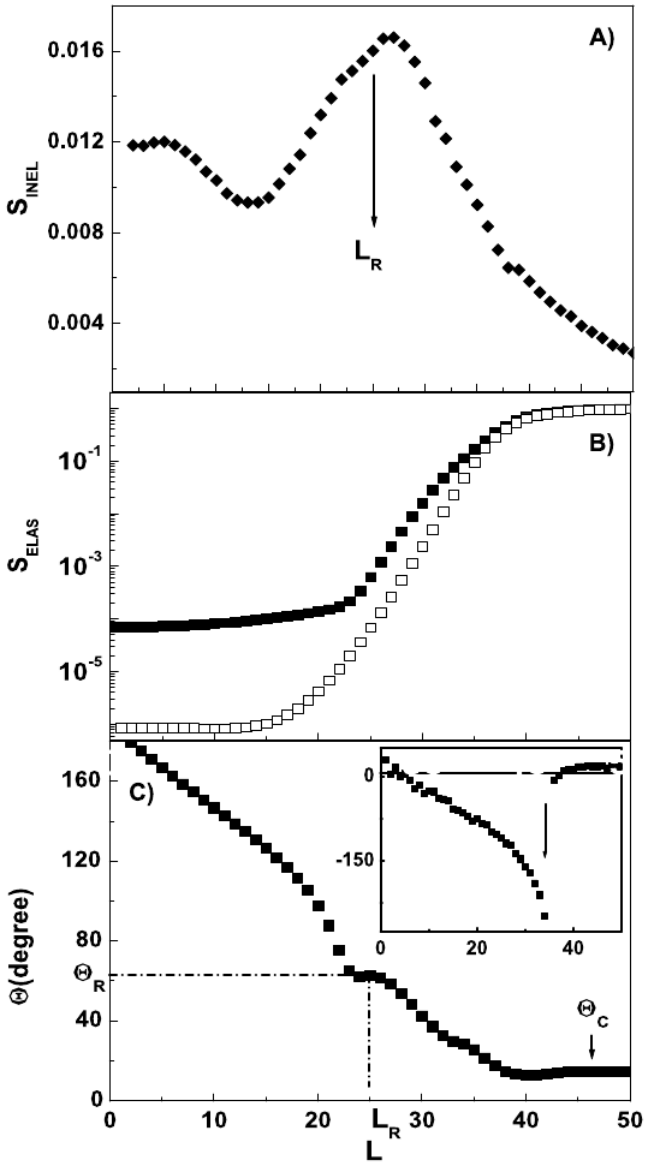

Figure 3.3: Panel A): the inelastic S-matrix for the ^{16}O +^{27} Al reaction at E_{lab} = 100 MeV. Panel B): the elastic S-matrix for the same reaction, given by CC calculations (closed squares) and OM calculations (open squares). Panel C): the corresponding deflection function calculated in the CC approach. The nuclear and Coulomb rainbow angles are indicated as Θ_R and Θ_C, respectively.

system calculated within the CC approach is shown. For the purpose of comparison, the classical deflection function (eq. (2.6)), obtained considering only the real part of the optical potential, is reported in the inset. An almost orbiting process is observed

for $L = 35$, corresponding to $\Theta \approx 350°$ (some classical trajectories for fixed ℓ values are shown in Fig. 3.4). The deflection function derived from the CC calculation, including

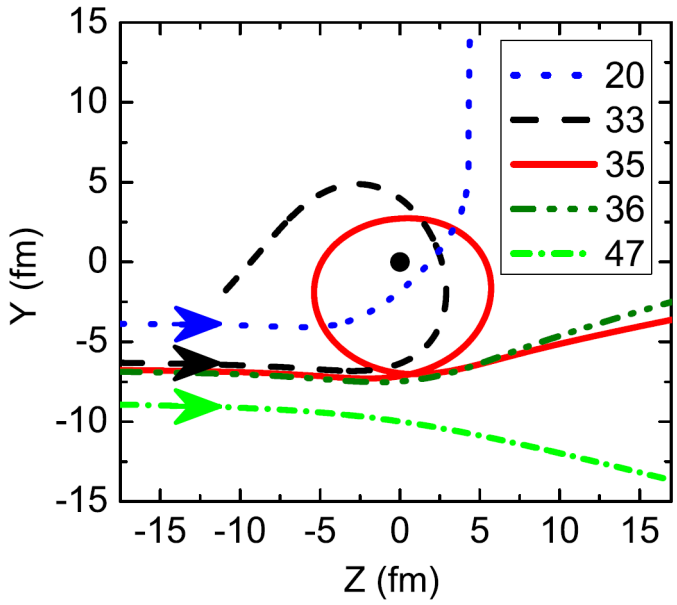

Figure 3.4: Classical trajectories for some ℓ values as indicated in the figure. An almost orbiting condition is reached for $\ell = 35$, which results in nearly the same scattering angle θ corresponding to $\ell = 36$. The closed circle represents the scattering center.

the imaginary part of the optical potential, is very different from its classical counterpart. The orbiting feature, in this case, is completely suppressed due to the strong absorption. A local maximum is observed around $L_R = 25$, corresponding to $\Theta_R \approx 63°$. This L value is close to the angular momentum for which the maximum in the inelastic S-matrix is observed (Fig. 3.3, panel A). Therefore, within the CC approach the nuclear rainbow scattering arises from inelastic couplings and consequently it is related to a positive contribution to the overall nucleus-nucleus imaginary potential due to the polarization.

The oscillation pattern in the experimental angular distribution of Fig. 3.1 is better seen in the expansion region shown in Fig. 3.5. As discussed in Chapter 1, the Airy-like minima observed in the data are expected when a system with small absorption is considered. Thus, the occurrence of this oscillation pattern for the ^{16}O +^{27} Al system at E_{lab} = 100 MeV can be related to a decrease of absorption, probably linked to the previously discussed Pauli Blocking effect or to other in medium effects [56]. The decomposition of the scattering amplitude in the nearside and farside components,

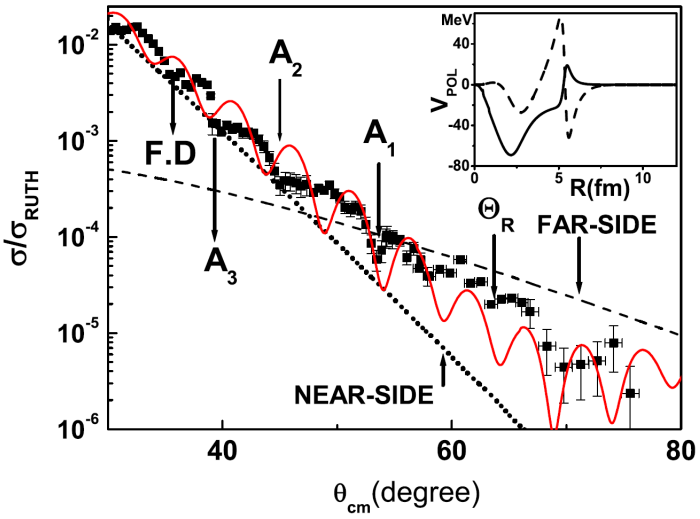

Figure 3.5: An expansion of the elastic angular distribution of Fig. 3.1. The observed Fraunhofer oscillations and Airy-like minima are indicated by the arrows. A decomposition of the scattering amplitude in the near/far side components, based on standard OM calculations, is also shown. The inset in the figure shows the real (solid line) and imaginary (dashed line) parts of the trivially equivalent polarization potential obtained from the CC calculations.

obtained from standard OM calculations (no coupling), is also shown. In this context, the Fraunhofer oscillations are explained in terms of interference between the nearside and the farside amplitude in forward direction. On the other hand, the behaviour of the distribution at large angles is dominated by the farside amplitude. The trivially equivalent polarization potential (TELP), obtained from the CC calculations, is shown in the inset of Fig. 3.5. This potential represents an average over the L-dependent polarizations. Strong oscillations of the real and imaginary components of the potential are observed near the barrier radius ($\sim$ 5 fm). The effect is particularly significant for the imaginary part, where the inclusion of the polarization effectively reduces the overall absorption around 5 fm, creating an absorption-free region, while increasing it around 6 fm. This behaviour is compatible with that observed for the elastic S-matrix (see Fig. 3.3, panel B), in which more absorption (when comparing the CC results with the OM ones) at large L-values and less absorption at small L-values is expected.
The results obtained for the ^{16}O +^{27} Al system at E_{lab} = 100 confirm the reliability of the SPP/CC calculations in this energy regime. Starting from these findings, the same elastic scattering process at the increased energy of 280 MeV is investigated in the

present work, since the SPP/CC calculations predict a nuclear rainbow structure in the elastic cross section angular distribution. The experimental set-up and data reduction technique, as well as the obtained results will be discussed in the following chapters.

Chapter 4

Experimental set-up

The experiment discussed in this thesis work has been performed at the Laboratori Nazionali del Sud (LNS-INFN) in Catania on February 2012. The primary $^{16}O^{3+}$ ions were produced by the Electron Cyclotron Resonance source (SERSE) and then accelerated by the k800 Superconducting Cyclotron (CS) at an energy of 280 MeV. The beam current was varied during the experiment according to the angular setting investigated, from the lowest value of about 5 enA at forward angles to the highest value of about 80 enA at large angles. The beam was shaped by the use of a collimation system, giving a beam spot size of about 1.2 mm horizontally and 2.3 mm vertically, guaranteeing a good matching with the optical properties of the MAGNEX spectrometer [18], used to analyse the reaction products.

The collimation system is made up of two main parts. The first one is composed of four slits, two for the horizontal and two for the vertical phase space, which can be electrically moved and are located along the beam line, 2 m upstream from the entrance of the scattering chamber. The second part is located inside the scattering chamber, upstream the target ladder, and is made up of a rectangular diaphragm (1 x 2 mm^2) mounted 15 cm far from the target and a 5 mm hole diaphragm, used as anti-scattering screen, mounted at a distance of 5 cm from the target. Both diaphragms are aligned with the beam axis. Thanks to this collimation system, it was possible to obtain horizontal and vertical beam divergences of ~ 0.8 mrad and ~ 3 mrad, respectively.

An accurate optical alignment is needed in order to make the beam hitting the target at the object point of the spectrometer. This request was fulfilled by the use of a bubble level, which made it possible to align the target ladder with the collimation system and

the beam line, with a precision within 0.1 mm.
The measurement of the beam current, necessary to retrieve the absolute cross section, was accomplished by a 8 mm Faraday cup, mounted inside the scattering chamber downstream the target ladder along the beam direction. An electron suppressor, negative polarized at -200 V, was used at the entrance hole of the cup in order to enhance the efficiency of the charge collection. The current signal was then sent from the experimental room to the acquisition room to a Digital Integrator [57]. The current values were stored in the memory of a Latching Scaler [58], monitoring, in this way, the beam intensity for the entire acquisition time.
The target used in the experiment was a 109 $\mu g/cm^2$ thick self-supporting ^{27}Al foil, mounted in the second position from the top of the target ladder.
A picture of the scattering chamber with the collimation system, the target ladder and the Faraday cup is shown in Fig. 4.1.

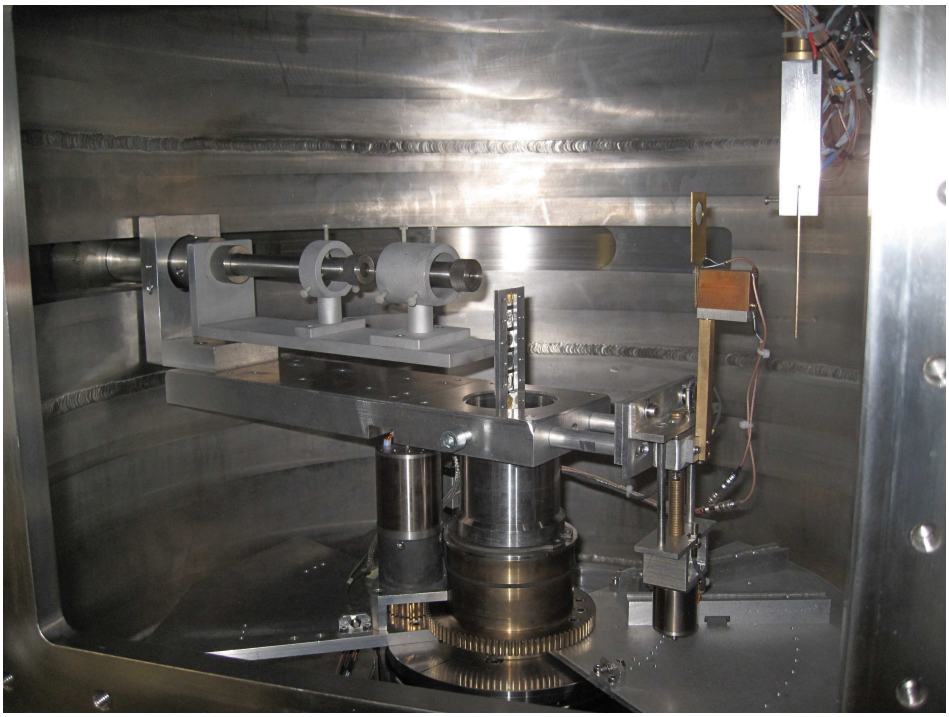

Figure 4.1: A picture of the scattering chamber. The collimation system, the target ladder and the Faraday cup are visible.

The ^{16}O ejectiles were momentum analysed by the MAGNEX spectrometer (see 4.1) working in full acceptance mode. This configuration corresponds to a solid angle

coverage of $\Omega \sim 50$ msr and a momentum range $\Delta p/p \sim 24\%$. Since the main target of the present experiment was the measurement of the elastic and inelastic angular distributions of the $^{16}O + ^{27}Al$ system, 5 different angular settings were chosen in order to have wider distributions. In particular, the spectrometer optical axis was located at $\theta_{opt}^{lab} = 10°$, 13°, 18°, 26°, 34° in the laboratory reference frame. Due to the large angular acceptance of the spectrometer ($-5.16°$, $+6.3°$ horizontal, $\pm 7.16°$ vertical), these angular settings correspond to a whole angular coverage $5° \leq \theta_{lab} \leq 40°$ in the laboratory frame.

4.1 The MAGNEX magnetic spectrometer

4.1.1 General features

MAGNEX [18, 59] is a large acceptance magnetic spectrometer installed at the LNS-INFN in Catania. It is a high-performance device, offering a high angular, mass and energy resolution, which can be employed for studies in different fields of nuclear research, ranging from nuclear structure to the characterization of reaction mechanisms in a wide interval of energies and masses [60]. Thanks to a good hardware and software compensation of the strong aberrations produced by the large acceptance elements, MAGNEX is able to merge the advantages of the traditional magnetic spectrometry [61] with those of a large angular and momentum acceptance device (50 msr the former, -14.3%, $+10.3\%$ the latter).

From the mechanical point of view, MAGNEX is composed of two large aperture magnets, a quadrupole (Q) followed by a 55° dipole (D), and a Focal Plane Detector (FPD) for the detection of the focused reaction products. A picture of the apparatus is shown in Fig 4.2.

The quadrupole magnet provides the focusing strength in the vertical plane, while the dipole gives the dispersion and the horizontal focusing strength through a rotation of $-18°$ of the entrance and exit dipole boundaries. The accepted magnetic rigidities range from 0.2 to 1.8 Tm, corresponding to energies of the detected ions ranging from 0.2 to 40 AMeV, depending on their mass and charge.

The requirements of large acceptance strongly constrained the design of MAGNEX. Severe limitations arise from the manufacture of the elements, from space limitations

Figure 4.2: The MAGNEX spectrometer installed at LNS-INFN. The two large magnets, the dipole (white-red) and the quadrupole (blue-white) are visible. The focal plane detector is located after the quadrupole, on the right side of the picture.

and from the disturbing effects on the optics of higher-order aberrations, always present when dealing with huge magnets. All these effects reduce the available phase space, that is the range of the detected angles and momenta with the required resolution. A sizeable improvement in the correction of aberrations is obtained by using special algorithms to reconstruct the relations between the initial phase space coordinates of the ions with those measured at the position of the focal plane detector. A detailed description of the method is reported in ref. [59]. The main actual parameters of MAGNEX, resulting from the best compromise between the calculated configuration described in [59] and the effective construction requirements, are reported in table 4.1.

4.1.2 The reference frame, matrix formalism and aberrations

Usually, the description of the motion of a beam of charged particles is done choosing one of them as the reference particle. Then, the momenta and paths of all the other particles through the magnetic elements are referred to those of the reference one, labelled as p_0 and l_0. The reference moomentum p_0 is also used to set the strength

Optical characteristics	Actual values
Maximum magnetic rigidity (Tm)	1.8
Solid angle (msr)	50
Horizontal angular acceptance (mr)	−90,+110
Vertical angular acceptance (mr)	±125
Momentum acceptance	−14%,+10%
Central path length (cm)	596
Momentum dispersion (cm/%)	3.68
First order momentum resolution	5400
Focal plane rotation angle (degrees)	59.2
Focal plane length (cm)	92
Focal plane height (cm)	20

Table 4.1: Main optical characteristics of the MAGNEX spectrometer.

of the bending magnets. In this way, it is possible to define a reference frame (**t**,**x**,**y**), with **t** defining the direction along the reference trajectory and the transverse axis **x** and **y** perpendicular to it. A schematic view of the reference frame adopted is shown in Fig 5.5.

In this reference frame, the momentum of a particle of the beam is decomposed in its p_x and p_y components along the x and y directions and the fractional deviation δ from the reference momentum, defined as $\delta = (p - p_0)/p_0$. However, the quantities $x' = p_x/p_t$ and $y' = p_y/p_t$ are usually chosen, where p_t is the momentum longitudinal component along the reference trajectory. Since p_x and p_y are small when compared to p_t, x' and y' can be approximated to the horizontal θ and vertical ϕ angles with respect to the reference trajectory (see Fig. 5.5). To have a complete phase space coordinate set it is necessary to have three more quantities: the two transverse distances of the particles from the central trajectory, x and y, and the path length difference between a given trajectory and the reference one, l. The path length is defined as the distance, along the particle trajectory, from the starting point of the beam line, i. e. the target position for magnetic spectrometry, to the intersection between the trajectory of the particle and a plane normal to the reference trajectory, at a fixed t. Summarizing, the complete phase space coordinate set for a generic particle can be written as $P \equiv (x, \theta, y, \phi, l, \delta)$.

Using this phase space representation, the motion of a charged particle beam, under the action of an external magnetic field, can be described as the dynamical evolu-

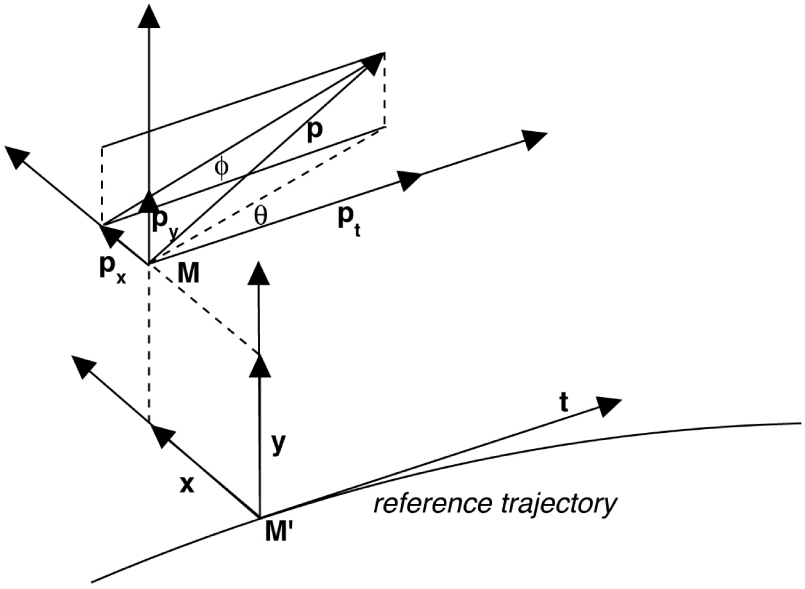

Figure 4.3: The reference frame adopted for the description of the motion of a beam of charged particles in a magnetic field.

tion of the hyper-volume occupied by the system. In particular, the final position $P_f \equiv (x_f, \theta_f, y_f, \phi_f, l_f, \delta_f)$ is obtained from the initial position $P_i \equiv (x_i, \theta_i, y_i, \phi_i, l_i, \delta_i)$ through a general non-linear transport relation, characteristic of the particular optical system:

$$F : P_i \longrightarrow P_f \tag{4.1}$$

The evolution of each single coordinate is given by:

$$\begin{aligned} x_f &= F_1\left(x_i, \theta_i, y_i, \phi_i, l_i, \delta_i\right) \\ \theta_f &= F_2\left(x_i, \theta_i, y_i, \phi_i, l_i, \delta_i\right) \\ y_f &= F_3\left(x_i, \theta_i, y_i, \phi_i, l_i, \delta_i\right) \\ \phi_f &= F_2\left(x_i, \theta_i, y_i, \phi_i, l_i, \delta_i\right) \\ l_f &= F_2\left(x_i, \theta_i, y_i, \phi_i, l_i, \delta_i\right) \\ \delta_f &= \delta_i \end{aligned} \tag{4.2}$$

where the last equation expresses the conservation of the ion momentum modulus in a magnetic field, when electric fields and degrading elements are absent. The F_i functions

completely describe the motion of the particles in the beam and are, in general, non linear functions. The l_i parameter is essentially constant for thin targets, so it will not be considered in the following. Exploiting the tensor notation, eq. (4.2) can be written in terms of Taylor expansion as:

$$x_i(f) = \sum_k R_{jk} x_k(i) + \sum_{k,l} T_{jkl} x_k(i) x_l(i) + \cdots \tag{4.3}$$

where x_j is the generic phase space coordinate and R_{jk} and T_{jkl} are the first and second order transfer matrix elements, respectively. The coefficients of the second and higher order terms in eq. (4.3) are usually referred to as *aberrations* [62], since they determine deviations from the ideal first order optical properties. They are called *chromatic aberrations* if they contain derivatives respect to the momentum (i.e., if they are momentum dependent), otherwise they are just *geometrical aberrations*. The main advantage when using the tensor formalism lies in the fact that, for a complex magnetic system, R and T are given by the product of the corresponding tensors of each single magnetic element [63]. In general, these systems are solved through numerical algorithms.

For small deviations from the reference trajectory and momentum, eq. (4.3) can be written as:

$$P_f \approx R P_i \tag{4.4}$$

where R is the first order transport matrix:

$$R = \begin{pmatrix} (x|x) & (x|\theta) & (x|y) & (x|\phi) & (x|l) & (x|\delta) \\ (\theta|x) & (\theta|\theta) & (\theta|y) & (\theta|\phi) & (\theta|l) & (\theta|\delta) \\ (y|x) & (y|\theta) & (y|y) & (y|\phi) & (y|l) & (y|\delta) \\ (\phi|x) & (\phi|\theta) & (\phi|y) & (\phi|\phi) & (\phi|l) & (\phi|\delta) \\ (l|x) & (l|\theta) & (l|y) & (l|\phi) & (l|l) & (l|\delta) \\ (\delta|x) & (\delta|\theta) & (\delta|y) & (\delta|\phi) & (\delta|l) & (\delta|\delta) \end{pmatrix} \tag{4.5}$$

where the notation $(a|b) = (\partial a_f / \partial b_i)_0$.

The R matrix returns a good description of the particles dynamics only if the first order approximation of the Taylor expansion (4.3) is valid. This is true when beam lines or magnetic spectrometers with small angular and momentum acceptance are considered. Conversely, higher order terms of the expansion (4.3) are needed when dealing with large-acceptance spectrometers, like MAGNEX [64].

An important feature of the R matrix (4.5) is the possibility to direct link most of its first order elements to general properties of the beam transport line. As an example, the elements of the 6^{th} column are related to the effects caused by the momentum dependence, thus they are referred to as *dispersive terms*. In particular, the $R_{16} = (x|\delta)$ element gives the horizontal dispersion D, which corresponds to the horizontal separation, after a dispersive region, between two trajectories for which the difference in momentum is 1%. The R_{16} parameter is fundamental for the characterization of a spectrometer, since it determines the horizontal position resolution required for the focal plane detector to obtain the aimed momentum resolution.
The crucial problem of aberrations is faced in MAGNEX using hardware tricks and sophisticated software algorithms. From the hardware point of view, a partial compensation of the aberrations has been obtained with a carefully shaping the magnets, choosing, for example, the best effective field boundaries for the dipole, and using other specific solutions, like the rotation of the Focal Plane Detector with respect to the spectrometer optical axis, a system to shift it of ± 10 cm and the introduction of correction coils inside the dipole [18]. Anyhow, hardware solutions cannot solve alone the problem of aberrations, so a sophisticated software correction has been implemented, based on a fully algebraic approach in determining the ion trajectories inside the spectrometer [65]. The technique, called *Ray-Reconstruction technique*, requires an accurate magnetic fields mapping of the spectrometer [66–69], the use of powerful algorithms to solve high-order transport equations [70] and a precise measurement of the ions positions and directions at the FPD, described in the next Section.

4.2 The MAGNEX Focal Plane Detector

The MAGNEX Focal Plane Detector is a gas-filled hybrid detector with a wall of 60 Si detectors at the back, designed for measuring the horizontal and vertical coordinates and angles of each incident particle, the energy loss in the gas region and the residual energy released in the silicon detectors wall. A detailed description of the detector is reported in ref. [19]. The FPD main features are discussed in the following Sections.

4.2.1 FPD layout

The detector is basically made up of a proportional drift chamber divided in five sections, four of which are position-sensitive, and a wall of silicon detectors at the back in order to stop the focused reaction products [71, 72]. A schematic view of the FPD detector is given in Fig. 4.4. The FPD is placed 1.91 m downstream the exit pole face

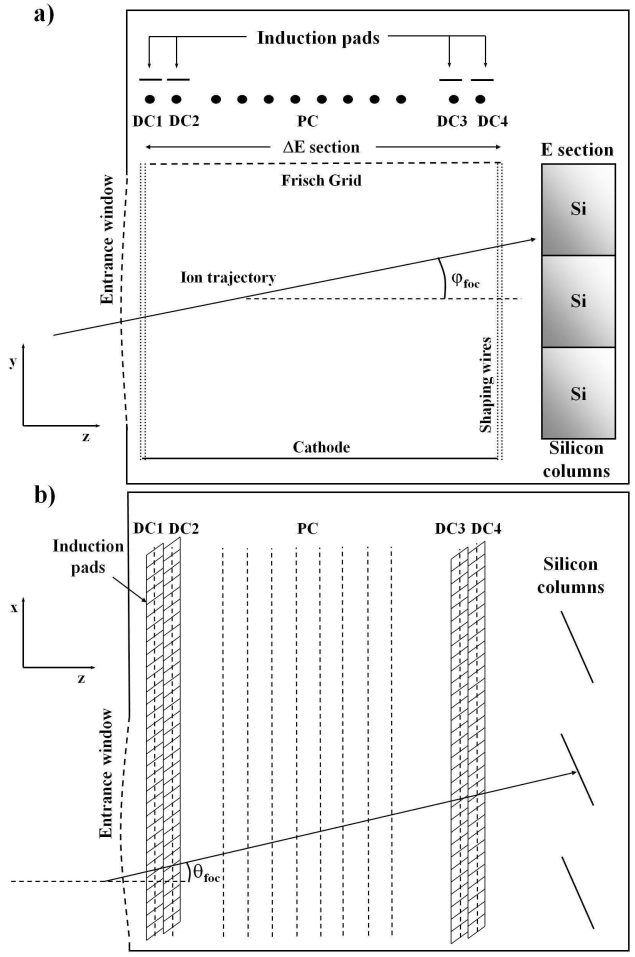

Figure 4.4: Schematic side (a) and top (b) views of the MAGNEX Focal Plane Detector.

of the dipole magnet. According to ion optics calculations [59, 64], this is the position at which the focal plane of the spectrometer is defined. The FPD vessel is mounted on a movable carriage which can translate of ±0.08 m along the spectrometer optical axis, in order to match the detector position to different focus conditions. The FPD entrance surface is rotated of an angle $\theta_{tilt} = 59.2°$ with respect to a plane normal to

the central reference trajectory. As already said, the rotation of the FPD is a hardware solution in order to reduce the effect of chromatic aberrations [64].
The drift chamber active volume is 1360 mm wide × 200 mm high × 96 mm deep. The cathode plate is located at the bottom of the chamber. The applied working voltages are usually in the range $-(900 \div 1500)$ V. The typically used gas is 99.95 % pure isobutane at pressures between 5 and 100 mbar, depending on the experimental conditions. The gas purity and pressure are preserved through a continuous flowing system. A 1.5 μm Mylar entrance window separates the gas region from the vacuum region. This window, of 920 × 220 mm^2 area, is supported by 20 silicon coated stainless multistrand wires 0.5 mm in diameter, arranged horizontally and spaced 1 cm from each other.
The Frisch grid, connected to the ground and placed in the opposite side with respect to the cathode plate, is made up of 10 gold-plated tungsten wires, 50 μm in diameter, spaced 5 mm between centers. A partition grid, consisting of 41 rectangular rings parallel to the cathode and arranged at 5 mm one to the other, guarantees the uniformity of the electric field in the 200 mm high drift region between the cathode and the Frisch grid.
The proportional counter section includes 5 sets of gold-plated tungsten amplifying wires, sequentially defined as DC1, DC2, PC, DC3, DC4 (see low panel of Fig. 4.4), located 20 mm above the Frisch grid and spaced 8 mm apart. Each DC wire is a unique amplifying wire 20 μm diameter, while the PC wires, made up of 8 single wires connected in common, are thicker (100 μm). The working voltages, varying in the range $+(600 \div 1300)$ V, are provided by a common power supply.
A set of 224 induction pads, parallel to the spectrometer optical axis, is located 5 mm above each DC proportional wire. The entire patterned electrode is engraved on a six-layered 6 mm thick printed circuit board. Each pad is 8 mm long and 5.9 mm wide, separated by 0.1 mm from its neighbour. A picture of the anodic plate is shown in Fig. 4.5.

The residual energy of the focused ions is measured by a wall of 60 silicon pad detectors placed at the back of the FPD. The detectors, with an active area of 70 mm height × 50 mm width and 500 μm in thickness, are arranged in 20 columns and 3 rows, rotated in order to have the active area perpendicular to the spectrometer reference trajectory, as shown in Fig. 4.6.

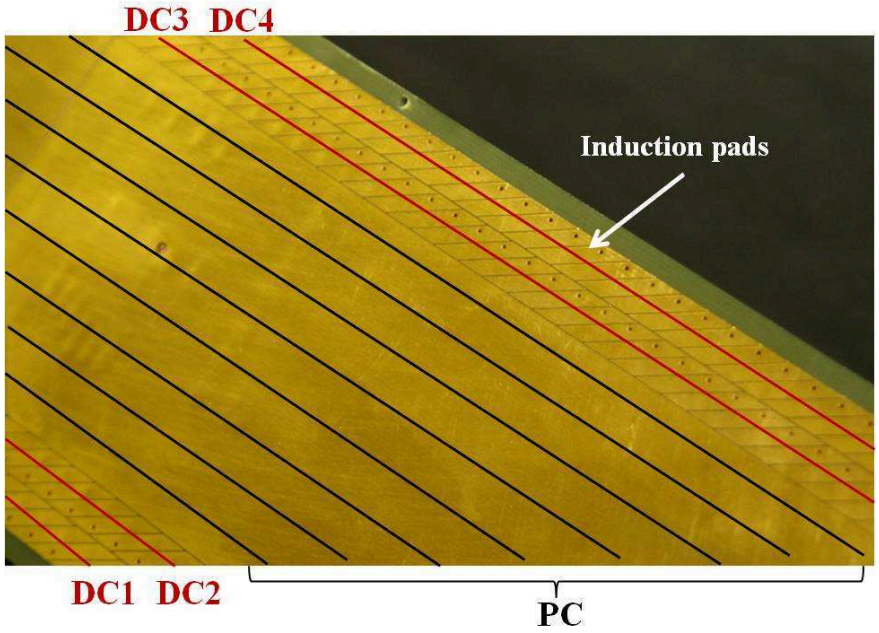

Figure 4.5: Picture of the anodic plate showing the segmented strips and the DC and PC proportional wires.

The columns are mechanically supported and electrically connected by a mother board built on a 6 mm thick multi-layer printed circuit. The motherboard also hosts the charge preamplifiers [73], which therefore operate in the low pressure gas environment.

4.2.2 Operating mode

When the ions deflected by the dipole enter the FPD gas region, they produce ionized atoms and primary electrons along their path (see upper panel of Fig. 4.4). Under the action of the uniform electric field of about 50 V/cm, these electrons are accelerated towards the Frisch grid, with velocities varying according to the pressure and voltage conditions [74]. Beyond the grid, a secondary electrons production takes place due to a growing electric field, which reaches higher values in the proximity of the DC and PC wires, where a multiplication factor of about 100-200 for each primary electron can be reached. The avalanche produces a signal proportional to the ions energy loss in each section, thus providing five measurements for each event (ΔE_1, ΔE_2, ΔE_{CP}, ΔE_3, ΔE_4). Charge sensitive preamplifiers with a sensitivity of 200 mV/MeV (silicon equivalent) [75] are used to shape the signals, which have typical rise time of about 150

Figure 4.6: The MAGNEX FPD silicon detectors. The columns are rotated in order to let the detectors show their active area perpendicular to the reference trajectory.

ns. Then a 16-channels NIM module splits the amplified signals before sending them to a shaping amplifier and a Constant Fraction Discriminator with a 200 ns delay time. The shaped output, proportional to the energy loss and with a shaping time of 6 μs, is used for the particle identification, while the logic output, extracted only for the DC wires, is used as the stop signal for the electrons drift time measurement. A scheme of the electronic chain for the read-out of the detector signals is shown in Fig. 4.7.

The information on the horizontal position and angle (X_{foc}, θ_{foc}) of the ion track at the focal plane is retrieved thanks to the signal induced by the electron avalanche on the closest induction pads. These signals are pre-amplified and shaped by an analog multiplexed read-out system based on 16-channels GASSIPLEX chips [76] and digitally converted by C-RAMS modules [77]. A dedicated algorithm [78] is used to extract the center of gravity of the charge distribution at each DC section. Exploiting the regular pattern of the segmented electrode, it is possible to obtain a unique correspondence between the measured centroid and the horizontal position X_1, X_2, X_3, X_4 in meter units.

The silicon wall at the back of the FPD provides the measurement of the residual energy of the impinging ions. The logic outputs are used as multi-purpose timing signals of MAGNEX. The logic OR, for example, is used as start signal for the electrons drift

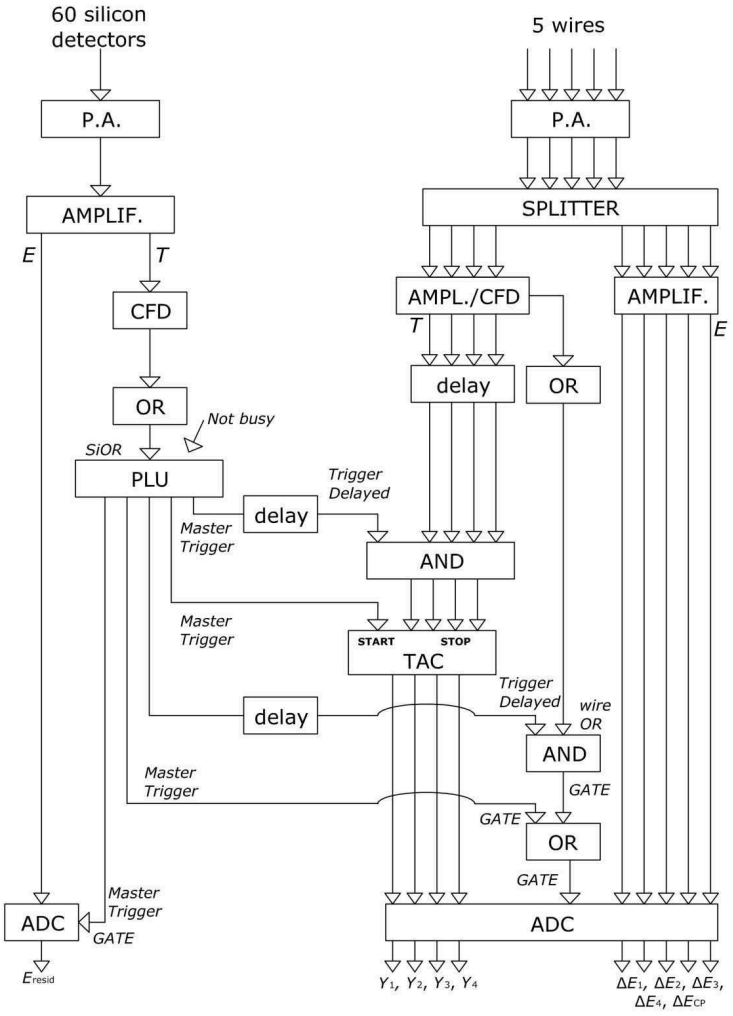

Figure 4.7: Schematic diagram of the read-out electronic chain of the E_{resid}, Δ_{E_i} and Y_i measurements.

time, as trigger for the data acquisition and to generate the ADC gate signal for the ΔE and drift time measurements. The four vertical positions Y_1, Y_2, Y_3 and Y_4 are extracted from the measurement of the electron drift time in the gas region, given by the time interval between the signal generated by the silicon detectors and the DC wires,

measured via a standard TAC - ADC read-out system. Thanks to an almost constant drift velocity of the electrons in the gas, the vertical positions and angles (Y_{foc}, ϕ_{foc}) at the focal plane are thus determined.

4.3 Spectrometer settings

4.3.1 Quadrupole and dipole magnetic fields

The choice of the correct magnetic fields settings for the quadrupole and the dipole is imposed by the condition of focusing the ^{16}O ions corresponding to the ground state of the ^{27}Al residual nuclei at the focal plane position. These magnetic fields are calculated using the COSYsetup program [79], specifically designed for searching the best parameters to set-up large magnetic apparata. When the kinematic parameters of the studied reaction and the desired δ ($\delta = 0.05$ in the present case) are given as input, the COSYsetup program searches the correct magnetic field settings among a sample of tabulated values, calculated for several different configurations. The current value of the quadrupole magnetic field is determined from the high precision measurement of the supplied current. Moreover, four permanent Hall probes, placed at 0.1815 m from the quadrupole symmetry axis, are used to monitor long term drifts and possible hysteresis effects. The dipole magnetic field is measured by a NMR probe inserted in a socket of the magnetic vacuum chamber. A detailed map of the field given by the manufacturer makes possible to extract the magnetic field strength at each point of the beam envelope, with an estimated error of $\sim 0.1\%$ [67]. The spectrometer parameters for each angular setting investigated are reported in table 4.2.

Setting	$\boldsymbol{\theta_{lab}^{opt}}$ (deg)	$\mathbf{B\rho}$ (Tm)	$\mathbf{B_Q}$ (Tm)
1	10	0.71782	0.66754
2	13	0.71280	0.66098
3	18	0.70326	0.65031
4	26	0.68113	0.62640
5	34	0.68113	0.62640

Table 4.2: Dipole and quadrupole magnetic fields for each investigated setting.

4.3.2 FPD settings

The Focal Plane detector was filled with the 99.95% pure C_4H_{10} isubutane gas at a pressure of 15.06 mbar. The cathode plate was supplied with -1200 V, whereas the Frisch grid was grounded. The voltage applied to the proportional wires DC1, DC2, DC3, DC4 and to the PC wires was +750 V, while a separated generator supplied the lateral shaping partition grid between the Frisch grid and the proportional wires with -430 V. The silicon detectors at the back of the FPD were powered with 60 V in a full depletion mode. Finally, a -0.09 m shift of the FPD was adopted for all the measurements.

Chapter 5

Data reduction

Data reduction is a complex procedure made up of several steps. A basic issue, characteristic of MAGNEX, is that the horizontal and vertical positions and angles measured by the FPD must be transformed in the three-dimesional reference frame where the objects points and the magnetic field maps are defined. This condition, which is a pre-requisite to solve the equation of motion of the detected particles, is achieved by proper calibrations of the data based on accurate optical and mechanical measurements. In addition, the ^{16}O ejectiles must be identified, since the elastic scattering process ^{27}Al(^{16}O,^{16}O)^{27}Al is investigated in this work. The identification procedure is based on the standard $\Delta E - E$ technique for the atomic number (Z). Then the mass number (A) is determined by the correlation between the measured ion positions at the focus and the kinetic energy. Once the ions track are measured at the focal plane position, it is possible to optimize the spectrometer transport map up to the 10^{th} order. This procedure, later described in detail, completely characterizes the investigated event, providing the ion kinetic energy and scattering angle in the laboratory reference frame. Moreover, it allows to take into account the loss of the transmission efficiency through the spectrometer. This aspect is of fundamental importance in order to extract the absolute cross section values of the investigated reaction.

5.1 Calibration of the horizontal and vertical positions

5.1.1 X calibration

As discussed in Chapter 3, the four X positions of the ion track inside the gas region of the Focal Plane Detector are given by the response of the induction pads above each DC wire. Before extracting the horizontal positions, a relative calibration of the pads response is mandatory. This request is fulfilled using a digital pulser and sending four negative pulses, with 0.05 μs rise time, 1 μs width and increasing amplitude (-2, -4, -6, -8 V), directly to each DC wire. In this way the same charge is instantly induced in each pad above a given wire, and the corresponding "GASSIPLEX" histograms are constructed. A reference pad is chosen for a given DC wire and a linear fit procedure is performed in order to relate the response of each induction pad to that of the reference one. An example of this correlation procedure is shown in Fig. 5.1.

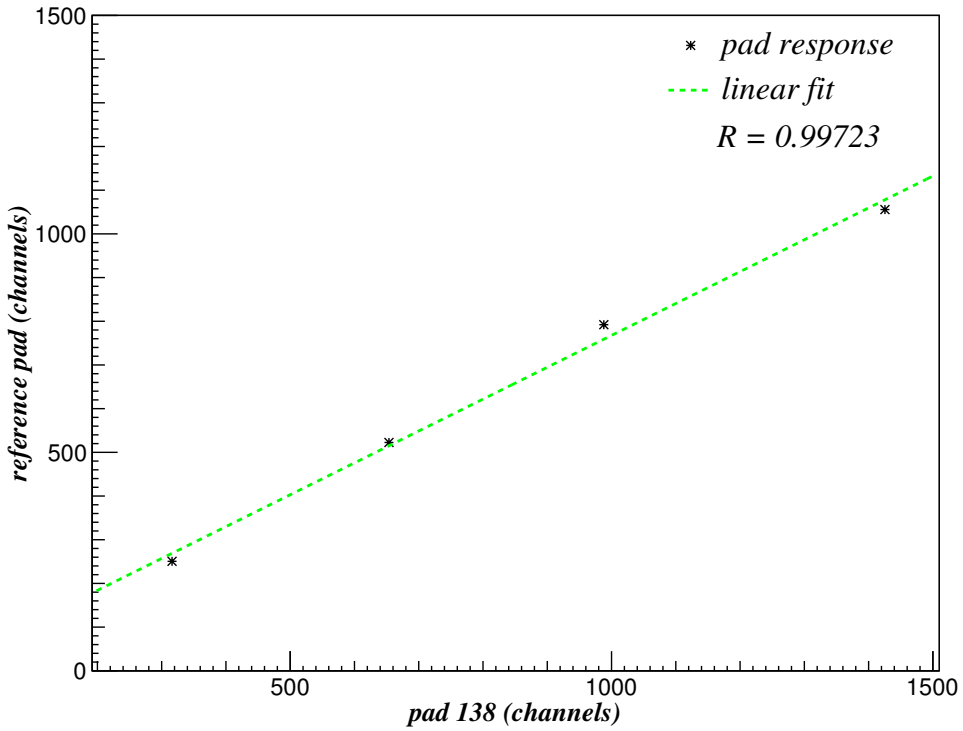

Figure 5.1: Linear fit procedure correlating the response of a given pad (DC2-138 in this case) with that of the reference one (DC2-24).

Once the relative pads calibration is obtained, the center of gravity of the charge distribution is extracted using a dedicated algorithm [78]. The algorithm described in ref. [78] has been specifically developed for the MAGNEX FPD to account for the large variation of the number of excited pads as a function of the incident angle. This effect causes very different shapes of the charge distributions, thus making any standard centroid-finding algorithm [80, 81] quite unreliable.
The horizontal positions X_1, X_2, X_3, X_4 are finally determined from the corresponding centroid positions, considering that each pad is 6.00 ± 0.01 mm wide. Using the known ΔZ_i longitudinal distances (downstream the optical axis) of the DC wires with respect to DC1, it is possible to reconstruct the ion horizontal track inside the detector, as shown in Fig. 5.2 for a typical event.

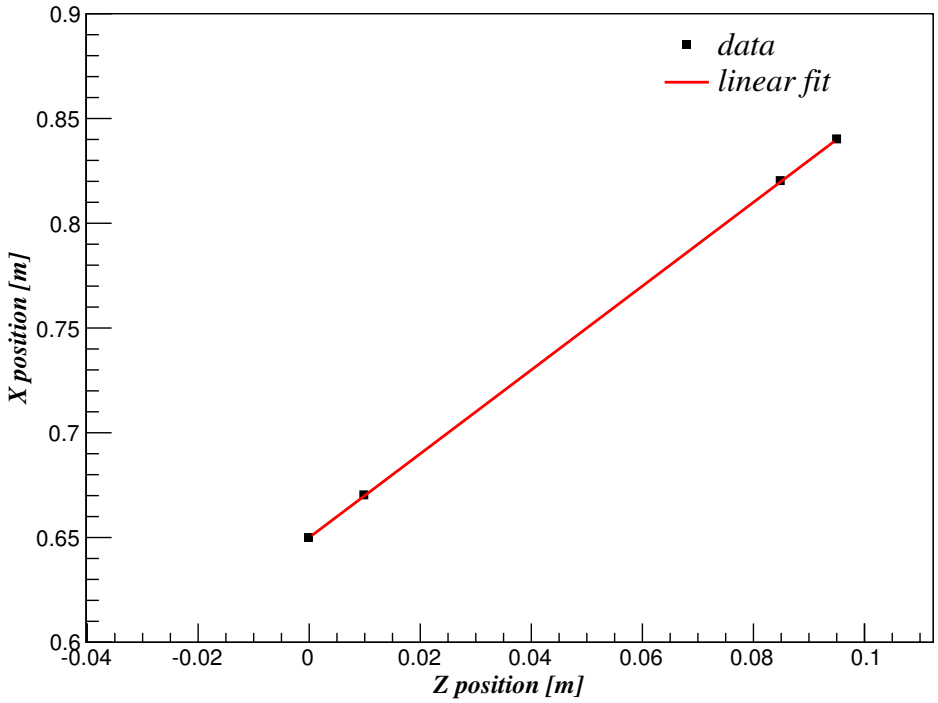

Figure 5.2: The linear correlation between the X_i positions for a typical event detected by the FPD and the ΔZ_i distances between the four DCs wires.

The zero for the horizontal positions X_i are extracted by the intersection between the spectrometer optical axis determined by a precision theodolite and the pad-pattern

above each DC_i. The X_{foc} coordinate at the focal plane is finally obtained taking into account the measured position at the FPD downstream the optical axis Z_{foc} (see Fig. 5.2). The angular coefficient of the track (see Fig. 5.2) gives the horizontal angle θ_{foc}. The X_{foc} and θ_{foc} parameters are used as inputs for the ray-reconstruction technique.

5.1.2 Y calibration

The calibration of the ions vertical position at the focal plane requires a procedure different from that used for the horizontal position, since, in this case, no mechanical references can be easily exploited. It was thus necessary to build an *ad-hoc* system in order to face this task. This system, shown in Fig. 5.3, consists of a metallic plate with 14 horizontal slits and a collimated α source, mounted on a moveable arm placed in front of the FPD Mylar entrance window.

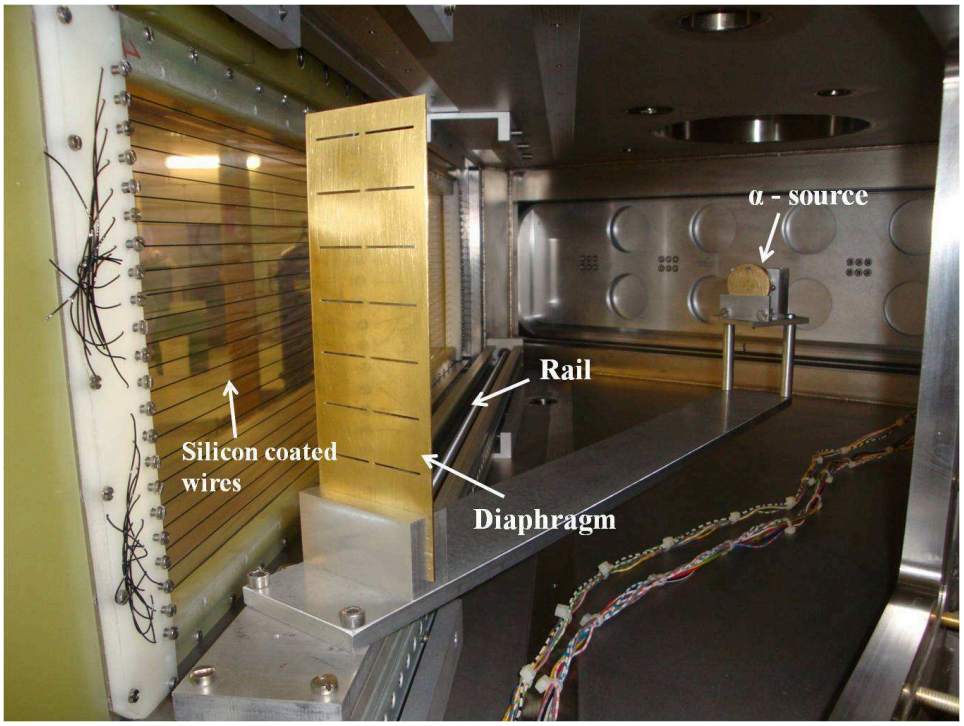

Figure 5.3: The *ad-hoc* system used for the calibration of the vertical position.

The slits, paired in 7 groups, are 1 mm wide and 26 mm long. Each group is 20 mm separated in height. The system was placed parallel to spectrometer optical axis, as shown in the picture. In this configuration, only the α particles passing through the

slits will be detected, producing a characteristic $Y_i - X_{foc}$ image, as shown in Fig. 5.4.

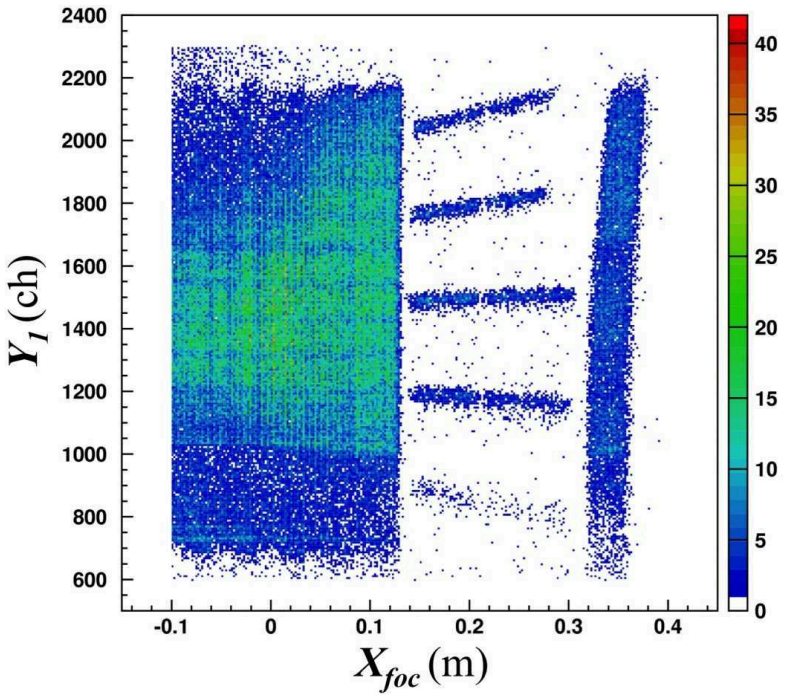

Figure 5.4: $Y_1 - X_{foc}$ scatter plot using the vertical position coordinate measured by the DC1 wire. The lines correspond to the α particles passing through the slits. The continuous background is due to those particles on the sides of the screen. Geometrical perspective effects make the slits images vertically inclined.

The absolute vertical position of the α source 1 mm diameter emitting hole with respect to the spectrometer symmetry plane was determined using a precision bubble-level. The same was done to determine the positions of the slits. The XYZ coordinates of an α particle at the FPD can be determined using the schematic frame reported in Fig. 5.5 and are given by the system of equations:

$$\begin{cases} X = X_\alpha + t\,(X_O + \Delta X - X_\alpha) \\ Y = Y_\alpha + t\,(Y_O - Y_\alpha) \\ Z = Z_\alpha + t\,(Z_O + \Delta Z - Z_\alpha) \end{cases} \tag{5.1}$$

where $(X_\alpha Y_\alpha Z_\alpha)$ are the absolute coordinates of the emitting source, the O index indicates the central axis of the diaphragm and ΔX, ΔZ represent the x and z projections of the slit, respectively, connected by the relation $\Delta Z = -\Delta X \tan\theta_{tilt}$ (Fig. 5.5).

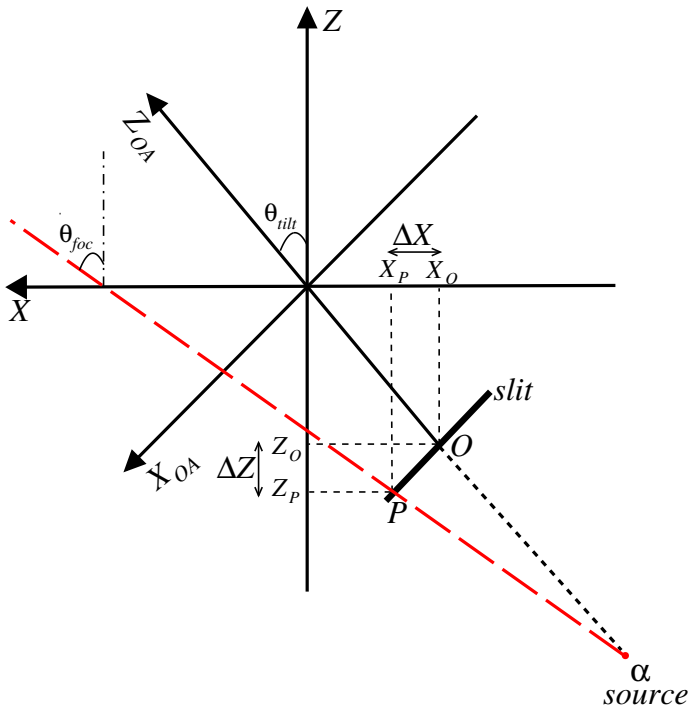

Figure 5.5: Schematic plane view of the coordinate system used to derive the system of equations (5.1). A general point $P(x_P, z_P)$ and the central point $O(x_O, z_O)$ of the slit are indicated. The dashed red line represents the trajectory of an α particle passing through the P point.

The vertical position of each trajectory can be therefore evaluated through the system (5.1), since the Z_i coordinates are accurately determined for each DC wire and the X_i are measured. It is then possible to obtain the absolute Y_i calibration from a linear fit between the evaluated vertical positions and the measured ones, ad shown in Fig. 5.6 for the Y_1 position.

Since it was not possible to move the arm to illuminate the entire FPD, the possible dependence of the Y_i positions on the X_i ones was not fully explored in this way. It was thus necessary a secondary calibration. This was done exploiting the shadows generated by the silicon coated wires used to support the Mylar window (see Fig. 5.3), which are clearly seen in a typical Y_i spectrum (Fig. 5.7) as regularly spaced minima.

Since the position of each wire is well known by accurate optical measurements, the absolute Y_i calibration is obtained comparing the position of the holes in the Y_i

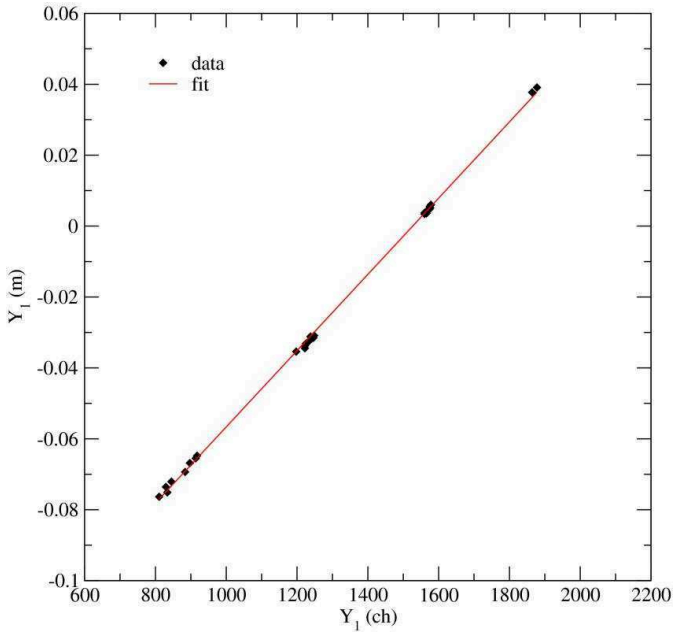

Figure 5.6: Linear fit correlating the measured vertical position Y_1 (channels) to the expected positions Y_1 (m) calculated using the system (5.1). The measured positions refer to the loci representing the slits images shown in Fig. 5.4.

spectrum with the projection of the wires at each DC vertical plane. Following the same procedure adopted for the X_i calibration, the Y_i vertical positions were used to draw the ion track inside the FPD detector in the YZ plane, obtaining the Y_{foc} coordinate, while the vertical angle ϕ_{foc} is extracted from the angular coefficient of the track. Both Y_{foc} and ϕ_{foc} are used as inputs for the ray-reconstruction technique.

5.2 The identification of the ^{16}O ejectiles

The next step in the data reduction procedure is the identification of the ^{16}O ions. The different particles detected by the Focal Plane Detector are separated in atomic mass number Z using the standard $\Delta\mathrm{E} - \mathrm{E}$ technique, based on the Bethe-Bloch formula [82]. An example of the Z discrimination of the different ions detected in the ^{27}Al(^{16}O,^{16} O)^{27}Al reaction for one silicon detector is shown in Fig. 5.8.

The energy loss in the ΔE_{CP}^{corr} plot is the measured energy deposited by the ions in

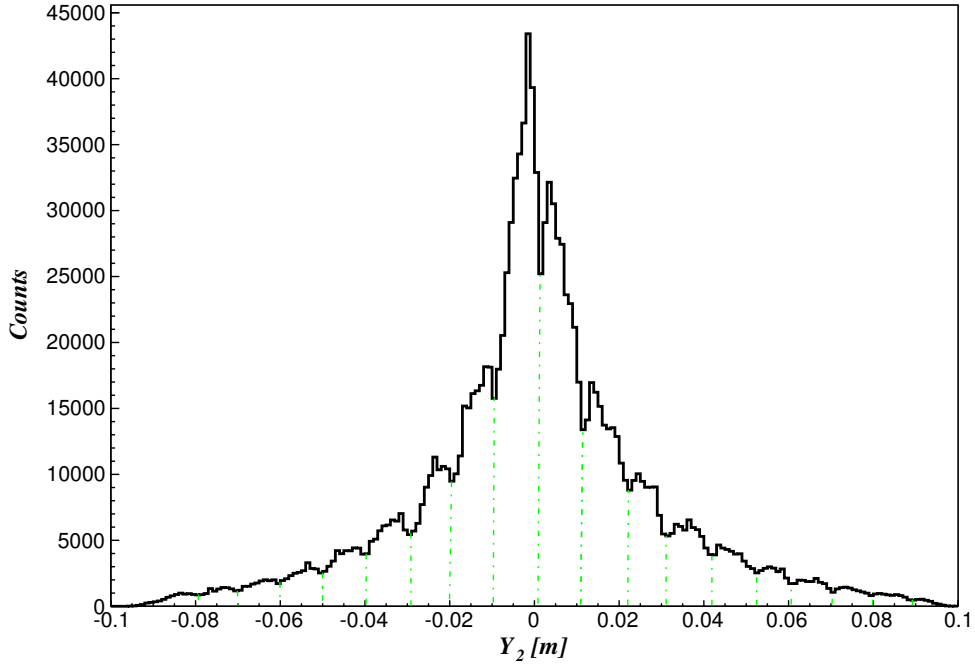

Figure 5.7: A typical Y_2 spectrum showing the regularly spaced minima due to the shadows generated by the silicon coated wires which hold the Mylar entrance FPD window. The position of the minima is indicated by the green dot-dashed lines.

the gas region, corresponding to the PC wires, corrected for the different path lengths associated to different horizontal angles θ_{foc}, according to the relation:

$$\Delta E_{CP}^{corr} = \Delta E_{CP} \frac{\cos\theta_{tilt}}{\cos\theta_{foc}} \tag{5.2}$$

where θ_{tilt} is the angle of the FPD with respect to a plane normal to the spectrometer optical axis ($\theta_{tilt} = 59.2°$). The residual energy, reported in abscissa, is the energy measured by the silicon detectors beyond the focal plane. It is not necessary to get a very accurate ΔE_{CP}^{corr} and E_{resid} in MeV since these quantities are used just for identification purposes.

The plot reported in Fig. 5.8 clarifies that the $\Delta E - E$ technique allows the Z discrimination of the different detected ions, but the isotopic resolution for a given ion is not achievable. The A identification is instead achieved through the correlation between the ions trajectory and their kinetic energy [83]. The motion of a charged particle

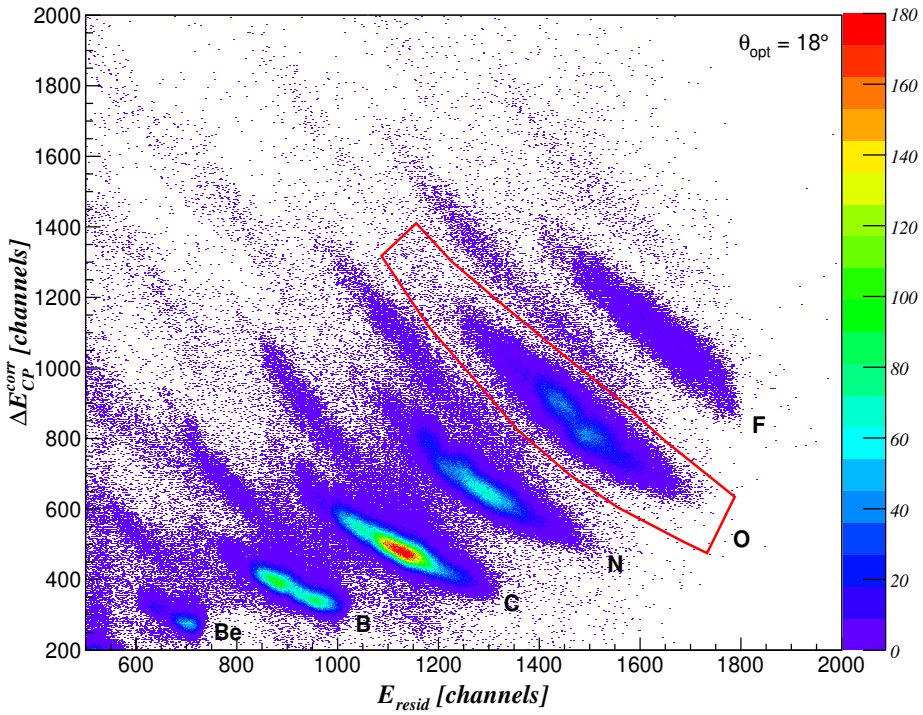

Figure 5.8: Bi-dimensional $\Delta E_{CP}^{corr} - E_{resid}$ scatter plot for a single silicon detector for the $\theta_{opt}^{lab} = 18°$ angular setting. The different ions detected in the ^{27}Al(^{16}O,^{16} O)^{27}Al reaction are clearly separated in atomic mass number Z.

moving across a uniform magnetic field is described by the relation:

$$\mathbf{B}\rho = \frac{\mathbf{p}}{q} \tag{5.3}$$

where $\mathbf{B}$ is the magnetic induction which forces the particle with charge q and momentum $\mathbf{p}$ to move on a trajectory with curvature radius ρ. In the non-relativistic limit, $p \simeq \sqrt{2mE_{resid}}$ and being ρ related to the position at the focal plane X_{foc}, the relation (5.3) can be transformed as:

$$X_{foc}^2 \propto \frac{m}{q^2} E_{resid} \tag{5.4}$$

where m is the ion mass. As a consequence, the trajectories of different isotopes of a given ion will be distributed on separated loci, according to the m/q^2 parameter, when an $X_{foc} - E_{resid}$ plot is constructed. An example of the method is shown in Fig. 5.9 for the O ions selected by a graphical cut applied to the identified Oxygen locus,

represented by the closed red contour in Fig. 5.8.

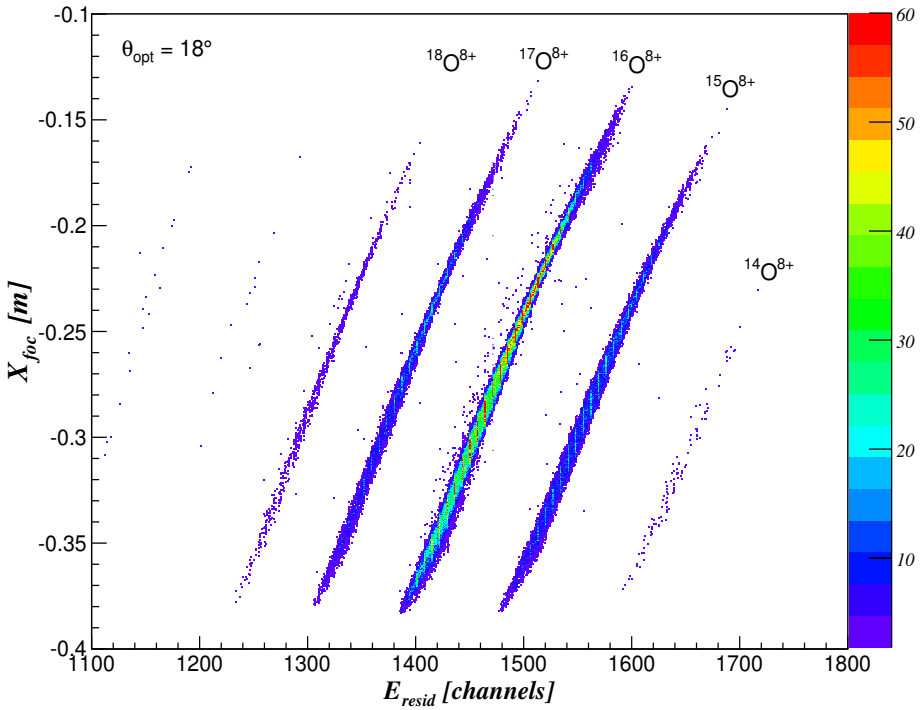

Figure 5.9: Bi-dimensional $X_{foc} - E_{resid}$ scatter plot for a single silicon detector after selecting the O locus in the $\Delta E_{CP}^{corr} - E_{resid}$ plot via the graphical cut represented by the closed red line in Fig. 5.8. The clear separation among the different Oxygen isotopes is clearly visible.

Fig. 5.9 shows the isotopic separation achieved in this way. The selected events are distributed on separated loci according to their mass and charge states. It is therefore possible to sort out only the $^{16}O^{8+}$ ions, as required in order to study the events corresponding to the elastic scattering process.

The described identification procedure is then repeated for each silicon detector, using each time the AND condition between the Oxygen identification in the $\Delta E_{CP}^{corr} - E_{resid}$ plot and the $^{16}O^{8+}$ selection in the $X_{foc} - E_{resid}$ plot. In this way, a unambiguous selection of all the detected ions of interest is obtained.

5.3 Analysis of the focus

The analysis of the correlations between the X_{foc}, θ_{foc}, Y_{foc} and ϕ_{foc} phase space parameters allows to study the focusing conditions determined during the experiment.

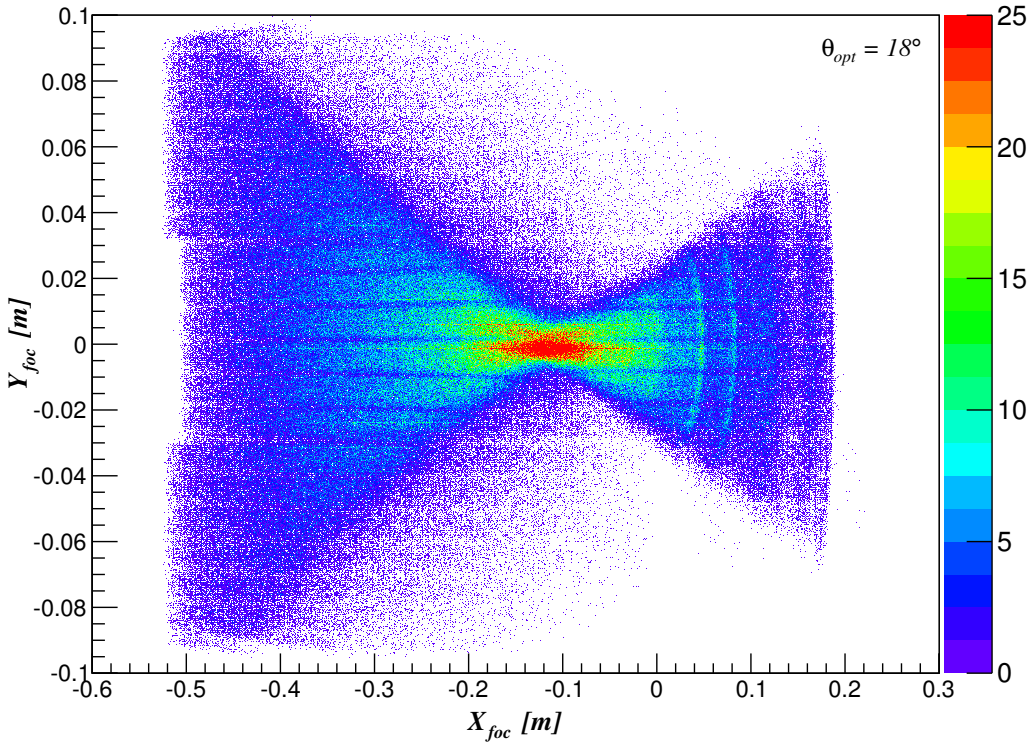

Figure 5.10: Bi-dimensional $Y_{foc} - X_{foc}$ scatter plot for the selected $^{16}O^{8+}$ ions in the ^{16}O + ^{27}Al elastic scattering at 280 MeV for the $\theta_{opt} = 18°$ angular setting.

As an example, the plot in Fig. 5.10 shows the typical "*butterfly*" shape for the XY distribution at the focal plane, which is due to the focusing effect of only those trajectories having the proper momentum $\delta' = 0.05$. The trajectories characterized by a momentum $\delta \neq \delta'$ are either over-focused ($\delta < \delta'$) or under-focused ($\delta > \delta'$) due to chromatic aberrations [59]. The $X_{foc} = 0$ position in the abscissa corresponds to the spectrometer optical axis. The observed shift of the center to negative X values indicates that the quadrupole field focused ions with rigidity Bρ 1% smaller than the reference one. The horizontal lines seen in the plot are the shadows produced by the silicon coated wires supporting the FPD Mylar window (Fig. 5.3). The almost vertical

correlated loci in the right side of the plot correspond to the ground state ($X_{foc} \approx 0.18$ m) and low lying excited states of the residual ^{27}Al nucleus. These appear in the focal plane region corresponding to a relative momentum $\delta' = 0.05$, as expected from the chosen magnetic field settings discussed in Section 4.3.1. These loci are not exactly vertical due to non negligible third and higher order aberrations in the vertical phase space, especially emphasized in the focal plane region far from the optical axis.
The ground and excited states populated in the residual nucleus are better seen in a $\theta_{foc} - X_{foc}$ scatter plot, shown in Fig. 5.11 for the same events of Fig. 5.10.

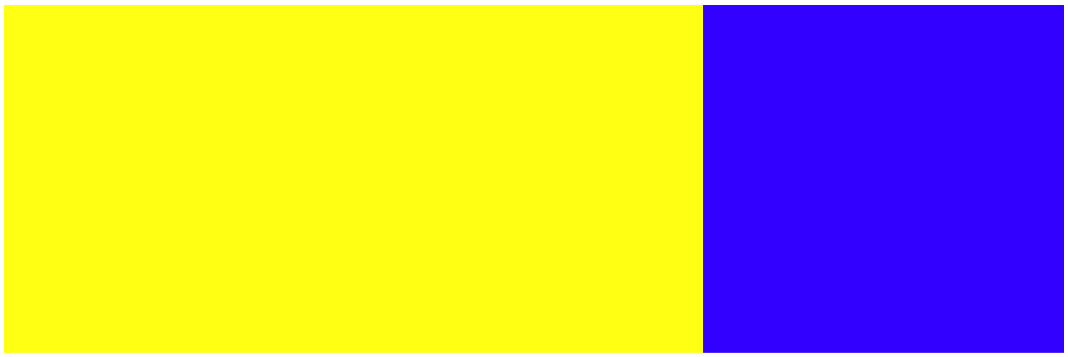

ions elastically scattered from Carbon and Oxygen contaminants present in the target. In addition to the horizontal phase space aberrations, the curvature of the states is affected also by the kinematic effect [64].

5.4 The ray-reconstruction technique

The ray-reconstruction procedure is a fundamental step of the data reduction, since it allows to retrieve the ejectile momentum vector at the target and thus to reconstruct the reaction Q value and the scattering angle. The practical implementation of the method is organized in two sequential steps described in detail in Sections 5.4.1 and 5.4.2.

5.4.1 Creation and simulation of the direct transport map

The starting point of the ray-reconstruction technique is the construction of the direct transport map F of equation (4.1), necessary to describe the evolution of the phase space parameters from the target position to the focal plane. For the MAGNEX spectrometer, this task is achieved using the COSY INFINITY program [84], in which the solution of equation (4.1) up to the 10^{th} order is obtained by Runge Kutta integration technique, based on the formalism of the differential algebra [70, 85]. The standard input file for COSY INFINITY contains the geometrical layout of the spectrometer (positions of the magnetic elements, length of the drift spaces, size and location of the FPD) and the values of the quadrupole and dipole magnetic fields used, which are described as three-dimensional Enge functions [86].
Once the direct transport map F is created, an accurate check is mandatory. Therefore, the ^{16}O + ^{27}Al elastic scattering at 280 MeV is simulated for each investigated angular setting using specific Monte Carlo routines [79]. In the simulations, the beam energy needs to be properly corrected to take into account the target straggling effect on both the projectile and the ejectile, respectively, since COSY INFINITY does not take into account energy losses. Using the scheme reported in Fig. 5.12 and assuming that the reaction takes place in the middle of the target, the *effective* beam energy is evaluated as follows:

- the impinging ^{16}O energy loss in the first half of the target is evaluated by the LISE++ program [87], giving the corrected energy $E'_{^{16}\text{O}}$;

- $E'_{^{16}\mathrm{O}}$ is used as input of the program CATKIN [88], which calculates by relativistic kinematic transformations the energy $E''_{^{16}\mathrm{O}}$ of the ejectiles produced in the ^{27}Al(^{16}O,^{16} O)^{27}Al scattering at the given angle θ_{opt};
- using again LISE++, the energy loss of the ^{16}O ejectiles in the remaining half target crossed with angle θ_{opt} is evaluated, obtaining $E^{fin}_{^{16}\mathrm{O}}$.

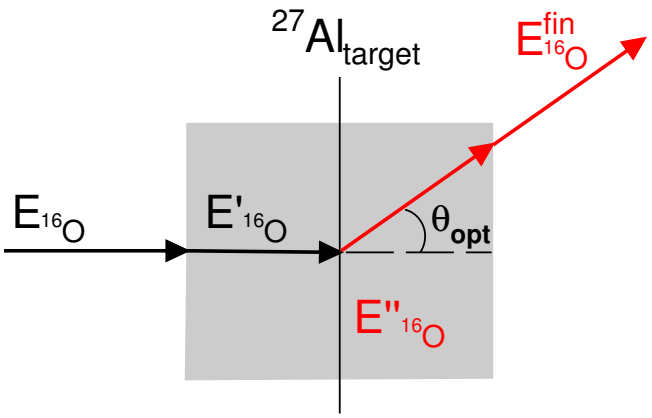

Figure 5.12: Schematic layout for the evaluation of the effective beam energy in the Monte Carlo simulation of the studied nuclear process.

The final energy $E^{fin}_{^{16}\mathrm{O}}$ is then taken as the reference one. Starting from this value and using CATKIN, the effective beam energy $E^{eff}_{^{16}\mathrm{O}}$ is found. This is defined as the beam energy necessary to generate by the same process ^{16}O ejectiles emitted at θ_{opt} with energy $E^{fin}_{^{16}\mathrm{O}}$, without any energy loss. In the data discussed in this work, due to the relatively high beam energy (280 MeV) and to the use of a thin target (109 μg/cm^2), the effective beam energy was found practically unchanged (within 100 keV) with respect to the nominal value for all the investigated angular settings.
Once all the input parameters are available, the simulation can be performed. As discussed above, the quality of the procedure is checked comparing the simulated final phase space parameters with the experimental ones. In Fig. 5.14 and 5.13 an example of the comparison with the data set of Fig. 5.10 5.11 is shown.

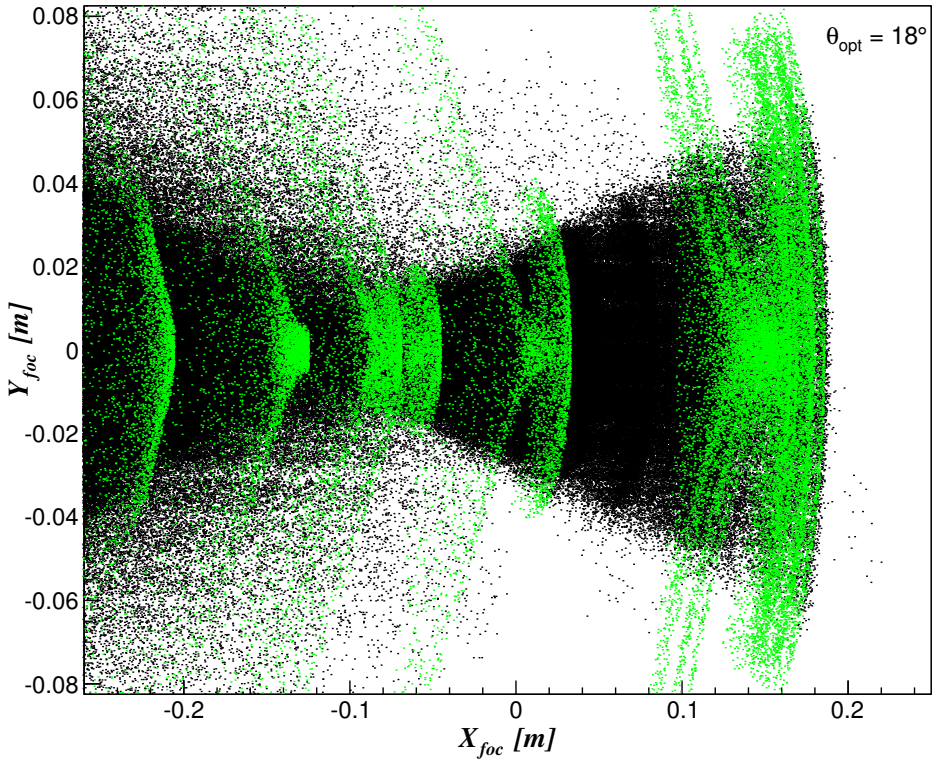

Figure 5.13: $Y_{foc} - X_{foc}$comparison between the experimental data (black points) and the simulated ones (green points).

A very good agreement of the simulated events (green points) with the experimental ones (black points) both in the $\theta_{foc} - X_{foc}$ plot and in the $Y_{foc} - X_{foc}$ plot, i.e. both in the horizontal and vertical phase space, is achieved. It is important to stress that the simulated states correspond to well defined excitation energies of the target nucleus, distributed in a discrete way on the whole spectrometer momentum acceptance. Moreover, a very accurate modelling of the dipole Effective Field Boundaries was necessary to obtain such result. The accuracy of the description of the final phase space by the application of the direct transport operator F is estimated in about -0.5 ± 0.9 mm and 3 ± 5 mr in X_{foc} and θ_{foc}, respectively. Similar values were found in ref. [65].

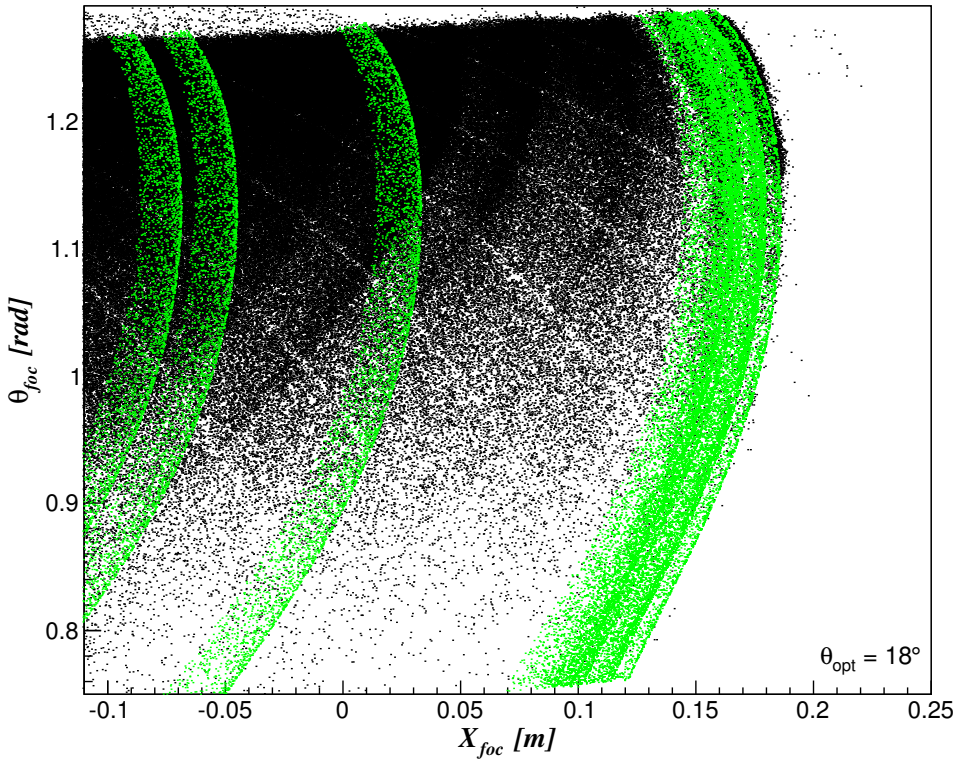

Figure 5.14: $\theta_{foc} - X_{foc}$ comparison between the experimental data (black points) and the simulated ones (green points).

5.4.2 The inverse transport map and its application to the experimental data

The second step of the ray-reconstruction procedure consists in the inversion of the direct transport map and the use of F^{-1} for the calculation of the momentum vector at the target location from the phase space parameters measured at the focal plane. An iterative procedure implemented in COSY INFINITY allows to construct the inverse transport map F^{-1} up to very high order (10^{th} in the case of MAGNEX). As a result, each initial phase space parameter, for example θ_i, is given by:

$$\theta_i = \sum_{n=1}^{10} \left(\frac{\partial^n \theta_i}{\partial x_f^m \partial \theta_f^p \partial y_f^q \partial \phi_f^r} \right)_{opt} \cdot x_f^m \theta_f^p y_f^q \phi_f^r \qquad \text{with } (m+p+q+r) = n \tag{5.5}$$

The effects of the high order aberrations described in Section 4.1.2 are largely compensated by this procedure.

The final step of the ray-reconstruction procedure is the application of the inverse transport map to the measured $(X_f, \theta_f, Y_f, \phi_f)$ vectors. The distribution of the events in the reconstructed initial horizontal and vertical $\theta_i - \phi_i$ angles for the same data of Fig. 5.8 is shown in Fig. 5.15.

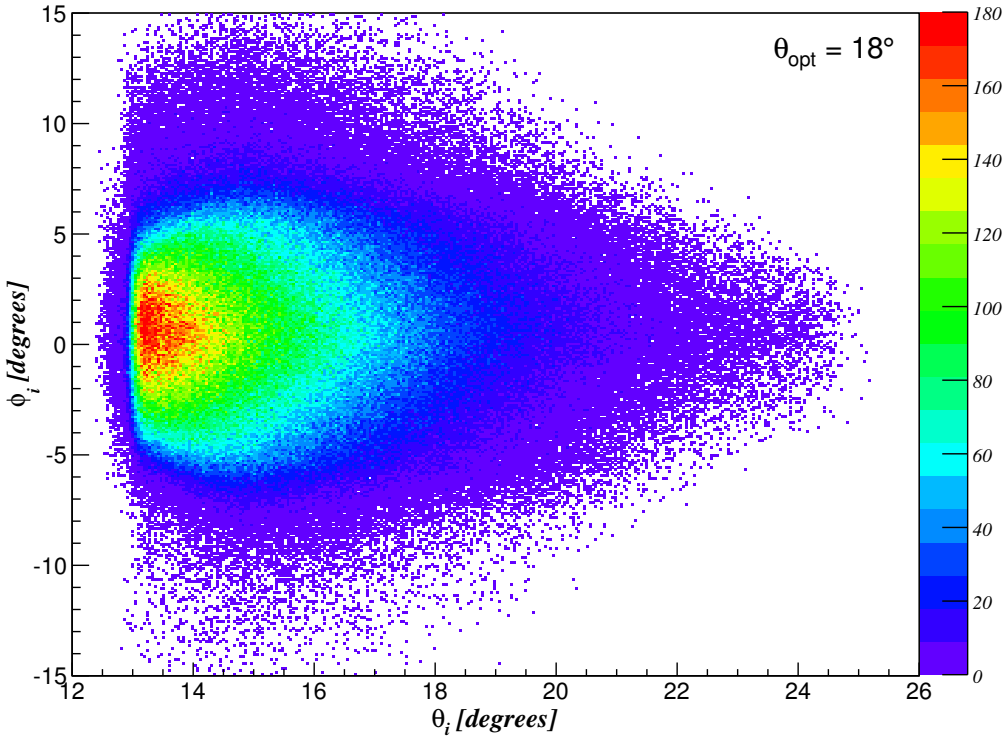

Figure 5.15: Reconstructed distribution of the events in the $\theta_i - \phi_i$ plane for the same data set of Fig. 5.8.

The plot in the figure indicates how the events are correctly reconstructed, since they are inside the real spectrometer acceptance ($-7.16° < \phi_i < 7.16°$ and $-5.16° + \theta_{opt} < \theta_i < 6.3° + \theta_{opt}$), with a slight shift (specificare) towards positive ϕ_i. In an ideal case, the events distribution should have a rectangular shape. However, the limited transmission efficiency of the spectrometer, especially at the borders, has been shown [89] to be due to cut-off of the beam envelope from the vacuum vessels. Nevertheless, this effect can

be accurately taken into account in the cross section angular distribution extraction procedure, as demonstrated in ref. [65] for the study of the ^{16}O +^{197} Au Rutherford scattering.

Using simple geometrical relations, it is possible to extract the scattering angle in the laboratory frame θ_{lab} starting from the initial angles θ_i and ϕ_i through:

$$\theta_{lab} = \arccos \frac{\cos(\theta_{opt}) - \sin(\theta_{opt}) \tan(\theta_i)}{\sqrt{1 + \tan^2(\theta_i) + \tan^2(\phi_i)}} \tag{5.6}$$

while the residual nucleus excitation energy E_x is calculated through a missing mass calculation, supposing a binary reaction:

$$E_x = Q_0 - Q = Q_0 - K\left(1 + \frac{M_e}{M_r}\right) + E_b\left(1 - \frac{M_p}{M_r}\right) + 2\frac{\sqrt{M_p M_e}}{M_r}\sqrt{E_b K}\cos(\theta_{lab}) \tag{5.7}$$

where Q is the reaction Q-value, M_e, M_r and M_p are the ejectile, residual and projectile masses, respectively. K is the ejectile kinetic energy, linked to the reconstructed δ parameter, E_b represent the beam energy and Q_0 is the ground state to ground state Q-value for the transition ($Q_0 = 0$ in the specific case of the elastic scattering process). The last two quantities, θ_{lab} and E_x, are used to construct bi-dimensional plots in which the ground and excited states of the residual ^{27}Al nucleus become evident, as shown in Fig 5.16 for the data set of Fig. 5.8. The ^{27}Al ground state and the low lying excited states are clearly visible as well correlated straight loci, since the reconstructed ^{27}Al excitation energy does not depend on the scattering angle. The curved loci, starting from $E_x \sim 6$ MeV, correspond to ^{16}O ions elastically scattered from ^{16}O (red dashed line) and ^{12}C (blue dashed lines) contaminants present in the ^{27}Al target, as already seen in Fig. 5.11. The efficiency cut at $E_x \sim 84$ MeV is due to the finite spectrometer acceptance [89].

The described procedure has been applied to the reconstructed events at $\theta_{opt}^{lab} = 10°$, $\theta_{opt}^{lab} = 13°$, $\theta_{opt}^{lab} = 26°$ and $\theta_{opt}^{lab} = 34°$. The result for the last data set is shown Fig. 5.17. The $\theta_{lab} - E_x$ distributions show how the adopted data reduction technique makes it possible to identify the ^{27}Al ground state and low lying excited states even at the largest angles, where the yield becomes extremely low. It will be shown that in this angular region the measured absolute cross section reaches values as low as 10^{-5} mb/sr.

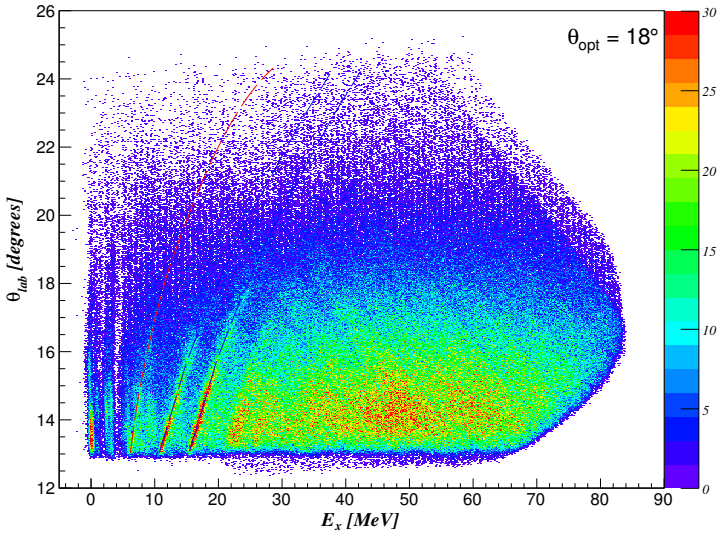

Figure 5.16: Reconstructed distribution of the events in the $\theta_{lab} - E_x$ plane for the same data set of Fig. 5.8. The ^{27}Al ground state and low lying excited states are clearly visible as well correlated straight loci. The curved loci, starting from $E_x \sim 6$ MeV, correspond to ^{16}O ions elastically scattered from ^{16}O (red dashed line) and ^{12}C (blue dashed lines) contaminants.

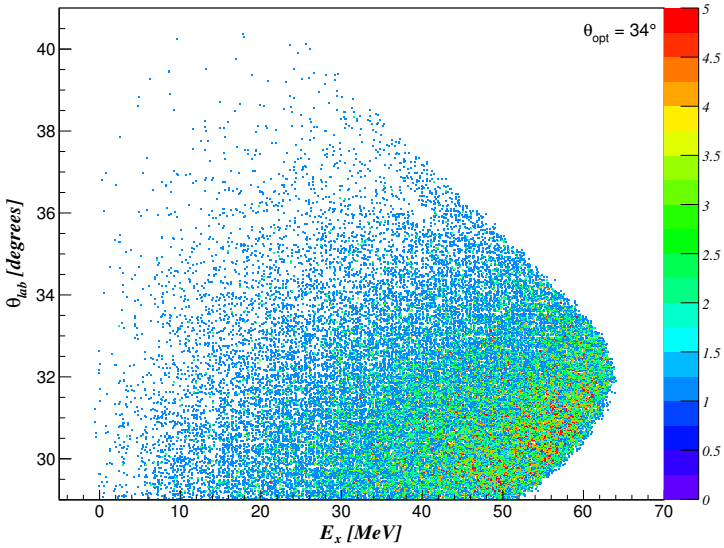

Figure 5.17: Reconstructed distribution of the events in the $\theta_{lab} - E_x$ plane for the data set at $\theta_{opt}^{lab} = 34°$. The ^{27}Al ground state is still visible despite the low yield.

5.5 Excitation energy spectra

The excitation energy spectra of the residual ^{27}Al nucleus are obtained from the $E_x - \theta_{lab}$ plots projecting the events on the E_x axis, after selecting fixed angular step slices in scattering angle θ_{lab}. The spectra resulting from the sum of all the slices for each experimental setting are shown in Fig. 5.18, 5.19, 5.20, 5.21, 5.22.

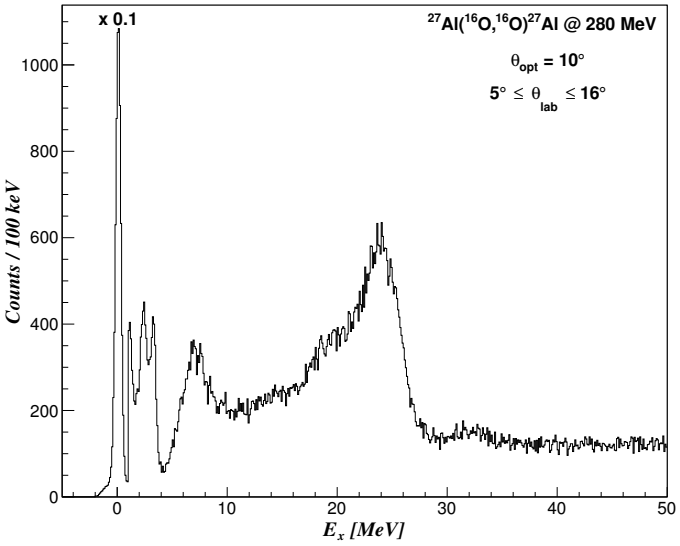

Figure 5.18: Excitation energy spectrum of the residual ^{27}Al nucleus for the data set at $\theta_{opt}^{lab} = 10°$. The data are integrated in the angular range $5° \leq \theta_{lab} \leq 16°$.

State	J^{π}	**Excitation energy** (MeV)
g.s.	$5/2^+$	0
1	$1/2^+$	0.844
2	$3/2^+$	1.015
3	$5/2^+$	2.735
4	$7/2^+$	2.212
5	$9/2^+$	3.004

Table 5.1: ^{27}Al low lying states populated in the ^{27}Al(^{16}O,^{16} O)^{27}Al reaction at 280 MeV.

The ^{27}Al ground state and low lying excited states populated in the ^{27}Al(^{16}O,^{16} O)^{27}Al scattering process are clearly visible in the spectra, even at the largest angles, where the yield is very low and the continuum is dominant (the scaling factors are indicated

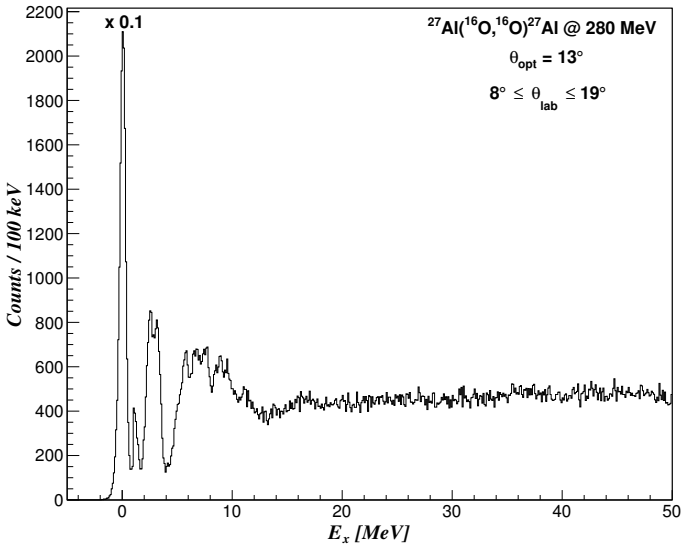

Figure 5.19: Excitation energy spectrum of the residual ^{27}Al nucleus for the data set at $\theta_{opt}^{lab} = 13°$. The data are integrated in the angular range $8° \leq \theta_{lab} \leq 19°$.

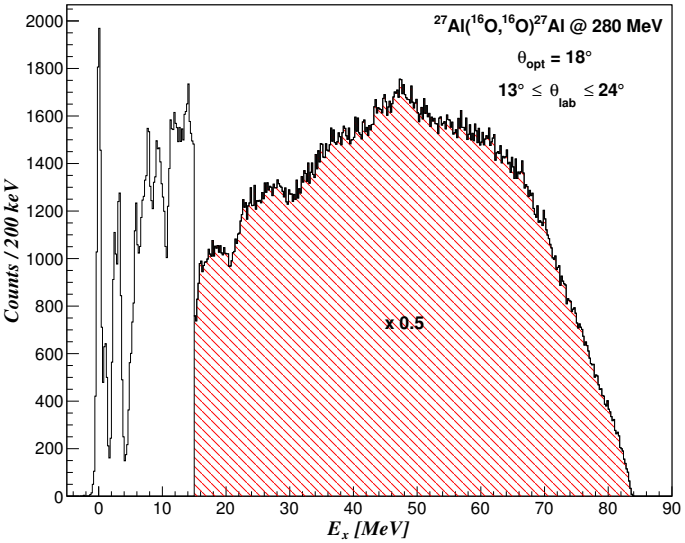

Figure 5.20: Excitation energy spectrum of the residual ^{27}Al nucleus for the data set at $\theta_{opt}^{lab} = 18°$. The data are integrated in the angular range $13° \leq \theta_{lab} \leq 24°$.

in the hatched areas). A list of the observed low lying states is reported in table 5.1. A Gaussian fit procedure, applied to the observed peaks, gives a mean energy resolution

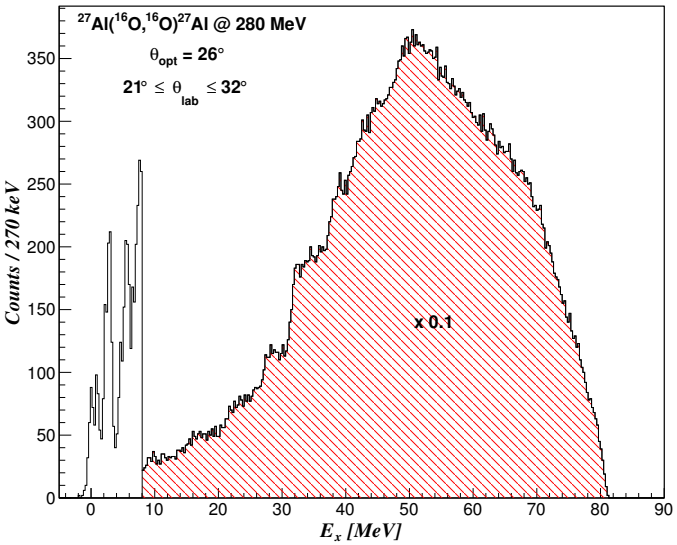

Figure 5.21: Excitation energy spectrum of the residual ^{27}Al nucleus for the data set at $\theta_{opt}^{lab} = 26°$. The data are integrated in the angular range $21° \leq \theta_{lab} \leq 32°$.

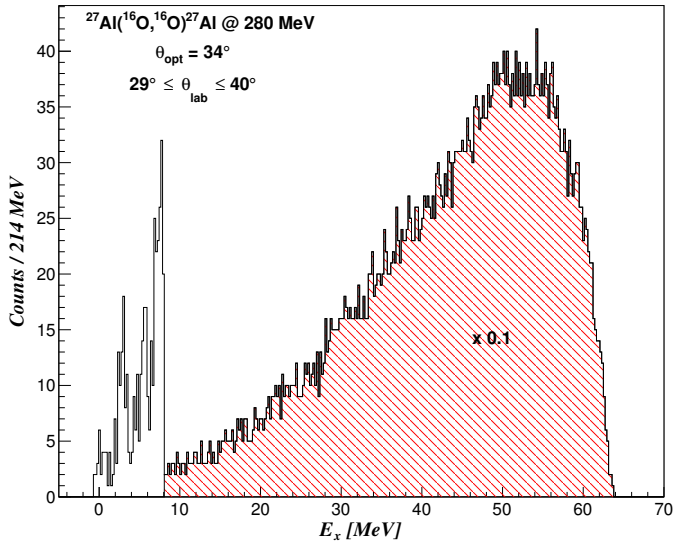

Figure 5.22: Excitation energy spectrum of the residual ^{27}Al nucleus for the data set at $\theta_{opt}^{lab} = 34°$. The data are integrated in the angular range $29° \leq \theta_{lab} \leq 40°$.

of about 550 keV (FWHM) in all the shown spectra. This resolution is affected by four main contributions. The first one is the spectrometer finite energy resolution, estimated

in about 1/900 [65], corresponding, in this case, to about 300 keV. The beam resolution, which is about 1/1000, is the second factor to take into account contributing, like the previous case, for about 300 keV. The straggling effect induced by the target thickness accounts for about 150 keV, considering ^{16}O ions passing through the 109 μg/cm^2 ^{27}Al target foil. Finally, the kinematic effect, which is angle dependent, plays a relevant role especially at the largest scattering angles, since it determines contributions to the energy resolution ranging from $\sim$ 100 keV at 10° to $\sim$ 600 keV at 40°. The obtained resolution is good enough to safely separate the elastic peak from the inelastic ones, allowing the extraction of the elastic and inelastic angular distributions for all the data sets (see 5.6).
The excitation energy specta at forward angles are of particular interest, since two huge bumps are observed at $E_x \sim 24$ MeV: they arise from the excitation of Quadrupole and Monopole Giant Resonances modes, as investigated in more details in next Chapter.

5.6 Cross section angular distributions

The final step of the data reduction procedure is the extraction of the cross section angular distributions for the identified transitions. This represents the main target of the present work, since nuclear rainbow evidences are expected in the elastic ^{16}O + ^{27}Al angular distribution.
As already discussed, the large angular acceptance of the MAGNEX spectrometer gives the possibility to explore an angular range $\theta_{opt} - 5° \leq \theta_{lab} \leq \theta_{opt} + 6°$ for a given central angle θ_{opt}. In the present data, this corresponds to an angular distribution which covers the range $5° \leq \theta_{lab} \leq 40°$, considering the five angular positions at which the apparatus was located. The spectrometer positions also allowed for angular overlaps of at least 3° between runs at contiguous central angles.
The differential cross section is calculated using the formula:

$$\frac{d\sigma}{d\Omega}(\theta) = \frac{N(\theta)}{N_{beam}\, N_{target}\, \Delta\Omega\, t_{live}\, \epsilon} \tag{5.8}$$

where $N(\theta)$ is the number of ejectiles detected at a given angle θ, N_{beam} is the number of incident ions, N_{target} is the number of scattering centers per unit surface, $\Delta\Omega$ is the solid angle covered by the detector, t_{live} is a factor which takes into account the acquisition dead time and ϵ is an overall efficiency factor.

The number of incident ions is retrieved integrating the beam current measured by the Faraday cup. A digital integrator (see Chapter 4) gives the total charge Q collected in each run. At the considered energy, the ^{16}O ions are totally stripped [90], therefore the number of beam ions is simply evaluated as $N_{beam} = Q/Ze$, where $Z = 8$ and $e = 1.602 \cdot 10^{-19}$C. Actually, a dedicated VME scaler measured directly the integrated charge Q_{live} corrected for the acquisition dead time, thus already including the factor t_{live} of eq. (5.8). The obtained values for each investigated angular setting are reported in table 5.2.

$\boldsymbol{\theta_{lab}^{opt}}$ (degrees)	$\boldsymbol{N_{beam}}$ (ions)
10°	$4.71 \cdot 10^{12}$
13°	$6.35 \cdot 10^{13}$
18°	$8.60 \cdot 10^{14}$
26°	$4.00 \cdot 10^{15}$
34°	$9.31 \cdot 10^{15}$

Table 5.2: Total number of impinging ions N_{beam} for each investigated angular setting.

The number of scattering centers per unit surface, N_{target}, is calculated using the program LISE++ [87]. A value of $N_{target} = 2.43 \cdot 10^{18}$ atoms/cm^2 is obtained for the 109 μg/cm^2 thick ^{27}Al target used in the experiment.

The evaluation of the solid angle $\Delta\Omega$ spanned by the detector is performed through a graphical cut in the $\theta_i - \phi_i$ plane following the real acceptance shape (green contour in Fig. 5.23). In fact, as already discussed in Section 5.4.1, the ideal rectangular shape, determined by the four solid angle diaphragms, is not achievable due to efficiency losses at the borders of the beam envelope through the spectrometer.

The circular slices drawn in the figure are traced considering, at each integration step, two circles centered at the origin $(\theta_i, \phi_i) = (0, 0)$ and having radii θ_i and $\theta_i + \Delta\theta_i$, respectively. $\Delta\theta_i$ is the chosen integration step. In this way, the area of the considered slice (full black area) gives the differential solid angle for each $\Delta\theta_i$ bin, with an estimated error of about 2%.

The overall efficiency factor ϵ is estimated taking into account the FPD detection efficiency ($\sim$ 95%) and the loss of events in the ray reconstruction procedure. The latter is obtained from the ratio between the number of the well reconstructed events and the number of the events identified by the FPD. A typical loss of about 25% was

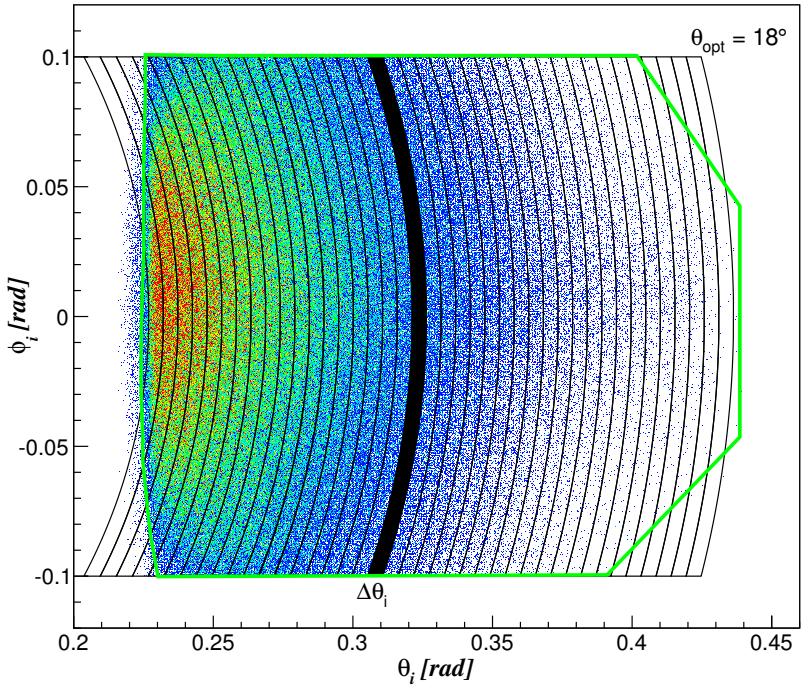

Figure 5.23: The solid angle evaluation procedure. The green contour is the graphical cut reproducing the real spectrometer acceptance. The area of each circular ring, enclosed in the green cut, gives the differential solid angle in the angular bin $\theta_i - \theta_i + \Delta\theta_i$ (full black area).

found for the investigated angular settings. Comparison with Rutherford scattering cross section demonstrated that the efficiency losses can be estimated within a few percent at the most [65].

The number of detected ions $N(\theta)$ is extracted from the $E_x - \theta_{lab}$ spectra, after a proper selection of the events of interest. In the following two Sections the result for the elastic and inelastic case are discussed.

5.6.1 Elastic angular distributions

The elastic angular distribution for the $^{16}O + ^{27}Al$ system can be constructed once the number of detected ions $N(\theta)$ corresponding to the elastic process is determined. The $N(\theta)$ value is extracted using a graphical cut selecting only the $^{27}Al_{g.s.}$ in the $E_x - \theta_{lab}$ plot. The achieved energy resolution makes it possible to separate the ground state

from the low lying excited states, i.e. the elastic from the inelastic processes. The procedure for the data set at $\theta_{lab}^{opt} = 18°$ is shown in Fig. 5.24.

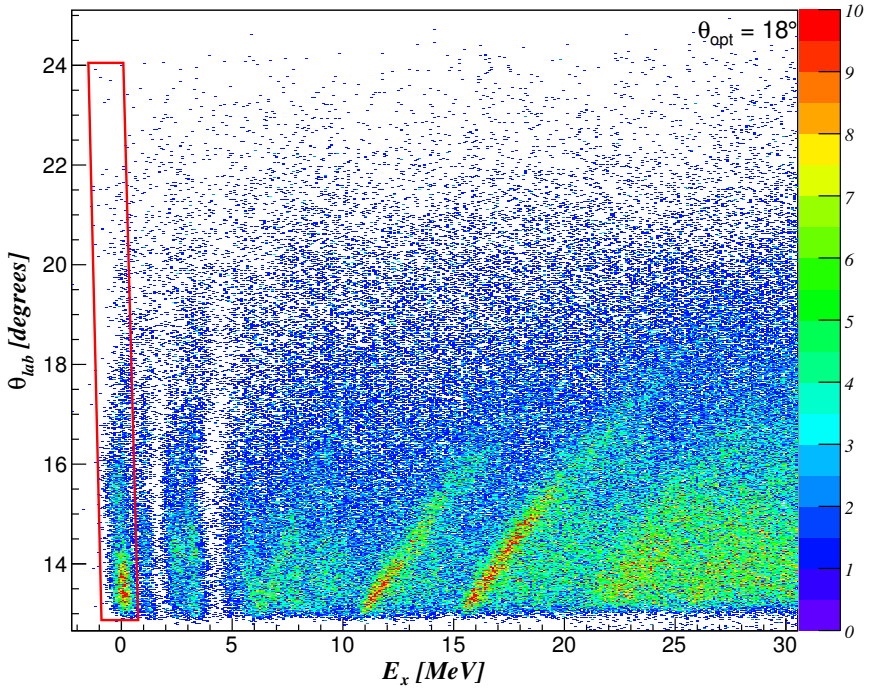

Figure 5.24: The graphical selection of the $^{27}Al_{g.s.}$ for the construction of the elastic cross section angular distribution.

Once the events are selected, they are projected on the θ_{lab} axis choosing fixed $\Delta\theta$ angular bins ($\Delta\theta = 0.2°$ for the data set of Fig. 5.24), thus obtaining $N(\theta)$ at each angular step. Then, using equation (5.8), the corresponding cross section values are calculated. Finally, the scattering angles in the laboratory reference frame are converted into the corresponding angles in the center of mass system using the Jacobian determinant of the transformation, given by CATKIN [88]. The obtained elastic angular distributions are reported in Figs. 5.25, 5.26, 5.27, 5.28, 5.29 for each investigated experimental setting. The total distribution, shown in Fig. 5.30, is a clear evidence of the quality of the data and of the accuracy of the absolute cross section measurements, since the single distributions perfectly overlap themselves without any need of re-normalization factors. A larger angular bin was chosen for the 26° and 34° distributions in order to achieve a good compromise between the statistical uncertainties in

the number of counts for each bin and the angular resolution.

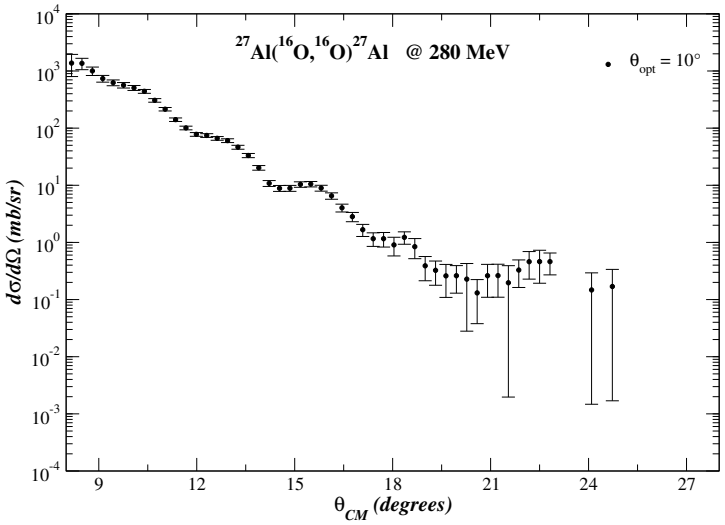

Figure 5.25: Elastic cross section angular distribution for the data set at $\theta_{lab}^{opt} = 10°$.

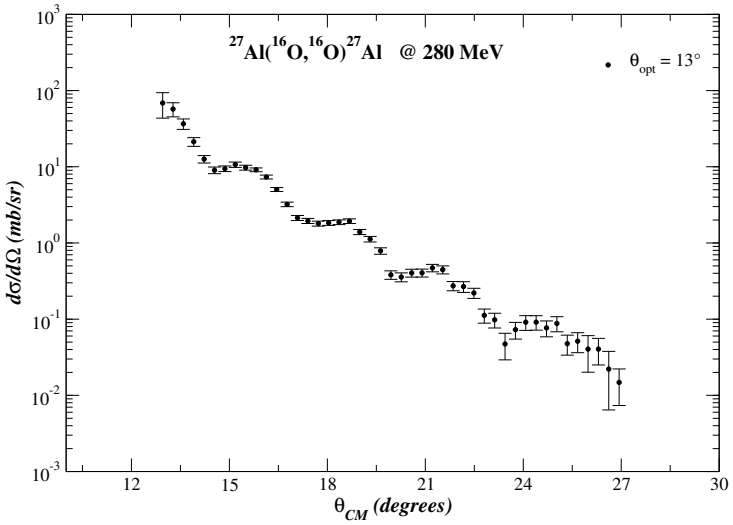

Figure 5.26: Elastic cross section angular distribution for the data set at $\theta_{lab}^{opt} = 13°$.

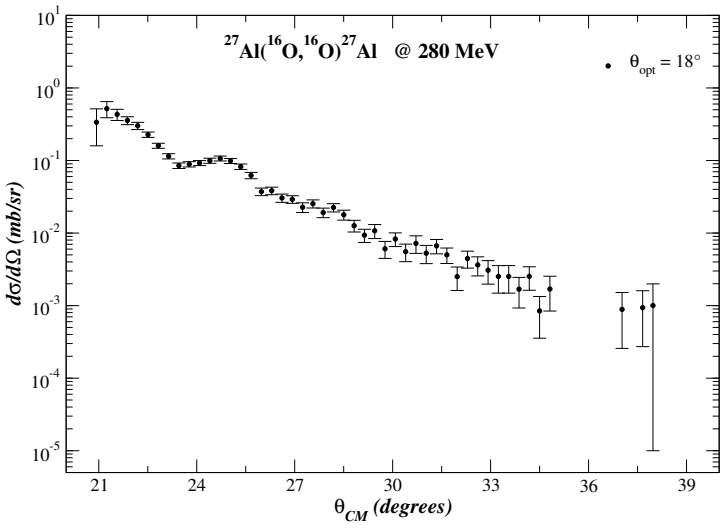

Figure 5.27: Elastic cross section angular distribution for the data set at $\theta_{lab}^{opt} = 18°$.

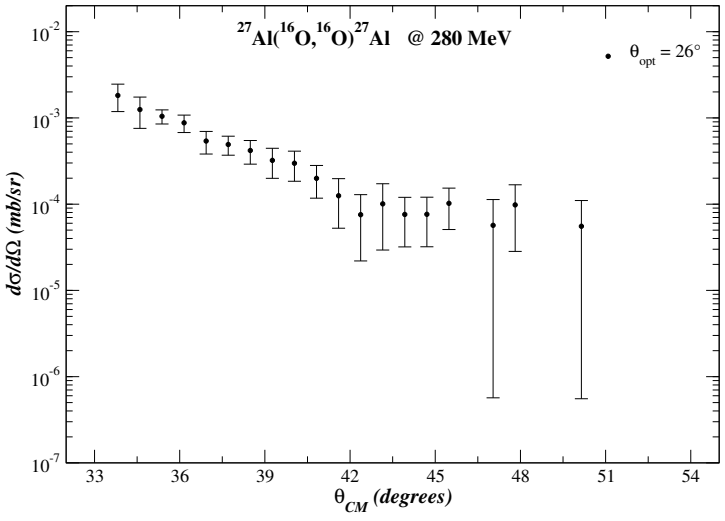

Figure 5.28: Elastic cross section angular distribution for the data set at $\theta_{lab}^{opt} = 26°$.

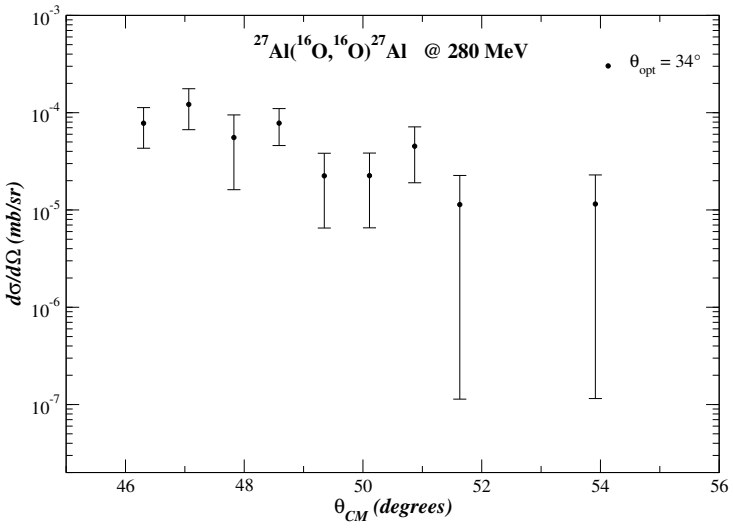

Figure 5.29: Elastic cross section angular distribution for the data set at $\theta_{lab}^{opt} = 34°$.

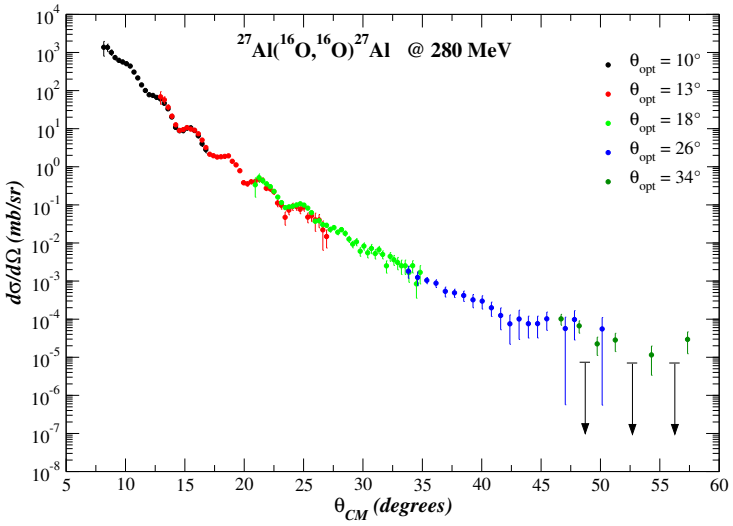

Figure 5.30: Total cross section angular distribution for the $^{16}\mathrm{O} + ^{27}\mathrm{Al}$ elastic scattering process at 280 MeV. The dashes at the tail of the arrows correspond to the estimated upper limits for the cross section.

5.6.2 Inelastic angular distributions

The inelastic cross section angular distributions are obtained following a procedure identical to that just described for the elastic process. In this case, $N(\theta)$ is extracted through a graphical cut which includes all the first low lying excited states, applied to the $E_x - \theta_{lab}$ plots: as it will be discussed in next chapter, all these states belong to same $L = 2$ multiplet $^{28}\mathrm{Si}(2^+) \otimes \nu(1d5/2)^{-1}$. An example is shown in Fig. 5.31 for the data set at $\theta_{lab}^{opt} = 18°$.

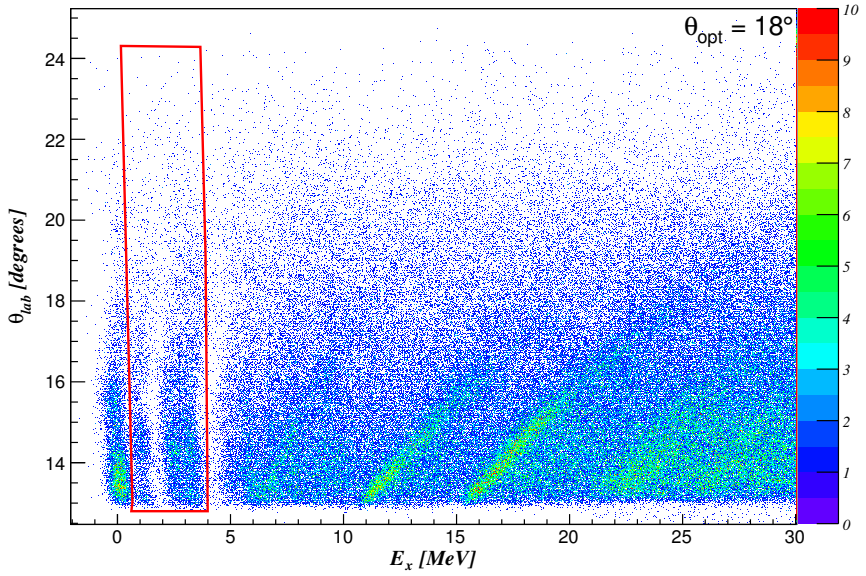

Figure 5.31: The graphical selection of the ^{27}Al low lying excited states for the construction of the inelastic cross section angular distribution.

The projection of the selected events on the θ_{lab} axis gives $N(\theta)$ for each angular bin $\Delta\theta$. Thus, through eq. (5.8), the inelastic angular distributions are constructed. The result for the total distribution in shown in Fig. 6.8. A perfect overlap between all the single distributions is observed, just as in the elastic case, again without the need of re-normalization factors. Also in this case a larger angular bin has been chosen for the 26° and 34° distributions for the best compromise between statistics and angular resolution.

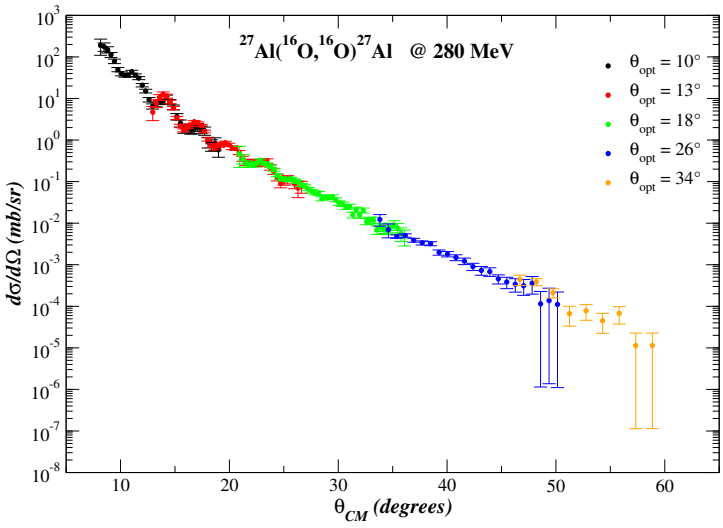

Figure 5.32: Total inelastic cross section angular distribution for ^{27}Al low lying excited states populated in the ^{16}O +^{27} Al reaction at 280 MeV.

5.6.3 Cross section uncertainties

The error bars in the cross sections are calculated through the error propagation applied to eq. (5.8). The uncertainties on the number of impinging ions N_{beam} (corrected for the acquisition dead time) and on the number of the scattering centers N_{target} contribute to an overall error of about 10% in the absolute scale of the cross sections, not included in the single data points plotted in the previous Figures. Thus, the main sources of error in the single datum point are the number of the detected ions, the solid error calculation and on the efficiency ϵ. The error on $N(\theta)$ is simply given by $\Delta N(\theta) = \sqrt{N(\theta)}$, evaluated for each angular bin $\Delta\theta_{lab}$ chosen in the cross section extraction procedure. The error on $\Delta\Omega$ depends on the uncertainties on the reconstructed vertical and horizontal angles ϕ_i and θ_i, respectively. The former is about $\Delta\phi_i = \pm\, 0.4°$ [65], and corresponds to a common factor for all the angular distribution bins. The latter is affected by an uncertainty of about $\Delta\theta_i = \pm 0.2°$ [65]. This error is important especially for those bins corresponding to the border of the acceptance, where the effect is larger. Its influence was evaluated calculating the variation of the area of the slices used to obtain the differential solid angle (Fig. 5.23) when θ_i was varied within $\pm\, 0.2°$. Finally,

$\Delta\epsilon$ was calculated considering that the reconstruction efficiency is slightly different depending on the angular bin considered (the biggest variations are found at the border of the acceptance). Thus, this effect was taken into account calculating ϵ from the ratio between the reconstructed events and the detected events at the FPD and for each angular bin selected.

Chapter 6

Data analysis

The present chapter is devoted to the analysis of the ^{16}O + ^{27}Al elastic scattering at E_{lab} = 280 MeV. In particular, the experimental elastic and inelastic angular distributions will be compared to theoretical calculations based on the Coupled Channel formalism. The São Paulo parameter-free double folding potential, already discussed in Chapter 2, is adopted in all the calculations.

6.1 Model independent analysis

Before going in the details of the data analysis, some preliminary considerations can be made about the experimental results. The primary goal of the experiment was the measurement of the elastic angular distribution for the ^{16}O + ^{27}Al system at 280 MeV down to hundreds of nb/sr. This ambitious result was achieved and the total cross section elastic angular distribution is shown in Fig. 6.1. The figure clearly shows how the elastic angular distribution deviates from the rapid exponential decrease expected for a strong absorbing system [15]. In order to emphasize this feature, qualitative exponential fit have been performed in three different angular ranges: $8^\circ \leq \theta_{cm} \leq 25^\circ$ (red dashed line), $20^\circ \leq \theta_{cm} \leq 50^\circ$ (blue dashed line) and $42^\circ \leq \theta_{cm} \leq 58^\circ$ (green dashed line). These curves are used just to guide the eyes. Starting from about $\theta_{cm} \approx 20^\circ$, the data systematically deviate with respect to the rapid exponential decrease represented by the red dashed curve. Another change in the slope of the distribution is located at $\theta_{cm} \approx 42^\circ$, where the cross section fall off is strongly attenuated. Moreover, a local minimum is observed at $\theta_{cm} \approx 36^\circ$, where a first broad oscillation occurs. All

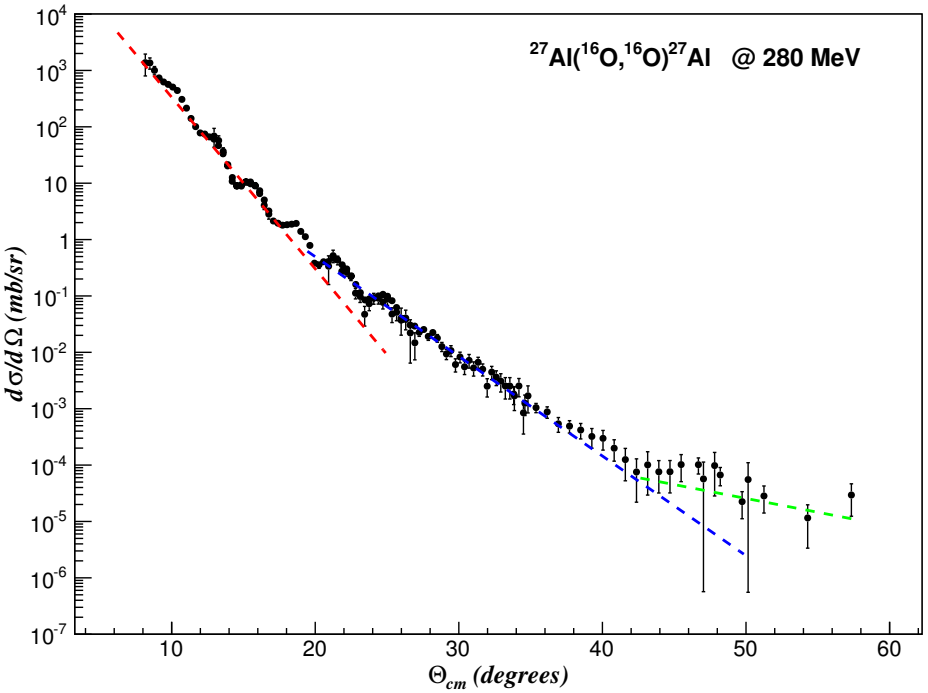

Figure 6.1: Total elastic angular distribution for the ^{16}O + ^{27}Al reaction at $E_{lab} = 280$ MeV. The dashed lines drawn in the figure are exponential fit of the data used just to guide the eyes. Three changes in the slope of the distribution are clearly visible, definitively deviating from the sharp exponential decrease at the smallest angles.

these characteristics well match with the rainbow features discussed in the previous chapters. Without the need of any theory, the experimental findings can be already considered as an interesting signal of a well developed rainbow structure in the ^{16}O + ^{27}Al system, consisting in the broad bump observed at the largest scattering angles. The 3-slope like pattern is here much more clear than found at 100 MeV (see Chapter 2), where only the initial part of the rainbow structure was at most observed. The quality of these results resembles more the best evidences of nuclear rainbow found in the ^{16}O + ^{16}O elastic scattering at 350 MeV (see Chapter 1).

6.2 CC calculations

The theoretical calculations were performed using the computer code FRESCO [21]. The code allows to find the solution of equation (3.18), repeated here for convenience:

$$[E - \epsilon_\alpha - K_\alpha - (\alpha|V_\alpha|\alpha)]\, u_\alpha(\mathbf{r}_\alpha) = \sum_{\alpha \neq \alpha'} \left(\alpha|V_\alpha|\alpha'\right) u_{\alpha'}(\mathbf{r}_\alpha) \tag{6.1}$$

The $u_\alpha(\mathbf{r}_\alpha)$ functions indicate that the exact total wave function $\Psi = \sum_\alpha \xi_\alpha(\mathbf{r}_\alpha)\psi_\alpha(x_\alpha)$ is replaced by the model one $\Psi_{model} = \sum_\alpha{}' u_\alpha(\mathbf{r}_\alpha)\psi_\alpha(x_\alpha)$ and an effective interaction V_α for the investigated α partition is used.
The interaction matrix elements are given by:

$$\left(\alpha|V_\alpha|\alpha'\right) \equiv \int \psi^*_\alpha(x_\alpha) V_\alpha(\mathbf{r}_\alpha, x_\alpha)\psi_{\alpha'}(x_\alpha) dx_\alpha = V_{\alpha\alpha'}(\mathbf{r}_\alpha) \tag{6.2}$$

In order to obtain the solution of (6.1), in the FRESCO input file the channels to couple, the strength of the corresponding coupling and the potential to be used must be specified. In the next two sections, these aspects are discussed in detail.

6.2.1 Channels wavefunctions and strength of the coupling

As shown in Section 5.5, the $^{27}\mathrm{Al}_{g.s.}$ and several low lying excited states are populated in the $^{16}\mathrm{O}$ + $^{27}\mathrm{Al}$ at 280 MeV incident energy. These states are therefore coupled to the $^{16}\mathrm{O}_{g.s.}$ in the CC calculations. When inserted in the FRESCO input file, the spin, parity and excitation energy of each state must be specified. The values used in the calculations are listed in table 5.1. The coupling between two given states α and α' depends on the interaction potential used to excite the system from the state α to the state α'. In the FRESCO code, this interaction is constructed within a given model. In the ^{27}Al case, a collective model was adopted, where the excitations are interpreted in terms of the deformation of the charge or mass distribution of the nucleus. This is a standard way to proceed for the low lying 2^+ state of an even-even nucleus, due to the relevant degree of collectivity of such state. Here this procedure is extended to the ^{27}Al odd nucleus, assuming that the $1/2^+$, $3/2^+$, $5/2^+$, $7/2^+$ and $9/2^+$ multiplet of states originates from the weak coupling of the ^{28}Si 2^+ collective state and the $5/2^+$ proton hole orbital. The ^{27}Al excited states are then described in terms of deformed potentials. The way in which the Coulomb and nuclear deformation are treated in

FRESCO is described in detail in Appendix A.
In order to calculate the strength of the coupling, the following reduced matrix element (see Appendix A) has to be evaluated:

$$\langle \alpha \parallel V^{\lambda} \parallel \alpha' \rangle \tag{6.3}$$

for the transition $\alpha \longrightarrow \alpha'$ through the operator V of multipolarity λ.
As an example, the excitation from the $^{27}\mathrm{Al}_{g.s.}$ to the $5/2^+$ state is described as follows:

$$\begin{aligned} |\alpha\rangle &= {}^{27}\mathrm{Al}_{g.s.} = |0^+ \otimes \frac{5}{2}^+, \frac{5}{2}^+\rangle \\ |\alpha'\rangle &= {}^{27}\mathrm{Al}_{5/2^+} = |2^+ \otimes \frac{5}{2}^+, \frac{5}{2}^+\rangle \end{aligned} \tag{6.4}$$

where $|0^+\rangle$ and $|2^+\rangle$ are the ^{28}Si ground and first excited states, respectively. Therefore, eq. (6.3) becomes:

$$\langle 0^+ \otimes \frac{5}{2}^+, \frac{5}{2}^+ \parallel V^{\lambda} \parallel 2^+ \otimes \frac{5}{2}^+, \frac{5}{2}^+ \rangle \tag{6.5}$$

The reduced matrix element is evaluated using the Wigner-Eckart theorem [91]:

$$\langle j' \| V^k \| j \rangle = \langle j' m' | V^k_q | j m \rangle \frac{\sqrt{2j'+1}}{(j' m' k q | j m)} \tag{6.6}$$

where $(j' m' k q | j m)$ are Clebsch-Gordan coefficients used to couple two states $|j_1 m_1\rangle$ and $|j_2 m_2\rangle$ to obtain the state $|JM\rangle$:

$$\begin{aligned} J &= j_1 \otimes j_2 \\ |JM\rangle &= \sum_{m_1, m_2} (j_1 m_1 j_2 m_2 | JM) |j_1 m_1\rangle |j_2 m_2\rangle \end{aligned} \tag{6.7}$$

The C-G coefficients are always zero unless:

$$\begin{aligned} M &= m_1 + m_2 \\ |j_1 - j_2| &\leq J \leq j_1 + j_2 \end{aligned} \tag{6.8}$$

For the $^{27}\mathrm{Al}_{g.s.} \longrightarrow {}^{27}\mathrm{Al}_{5/2^+}$ transition through the quadrupole operator V^2, $j' = j = \frac{5}{2}$, $k = 2$, $q = 0$ and, from the C-G properties (6.8), $m = m' = 5/2$. The reduced matrix

element (6.5) is therefore:

$$\langle\alpha\|V^2\|\alpha'\rangle = \frac{\sqrt{6}}{\left(\frac{5}{2}\frac{5}{2}20|\frac{5}{2}\frac{5}{2}\right)}\langle 0^+ \otimes \frac{5}{2}^+, \frac{5}{2}^+\frac{5}{2}\|V_0^2\|2^+ \otimes \frac{5}{2}^+, \frac{5}{2}^+\frac{5}{2}\rangle \tag{6.9}$$

where the C-G coefficient $\left(\frac{5}{2}\frac{5}{2}20|\frac{5}{2}\frac{5}{2}\right)$ is $\frac{\sqrt{5}}{\sqrt{14}}$.
The ground state and $5/2^+$ excited state wavefunctions are, respectively:

$$|0^+ \otimes \frac{5}{2}^+\rangle = \sum_{\mu_1}\left(00\frac{5}{2}\mu_1|\frac{5}{2}\frac{5}{2}\right)|00\rangle\,|\frac{5}{2}\frac{5}{2}\rangle \tag{6.10}$$

$$|2^+ \otimes \frac{5}{2}^+\rangle = \sum_{\mu_2\mu_3}\left(2\mu_2\frac{5}{2}\mu_3|\frac{5}{2}\frac{5}{2}\right)|2\mu_2\rangle\,|\frac{5}{2}\mu_3\rangle \tag{6.11}$$

Using these expressions, eq. (6.9) is written as:

$$\langle\alpha\|V^2\|\alpha'\rangle = \frac{\sqrt{6}\sqrt{14}}{\sqrt{5}}\sum_{\mu_1\mu_2\mu_3}\left(00\frac{5}{2}\mu_1|\frac{5}{2}\frac{5}{2}\right)\langle 00|V_0^2|2\mu_2\rangle\langle\frac{5}{2}\mu_1|\frac{5}{2}\mu_3\rangle\left(2\mu_2\frac{5}{2}\mu_3|\frac{5}{2}\frac{5}{2}\right) \tag{6.12}$$

Exploiting the orthonormality of the wavefunctions and the C-G properties, eq. (6.12) becomes:

$$\langle\alpha\|V^2\|\alpha'\rangle = \frac{\sqrt{6}\sqrt{14}}{\sqrt{5}}\left(00\frac{5}{2}\frac{5}{2}|\frac{5}{2}\frac{5}{2}\right)\langle 00|V_0^2|20\rangle\left(20\frac{5}{2}\frac{5}{2}|\frac{5}{2}\frac{5}{2}\right) \tag{6.13}$$

The C-G coefficients $\left(00\frac{5}{2}\frac{5}{2}|\frac{5}{2}\frac{5}{2}\right)$ and $\left(20\frac{5}{2}\frac{5}{2}|\frac{5}{2}\frac{5}{2}\right)$ in eq. (6.13) are equal to 1 and $\frac{\sqrt{5}}{\sqrt{14}}$, respectively. Thus:

$$\langle\alpha\|V^2\|\alpha'\rangle = \sqrt{6}\langle 00|V_0^2|20\rangle \tag{6.14}$$

The Wigner-Eckart theorem is then used again to evaluate the matrix element:

$$\langle 00|V_0^2|20\rangle = \frac{1}{\sqrt{5}}\langle 0\|V^2\|2\rangle \tag{6.15}$$

while the reduced matrix element $\langle 0\|V^2\|2\rangle$ is obtained from [92]:

$$B_\lambda(I',I) = \sqrt{2I+1}(Ik\lambda 0|I'k) \;\longrightarrow \langle 0\|V^2\|2\rangle = \sqrt{5}(2020|00) = \frac{\sqrt{5}}{\sqrt{5}} = 1 \tag{6.16}$$

The strength of the $^{27}\mathrm{Al}_{g.s.} \longrightarrow {}^{27}\mathrm{Al}_{5/2^+}$ transition is finally given by:

$$\langle \frac{5}{2}^{+}\, g.s. \| V^2 \| \frac{5}{2}^{+*} \rangle = \sqrt{\frac{6}{5}} = 1.095 \tag{6.17}$$

This is the value inserted in the FRESCO input file in order to specify the real strength of the coupling between the considered states. The same procedure has been followed for the remaining states. The obtained strengths are listed in table 6.1.

α	α'	$\langle \alpha \parallel V^2 \parallel \alpha' \rangle$
$^{27}\mathrm{Al}_{g.s.}$	$^{27}\mathrm{Al}_{1/2^+}$	0.632
$^{27}\mathrm{Al}_{g.s.}$	$^{27}\mathrm{Al}_{3/2^+}$	0.894
$^{27}\mathrm{Al}_{g.s.}$	$^{27}\mathrm{Al}_{5/2^+}$	1.095
$^{27}\mathrm{Al}_{g.s.}$	$^{27}\mathrm{Al}_{7/2^+}$	1.266
$^{27}\mathrm{Al}_{g.s.}$	$^{27}\mathrm{Al}_{9/2^+}$	1.422
$^{27}\mathrm{Al}_{1/2^+}$	$^{27}\mathrm{Al}_{1/2^+}$	0.0
$^{27}\mathrm{Al}_{3/2^+}$	$^{27}\mathrm{Al}_{3/2^+}$	0.645
$^{27}\mathrm{Al}_{5/2^+}$	$^{27}\mathrm{Al}_{5/2^+}$	0.430
$^{27}\mathrm{Al}_{7/2^+}$	$^{27}\mathrm{Al}_{7/2^+}$	-0.203
$^{27}\mathrm{Al}_{9/2^+}$	$^{27}\mathrm{Al}_{9/2^+}$	-1.219

Table 6.1: Coupling strengths between the states indicated as α and α' used in the FRESCO CC calculations.

6.2.2 The interaction potential

The São Paulo potential (see Section 3.1 for its detailed description) was used in the FRESCO code as the current interaction potential. The complete form (3.10) of the potential is given here for convenience:

$$V_{SPP}(R,E) = V_F(R) e^{-4\left(\frac{v(R)}{c}\right)^2} (n_r + i\, n_i) = V_{LE}(R,E)(n_r + i\, n_i) \tag{6.18}$$

The double folding potential $V_F(R)$ (2.20) is calculated as [15]:

$$V_F(R) = \int \rho_1(r_1)\rho_2(r_2) V_0 \delta(\mathbf{R} - \mathbf{r}_1 + \mathbf{r}_2)\, d\mathbf{r}_1\, d\mathbf{r}_2 \tag{6.19}$$

with $V_0 = -456$ MeV fm^3.

The use of the matter densities and delta function in eq. (6.19) corresponds to the *zero-range* approach for the folding potential, which is equivalent [16] to the more

usual procedure of using the frozen M3Y effective nucleon-nucleon interaction with the nucleon densities of the nuclei. The nuclear densities are modelled by the two-parameter Fermi distribution (2pF) fitted on experimental data [16] or, when missing, on Dirac-Hartree-Bogoliubov (DHB) calculations [50]. The values used to generate the São Paulo potential are listed in table 6.2 and the corresponding result is shown in Fig. 6.2.

Parameter	Description	Value
R_m^P	^{16}O matter radius	2.461 fm
R_c^P	^{16}O charge radius	2.560 fm
a_m^P	^{16}O matter diffuseness	0.560 fm
a_c^P	^{16}O charge diffuseness	0.530 fm
R_m^T	^{27}Al matter radius	3.090 fm
R_c^T	^{27}Al charge radius	3.178 fm
a_m^T	^{27}Al matter diffuseness	0.560 fm
a_c^T	^{27}Al charge diffuseness	0.530 fm
R_{max}	Matching radius ($V = 0$ for $R > R_{max}$)	30 fm
L_{max}	Number of partial waves	300

Table 6.2: Parameters used to generate the São Paulo potential used in the CC calculations.

In the CC calculations (see Appendix A) the ^{27}Al excitations are treated in terms of deformations. Both the Coulomb contribution and the real part of the São Paulo potential have been deformed. The deformation length used was obtained by the product of the ^{28}Si deformation parameter ($\beta = 0.407$ [93]) and the ^{27}Al radius (3.75 fm [94]). Moreover, the real part of the potential was not scaled ($n_r = 1$), while the scaling factor $n_i = 0.6$ was adopted for the imaginary one.

6.3 Cross section angular distributions

6.3.1 Elastic angular distributions

A first comparison between the normalized experimental data ad the CC/SPP calculation of the elastic angular distribution is shown in Fig. 6.3. The theoretical distribution was calculated including in the input file the ^{27}Al ground state and the first five excited states using the couplings specified in table 6.1. This first comparison clearly shows how

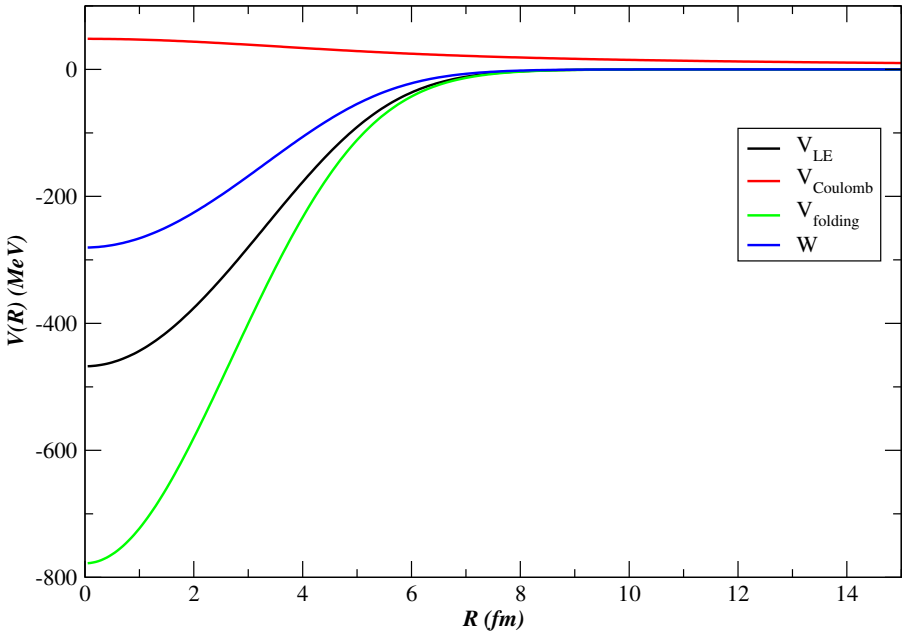

Figure 6.2: The São Paulo potential for the ^{16}O + ^{27}Al reaction at E_{lab} = 280 MeV. The different components of the potential are indicated in the legend. The Coulomb contribution (red curve) is also shown.

the theoretical distribution overestimates the cross section values in all the investigated angular range. Nevertheless, the oscillation pattern in the Fraunhofer diffraction region is well reproduced, with the phases of the oscillations in a very good agreement with the experimental ones. However, besides the too large cross section values, no rainbow structure is predicted with this approach, i.e. effectively including the ^{27}Al states.
Even if this first theoretical comparison gives a not so satisfactory result, the effect of the configuration mixing can be investigated, since an excited state with the same spin (5/2) and parity (+) as those of the ^{27}Al ground state is included in the calculation. In order to estimate this contribution, it is necessary to consider a modified version of

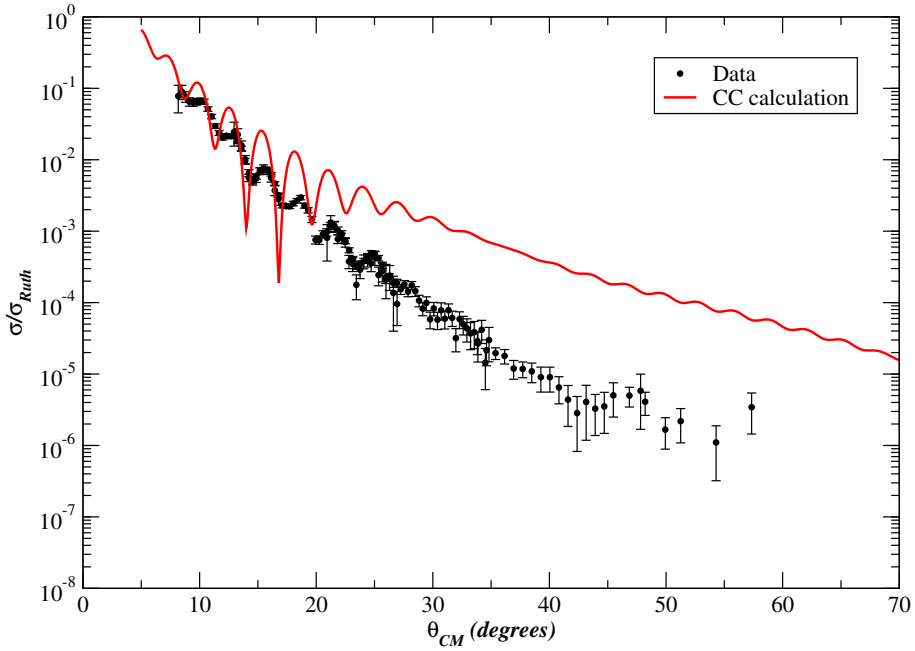

Figure 6.3: Comparison between the experimental elastic angular distribution and the CC/SPP theoretical result. The data are scaled for the corresponding Rutherford cross section values.

the wavefunctions for the g.s. and the considered excited state:

$$|\,\alpha\rangle = {}^{27}\mathrm{Al}_{g.s.} = a\,|0^+ \otimes \frac{5^+}{2}, \frac{5^+}{2}\rangle + \sqrt{1-a^2}\,|2^+ \otimes \frac{5^+}{2}, \frac{5^+}{2}\rangle \tag{6.20}$$

$$|\alpha'\rangle = {}^{27}\mathrm{Al}_{5/2*} = a\,|2^+ \otimes \frac{5^+}{2}, \frac{5^+}{2}\rangle - \sqrt{1-a^2}\,|0^+ \otimes \frac{5^+}{2}, \frac{5^+}{2}\rangle \tag{6.21}$$

where a is the mixing coefficient. Therefore, the following reduced matrix element has to be evaluated:

$$\begin{aligned}\langle\alpha\|V^2\|\alpha'\rangle =& (2a^2-1)\langle 0^+ \otimes \frac{5^+}{2}, \frac{5^+}{2}\|V^2\|2^+ \otimes \frac{5^+}{2}, \frac{5^+}{2}\rangle - \\ & a\sqrt{1-a^2}\langle 0^+ \otimes \frac{5^+}{2}, \frac{5^+}{2}\|V^2\|0^+ \otimes \frac{5^+}{2}, \frac{5^+}{2}\rangle + \\ & a\sqrt{1-a^2}\langle 2^+ \otimes \frac{5^+}{2}, \frac{5^+}{2}\|V^2\|2^+ \otimes \frac{5^+}{2}, \frac{5^+}{2}\rangle\end{aligned} \tag{6.22}$$

The final result is:

$$\langle \alpha \| V^2 \| \alpha \rangle = 2.19a\sqrt{1-a^2} + 0.43(1-a^2) \tag{6.23}$$

$$\langle \alpha \| V^2 \| \alpha' \rangle = 1.095(2a^2-1) + 0.43a\sqrt{1-a^2} \tag{6.24}$$

$$\langle \alpha' \| V^2 \| \alpha' \rangle = 0.43a^2 - 2.19a\sqrt{1-a^2} \tag{6.25}$$

A reasonable value of a is $a = 0.85$ [22], which means that the $^{27}Al_{5/2^+}$ g. s. wave-function has a contribution of the 15% arising from the $5/2^+$ excited state. The result of the calculation including the effect of the configuration mixing is shown in Fig. 6.4. The inclusion of the configuration mixing affects the theoretical calculation especially

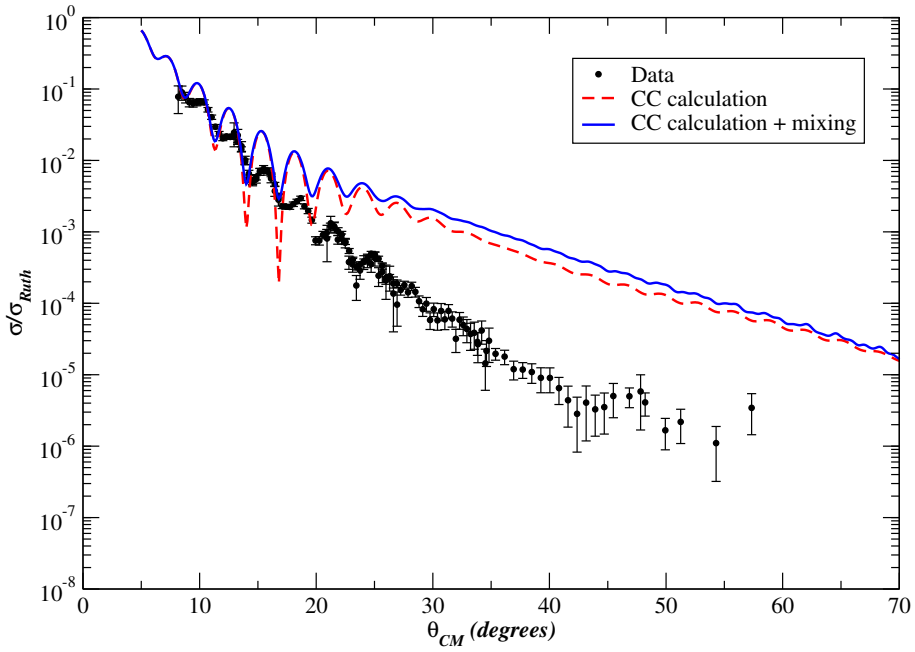

Figure 6.4: Comparison between the experimental elastic angular distribution and the CC/SPP theoretical results. The red distribution is the one shown in Fig. 6.3. The blue distribution is obtained when a mixing equal to 15% is included in the calculation (see text).

in the Fraunhofer angular region, with an improvement in the shape of the oscillation pattern. Indeed, the mixing between the ^{27}Al ground state and $5/2^+$ excited state

results in oscillations less deep when compared to the pure state result. The phase of the pattern is not affected by the introduction of the mixing.

The reason why the theoretical calculations performed including the effective ^{27}Al states do not reproduce the experimental data is to be searched in the symmetric rotational model implemented in FRESCO to calculate the couplings between the states of a deformed nucleus. This model works properly for even-even nuclei, like ^{28}Si, but there is no evidence that the ^{27}Al nucleus can be correctly treated within such a model. Nevertheless, as already discussed, the excitations of the ^{27}Al target can be treated in the weak coupling approach [22]. In ref. [22], in fact, the authors prove, analysing *(p,p')* cross section measurements, how the ^{27}Al states can be described as a $d5/2$ hole in the $T = 0$ nucleus ^{28}Si rather than a $d5/2$ particle added to the $T = 1$ nucleus ^{26}Mg. This approach was already used in the elastic scattering process ^{16}O + ^{27}Al at 100 MeV, as discussed in Chapter 2, and very good results were obtained when comparing the elastic angular distribution with the CC/SPP calculations. The weak coupling model was then adopted for the description of the ^{27}Al(^{16}O,^{16} O)^{27}Al scattering at 280 MeV. Within such a model, the ^{27}Al ground state and the first low lying excited states ($1/2^+$, $3/2^+$, $5/2^+$, $7/2^+$, $9/2^+$) are described as a $1d5/2$ proton hole coupled with the ^{28}Si 0^+ ground state and 2^+ (1.779 MeV) excited state, respectively. Therefore, in the calculations the $^{16}O_{g.s.}(0^+) \longrightarrow {}^{27}Al_{g.s.}(5/2^+)$ channel is replaced by the $^{16}O_{g.s.}(0^+) \longrightarrow {}^{28}Si_{g.s.}(0^+)$ one, while the first five low lying ^{27}Al excited states are globally described through the the excitation of the 2^+ ^{28}Si state, i.e. via the $^{16}O_{g.s.}(0^+) \longrightarrow {}^{28}$Si (2^+) channel. In this case there is no need to repeat the procedure for the calculation of the strength of the coupling between the states, as done for the ^{27}Al states, since FRESCO calculates this quantity in the framework of the standard symmetric rotational model. The obtained theoretical elastic angular distribution, compared to the experimental one, is shown in Fig. 6.5. As it can be appreciated in the figure, the calculation predicts much larger cross sections than the experimental results around 25° and above, by roughly one order of magnitude. Again, the best agreement with the data is obtained at the smallest angles, corresponding to the Fraunhofer diffraction region, since the phase of the oscillations are well reproduced. Unlike the result shown in Fig. 6.3, the present CC/SPP calculation shows a pronounced rainbow shoulder at about $\theta_{CM} \approx 47°$, which corresponds to the marked change in the slope of the experimental elastic distribution.

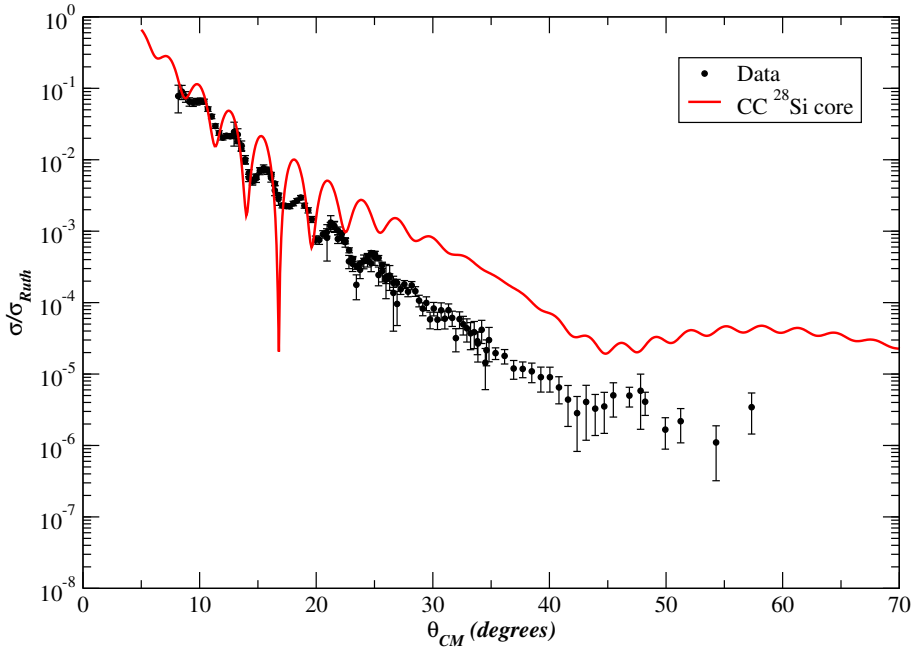

Figure 6.5: Comparison between the measured elastic angular distribution (black dots) and the CC/SPP calculation (red line) performed considering the ^{27}Al g.s. as a $1d5/2$ proton hole coupled with the ^{28}Si 0^+ ground state.

Additional coupling channels, not included in these calculations, are expected to become important at this beam energy, like excitation to other target and beam states and particle transfers. In principle, these channels will tend to reduce the flux to the elastic channel. Moreover, the model for the imaginary potential has not been previously tested in this energy and angular range, and it could be possible that a larger absorption is present than anticipated. Improved model calculations are being attempted in order to reduce the discrepancy in relation to the experimental observations. Such calculations are complex because a careful test of numerical convergence is necessary, and reliable results have not been obtained so far.

Actually, attempts were done in order to obtain a better agreement with the data. The São Paulo potential (6.18) used in the CC calculations was calculated considering an unscaled real part ($n_r = 1$) plus a scaled imaginary part ($n_i = 0.6$). These parameters

are standardly used in describing scattering and reaction data at several energies and for a large number of systems. However, in ref. [94], a reduced real potential was proven to give a better description of the data when a positive polarization from the continuum to bound states is particularly relevant, like in reactions where the projectile break-up is important. Even if this is not the case for the ^{16}O + ^{27}Al elastic scattering, the excitation of Giant Resonances modes observed at forward angles (see Section 6.4) can give rise to a similar contribution. The too large theoretical cross sections of Fig. 6.5 can be explained in terms of a too large real component of the nucleus-nucleus potential. Indeed, a strong attractive potential ($V_{LE}(R) \approx -470$ MeV at $R = 0$, see Fig. 6.2) results in an enhanced flux in the elastic channel and in a increased elastic cross section at backward angles. Thus, calculations considering a scaled real contribution of the optical potential were performed. Scaling factors equal to $n_r = 0.8$ and $n_r = 0.6$ were used. The scaling factor for the imaginary part was not modified ($n_i = 0.6$). The obtained results are reported in Fig. 6.6. The effect of the reduction of the strong attractive real component of the São Paulo potential is evident. Indeed, the theoretical cross sections become closer to the experimental ones when reducing the strength of the real part, as expected since less flux is scattered at backward angles due to the weaker attraction. At the same time, the rainbow shoulder at $\theta_{CM} \approx 47°$, well developed in the standard calculation ($n_r = 1.0$, $n_i = 0.6$), becomes progressively more damped. The effect of a reduced real part is also seen in the Fraunhofer diffraction region (see the inset in the figure). The cross section oscillations, in fact, result slightly wider and shifted toward larger angles as a consequence of the reduction the real potential.
The effect of the inclusion of other ^{28}Si excited states was also investigated in a very preliminary way. The 4^+ (4.617 MeV) and 0^+ (4.979 MeV) states were in particular included in the calculations. The obtained result is shown in Fig. 6.7. The real part of the São Paulo potential was reduced ($n_r = 0.8$) to obtain the best agreement with the data, while the imaginary one remained unchanged. This preliminary comparison shows how the inclusion of more channels in the calculation affects the elastic angular distribution in a significant way. The data are well reproduced in a wide angular range, with a good agreement for $\theta_{CM} < 40°$. On the other hand, the broad bump structure around $\theta_{CM} \approx 40°$ is slightly anticipated with respect to the standard distribution (red curve) and the experimental data. However, as already said, these calculations are still

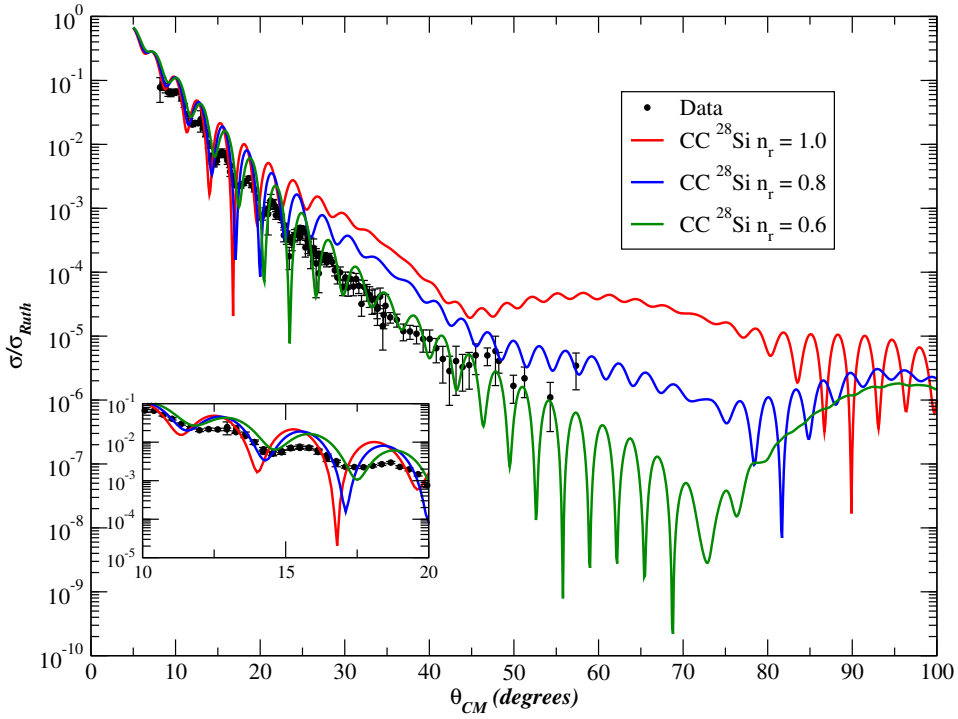

Figure 6.6: Comparison between the measured elastic angular distribution (black dots) and the CC/SPP results. The theoretical curves have been obtained considering the scaling factors for the real part as indicated in the figure. The inset shows the difference in the oscillation pattern between the calculations in the Fraunhofer diffraction region.

at a beginning stage and very accurate check of the models implemented and of the potential used are mandatory in this energy range.

6.3.2 Inelastic angular distributions

The FRESCO code calculates the inelastic cross sections corresponding to the excitation of each state specified in the input file. In the framework of the weak coupling model, the low lying excited states of the ^{27}Al target ($1/2^+$, $3/2^+$, $5/2^+$, $7/2^+$, $9/2^+$) are described as a $1d5/2$ proton hole coupled with the 2^+ first excited state of the ^{28}Si core. Like the elastic case, the strengths of the coupling are evaluated using the standard rotational model implemented in the code when the weak coupling approach is used. The result of the comparison between the experimental inelastic angular distribution

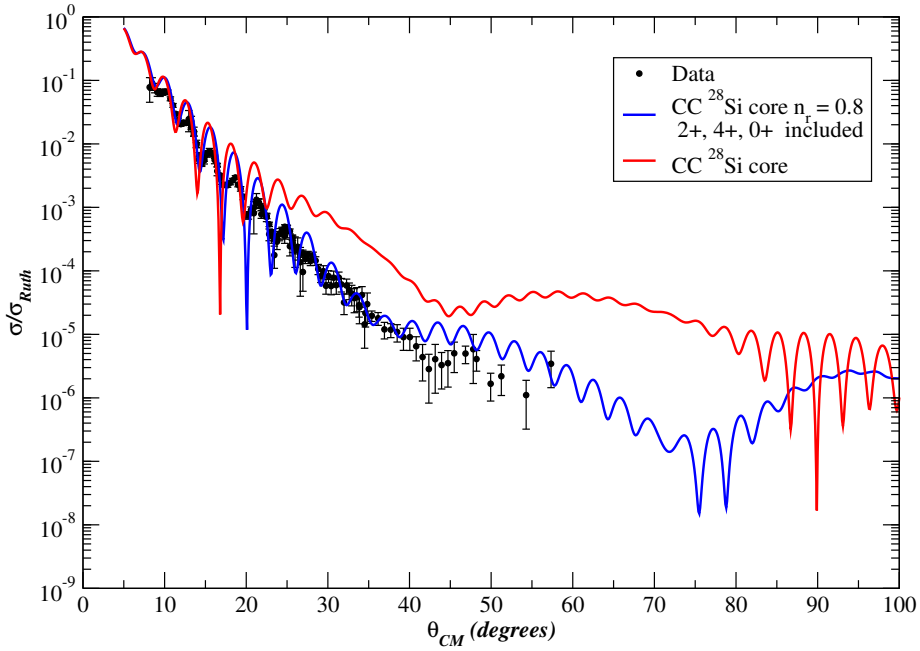

Figure 6.7: Comparison between the measured elastic angular distribution (black dots) and the CC/SPP results. The theoretical red distribution is the calculation of Fig. 6.5. The blue distribution is the result when the 4^+ (4.617 MeV) and 0^+ (4.979 MeV) ^{28}Si excited states are included in the calculation. A scaling factor $n_r = 0.8$ has been used.

and the theoretical calculation is shown in Fig. 6.8. The theoretical distribution gives inelastic cross sections larger than the experimental ones starting from about $\theta_{CM} \approx 15°$. The oscillation pattern at the smallest angles is well reproduced, with very similar phases, even if the deep minima predicted by the calculation are not experimentally observed. Moreover, the angular extension of the oscillation pattern is almost the same for both distributions, since no more oscillation are observed above $\theta_{CM} \approx 25°$.

As for the elastic case, also for the inelastic angular distribution the effect of the reduction of the real component of the São Paulo potential can be investigated. Scaling factor equal to $n_r = 0.8$ and $n_r = 0.6$ were again used, and the result of the comparison is shown in Fig. 6.9. The reduction of the strength of the real potential (the imaginary part being unchanged) results in a better agreement with the data. In particular,

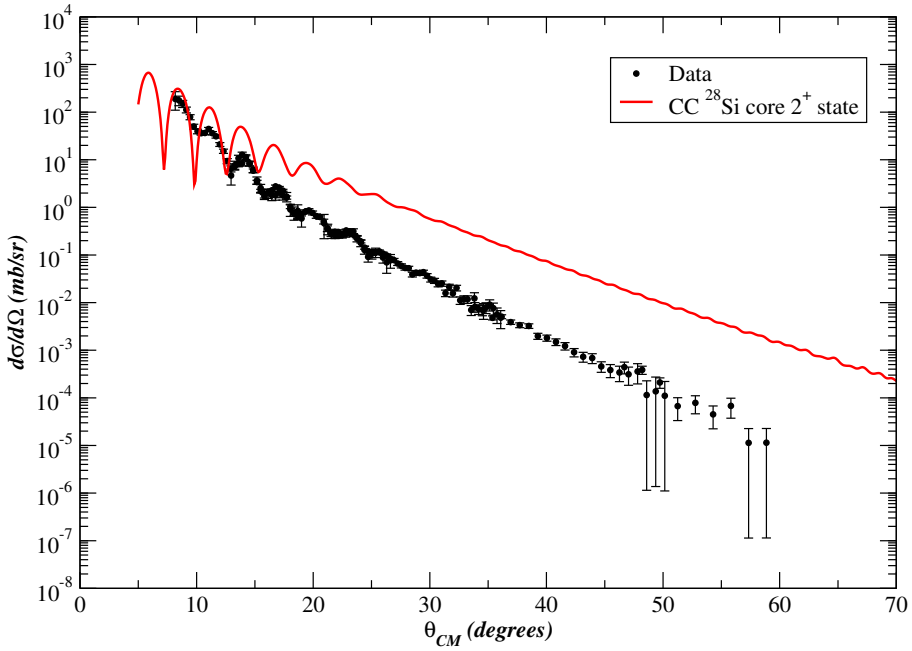

Figure 6.8: Comparison between the measured inelastic angular distribution (black dots) and the CC/SPP results. The theoretical red distribution is obtained when the low lying excited states of the ^{27}Al target are described as a $1d5/2$ proton hole coupled with the 2^+ first excited state of the ^{28}Si core.

the theoretical calculation for $n_r = 0.6$ gives a very good description of the trend of the experimental distribution. Besides the big effect at the largest angles, with a difference of almost two orders of magnitude between the red ($n_r = 1.0$) and the magenta ($n_r = 0.6$) distributions, a small shift of the oscillation pattern toward larger angles is observed with decreasing n_r (see the inset in the figure). The same effect was also observed for the elastic case (see Fig. 6.6). However, beyond these preliminary results, a very accurate check of the calculations is still in progress, thus no definitive conclusions can be given at this stage of the data analysis.

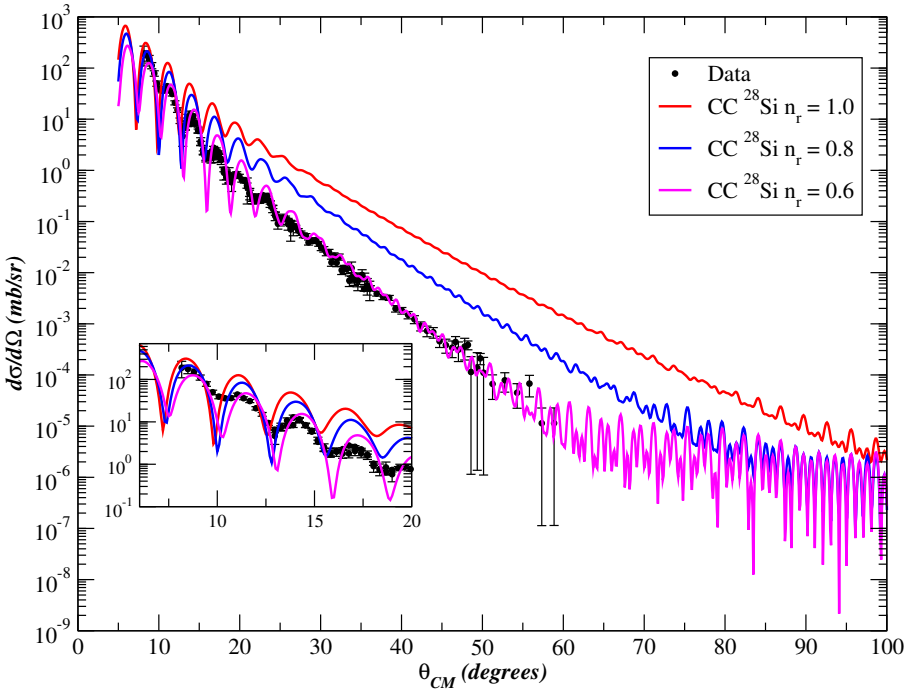

Figure 6.9: Comparison between the measured inelastic angular distribution (black dots) and the CC/SPP results. The theoretical curves have been obtained considering the scaling factors for the real part as indicated in the figure. The inset shows the difference in the oscillation pattern between the calculations at the smallest angles.

6.4 Giant Resonance modes

As anticipated in Section 5.5, the ^{27}Al excitation energy spectrum measured at $\theta_{lab}^{opt} = 10°$ is of particular interest since a huge bump followed by broader structures is observed at the smallest scattering angles. These structures are completely suppressed in a 4° degrees angular range, as shown in Fig. 6.10. These bumps can be associated to the excitation of collective modes in the target nucleus, i. e. Giant Resonance modes. Indeed, similar structures were already observed in the past in the ^{24,25,26}Mg and ^{27}Al inelastic α scattering [20].

Giant resonances are considered as highly collective nuclear excitations in which an appreciable fraction of the nucleons of a nucleus move together. These modes can be interpreted in hydrodynamical terms as the oscillation of a liquid drop. The most in-

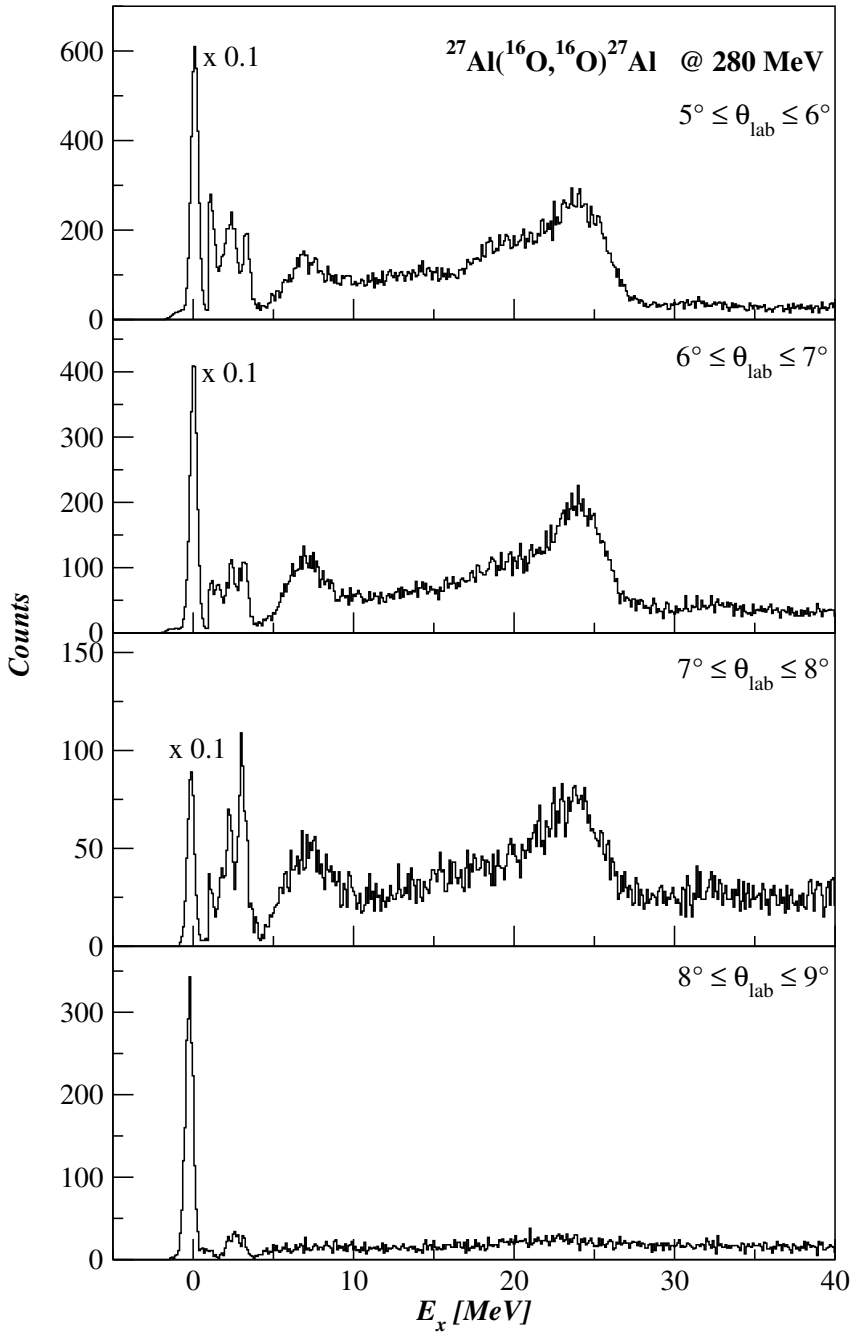

Figure 6.10: The evolution of the Giant Resonance modes observed in the ^{27}Al excitation energy spectrum measured at $\theta_{lab}^{opt} = 10°$. The huge bump at $E_x \approx 24$ MeV is completely suppressed for $\theta_{lab} > 8°$.

vestigated resonances are the Giant Monopole Resonance (GMR), the Giant Dipole Resonance (GDR) and the Giant Quadrupole Resonance (GQR). In the past decades several models were proposed in order to explain the observation of these nuclear excitations. For example, in the Goldhaber and Teller model [95], the GDR is interpreted as the excitation of a collective nuclear vibration in which all the protons in the nucleus move collectively against all the neutrons providing a separation between the centers of mass and charge, thus creating a dipole moment. The energy of the GDR can be fairly reproduced by the simple law $E_{GDR} \approx 80A^{-1/3}$ MeV. The GQR is interpreted as a surface vibration of the nucleus, which resembles the wave at the interface of two liquids. As for the GDR, the energy of the resonance depends on the mass number of the nucleus, since $E_{GQR} \approx 65A^{-1/3}$ MeV. Finally, the GMR is the $L = 0$ mode and is the only nuclear volume oscillation which has been isolated. The frequency of this breathing mode is directly related to the compressibility of the nucleus and the determination of its energy is the most direct way to access to the incompressibility modulus of nuclear matter. The energy of the resonance is roughly given by $E_{GMR} \approx 80A^{-1/3}$. Due to the large widths of these resonances (several MeV), the GMR is not always separated from the isoscalar component of the quadrupole resonance. On the other hand, the isoscalar dipole mode is a spurious center of mass motion and is not present as an internal excitation of stable atomic nuclei. In the (^{16}O, ^{16}O) scattering only the $T = 0$ isoscalar mode are allowed, due to the $T = 0$ value of the $^{16}O_{g.s.}$ wave function. As a consequence, no GDR is expected to be excited.

The pronounced structures observed in Fig. 6.10 above $E_x > 15$ MeV appear in an energy region which is compatible with the excitation of these giant modes. In fact, from the above formulas, the GMR is expected to appear at $E_x \approx 26.7$ MeV, while the GQR should be located at $E_x \approx 21.2$ MeV, considering the mass of the ^{27}Al target. The authors of ref. [20] found a somewhat similar result, with less evident structures. Also in this case, the bumps, associated with the excitation of the isoscalar GQR, were rapidly suppressed in less than 3° in the lab frame [20].

Considering the energy of the observed bumps and the results of ref. [20], the dominant collective mode excited in the investigated reaction can be ascribed to the excitation of the isoscalar GMR and GQR. These collective states should be included in the FRESCO input file in order to see their effect on the overall elastic and inelastic distributions. The corresponding calculations are time consuming, and an accurate check

in determining the strength of the coupling is necessary. In principle, the latter should be determined following the Energy Weighted Sum Rule (EWSR) [96], considering the GQR as its main contribution (in ref. [96] it is shown how the contribution of the low lying states in the excitation energy spectrum accounts for about the 10% of EWSR). Other hypotheses can be also considered, like the description of the Giant Resonances in terms of a constant imaginary potential. Anyhow, due to the complexity of the problem and to the different factors to take into account, the calculation is still in progress and no definitive result is available at this moment.

Chapter 7

Conclusions

In the present work the ^{16}O + ^{27}Al elastic scattering at 280 MeV incident energy was investigated. This study is inserted in the research line aiming at the investigation of the nuclear rainbow in the scattering process involving heavy nuclei. Nuclear rainbow is a peculiar phenomenon which reveals the nuclear interaction at small distances, where the projectile and target density overlaps can reach values up to twice the nuclear matter saturation value. The rainbow features were thought to be very unlikely for systems heavier than ^{16}O + ^{16}O because of the strong absorption, always present in heavy-ion collisions, which tends to hide the refractive component of the scattering process, responsible for the rainbow phenomenon.

The experiment was performed at the Catania LNS-INFN laboratory using a 280 MeV energy ^{16}O Cyclotron beam impinging on a 109 μg/cm^2 thick ^{27}Al target. The ejectiles were momentum analysed by the MAGNEX large acceptance magnetic spectrometer and detected by its Focal Plane Detector. In order to obtain wide elastic and inelastic angular distributions, five different angular settings were chosen, with the spectrometer optical axis located at 10°, 13°, 18°, 26° and 34° with respect to the beam direction. Due to the large angular acceptance of MAGNEX (-0.090 rad, +0.110 rad horizontally, $\pm$0.125 rad vertically in the spectrometer reference frame), these settings cover a whole angular range of about $5° \leq \theta_{lab} \leq 40°$ in the laboratory reference frame. The magnetic fields were set in order to focus the ^{16}O ejectiles corresponding to the ground state of the ^{27}Al residual nucleus at the focal plane position. Applying the ray-reconstruction procedure to the experimental data, ^{27}Al excitation energy spectra up to 85 MeV were extracted, showing the population of the ground state and low-lying excited states of

the residual nucleus. In addition, the spectra extracted at forward angles showed the population of large structures in a narrow angular range at relatively-high excitation energy, corresponding to the excitation of collective modes of the target nucleus, i.e. Monopole and Quadrupole Giant Resonances. Finally, elastic and inelastic cross section angular distributions were constructed for each angular setting.

A model independent data analysis was performed. The total elastic ^{16}O + ^{27}Al angular distribution was fitted using exponential functions in three different angular ranges. This procedure made it possible to better appreciate the systematic deviation of the data with respect to the rapid exponential decrease expected for a strong absorptive system. The rise of the cross section observed at the largest scattering angles is the evidence of a well developed nuclear rainbow structure for the investigated system. This result confirms the findings of the ^{16}O + ^{27}Al elastic scattering at 100 MeV, where only the initial part of the rainbow structure was at most observed. The experimental elastic and inelastic angular distributions were compared with a new generation of parameter-free calculations based on the Coupled Channel (CC) formalism, using the São Paulo potential (SPP). The calculations were performed with the computer code FRESCO. In a first step, the effective ^{27}Al states were included in the code, and the strengths of the coupling were specified. The comparison with the data revealed a well reproduced Fraunhofer oscillation pattern at the smallest scattering angles, but the calculations failed at the largest angles, systematically overestimating the experimental data. The introduction of the configuration mixing, due to the $5/2^+$ ^{27}Al excited state, improved the agreement at the smallest angles, damping the Fraunhofer oscillations, but had practically no effect at large angles. Moreover, no rainbow structure was predicted by these calculations. The problem was then treated in the framework of the weak coupling model. In this model the ^{27}Al ground state and the first low lying excited states ($1/2^+$, $3/2^+$, $5/2^+$, $7/2^+$, $9/2^+$) were described as a $1d5/2$ proton hole coupled with the ^{28}Si 0^+ ground state and 2^+ (1.779 MeV) excited state, respectively. Therefore, in the calculations the $^{16}O_{g.s.}(0^+) \longrightarrow {}^{27}Al_{g.s.}(5/2^+)$ channel was replaced by the $^{16}O_{g.s.}(0^+) \longrightarrow {}^{28}Si_{g.s.}(0^+)$ one, while the first five low lying ^{27}Al excited states were globally described through the excitation of the 2^+ ^{28}Si state, i.e. via the $^{16}O_{g.s.}(0^+) \longrightarrow {}^{28}Si\ (2^+)$ channel. The resulting calculations reproduced the experimental findings better than the previous cases. Even if the experimental cross sections were again overestimated, the angular position of the rainbow bump at about

$\theta_{CM} \approx 42°$ was well reproduced. Attempts in order to improve the agreement with the data were done. In particular, a reduced real component of the São Paulo potential was chosen. This procedure was proven to give a better description of the data when a positive polarization from the continuum to bound states is particularly relevant, like in reactions where the projectile break-up is important. Even if this is not the case for the ^{16}O + ^{27}Al elastic scattering, the excitation of Giant Resonances modes observed at forward angles could give rise to a similar contribution. The effect of the reduction of the real potential resulted in a better description of the data both in the elastic and inelastic case, with theoretical cross sections very close to the experimental values. The effect of the inclusion of other ^{28}Si excited states was also investigated in a very preliminary way. The 4^+ (4.617 MeV) and 0^+ (4.979 MeV) states were in particular included in the calculations. The real part of the São Paulo potential was reduced to obtain the best agreement with the data, while the imaginary one remained unchanged. The preliminary comparison showed how the inclusion of more channels in the calculation affected the elastic angular distribution in a significant way. The data were well reproduced in a wide angular range, with a good agreement for $\theta_{CM} < 40°$. Finally, the huge structures observed in the ^{27}Al excitation energy spectra at forward angles were qualitatively analysed. These can be associated with the excitation of Giant Monopole (GMR) and Quadrupole (GQR) Resonances. Such collective modes are indeed expected to appear in an energy region which is compatible with the mean energy ($E_x \approx 24$ MeV) of the observed bumps. In addition, the excitation of these giant modes in ^{27}Al were also observed in the past through (α, α') experiments. These collective states should be included in the calculations in order to investigate their effect on the overall elastic and inelastic distributions. However, the calculations are time consuming, and an accurate check in determining the strength of the coupling is necessary.

As a future perspective, a very accurate check of all the factors entering in the calculations is mandatory. In particular, the details of the code in performing the couplings among the different channels and of the models implemented for the treatment of the nucleus-nucleus interaction must be accurately analysed. This is a very important task to be fulfilled in order to improve the predictive power of the calculation and to evaluate the effect of the excitation of collective states, like the Giant Resonance modes discussed in this thesis work.

Acknowledgements

There are many people I would like to thank at the end of my PhD course, without whom these years wouldn't have been as rich as they were for me. My first thanks goes to my tutor, Prof. Francesco Cappuzzello, who guided me in this very intense period, constantly supporting me and giving me his help and his great experience through all the steps of the work, from the experimental set-up to the data analysis. An enormous thanks goes to Dr. Diana Carbone, dear friend and co-tutor of this work. We spent these three years together, in the same office, working on the same matters, sharing sunny and rainy days, but constantly helping each other. I am really grateful to her for all the effort she spent in constantly supporting me. I would like to thank also Dr. Giacomo Cuttone, director of the Laboratori Nazionali del Sud, for giving me the opportunity to work in this laboratory, Dr. Clementina Agodi, for her precious advices, and my research group: Prof. Angelo Cunsolo, Prof. Antonino Foti, Dr. Manuela Cavallaro and Dr. Marzio De Napoli.

I am particularly grateful to Prof. Jesus Lubian, who gave me the opportunity to spend a period in Niteroi and learn a little bit about the code and the calculations, and to Prof. Dirceu Pereira, who passed away last year, since he was the first to think about this research line and introduced me to it.

A special thanks goes to my colleagues and dear friends Cristina Schillaci, Mariangela Bondì, Roberta Spartà, Lorenzo Neri, Armando Puglisi, Iolanda Indelicato, Stefania Tropea, David Mascali and to all the other guys in this laboratory, too many to write down each name. Without them, I am sure I would have miss one of the best things I found in this place, their sincere friendship.

Thanks also to my brothers Salvo, Gigi, Adriano and Davide, for being always close to me, not only in our academic paths.
There are no appropriate words to thank my family at all, for giving me all the love, the support and for constantly encouraging me through these years.
My greatest thanks goes to Carmen, for always believing in me and supporting me with all the love and the patience of this world. You are the best thing I have ever had in my life.
Finally, thanks to all my friends, especially Roberto, Marco and Salvone, for being always present when I need their help and for the wonderful times spent together.

Appendix A

Deformed potentials in FRESCO

When two nuclei interact, a variety of kinds of elastic and inelastic potentials may be needed to describe their interaction. As well as the scalar nuclear attractions and scalar Coulomb repulsions, if either of the nuclei has spin $J \neq 0$ then there can be higher-order tensor interactions which couple together the spin and the orbital motion.
Inelastic potentials arise when one or both of the nuclei have permanent deformations or are vibrationally deformable. The inelastic potentials which comes from rotating a permanently deformed nucleus are described in the Hamiltonian by terms of the form:

$$V_\lambda = \sum_\mu V_\lambda(R) D^\lambda_{\mu 0} Y^\lambda_\mu(\hat{\mathbf{R}}) \tag{A.1}$$

where the form factors $V_\lambda(R)$ have both nuclear and Coulomb components for angular momentum transfers λ, called multipolarity. Their nuclear component is approximatively proportional to the derivative of the scalar potential between the two reaction partners. Simultaneous excitations of both nuclei are also possible, but have not been included in FRESCO at the moment. Vibrational excitations of a nucleus have, in general, more complicated form factors [92], but can still be expanded in the form of eq. (A.1).
Within a collective model, excitations are interpreted in terms of the deformation of the charge or mass distribution of the nucleus, therefore using deformed potentials. These can be expressed as a change in the radius at which the optical potentials are evaluated, the change depending on the relative orientations of the radius vector to the intrinsic orientation of the nucleus.

Coulomb deformation

The Coulomb potential between a charge Z and a distribution of charges z_i is expressed as:

$$V_C(\mathbf{r},\xi) = \sum_i \frac{Z z_i}{|\mathbf{r}-\mathbf{r_i}|} \tag{A.2}$$

with $\xi = \{r_i\}$.

This potential can be expanded in multipoles (A.1), obtaining:

$$V_C^{\lambda\mu}(R,\xi) = M(E_{\lambda\mu})\frac{\sqrt{4\pi}}{2\lambda+1}\frac{Z}{R^{\lambda+1}} \tag{A.3}$$

where

$$M(E_{\lambda\mu}) = \sum_i z_i r_i^{\lambda} Y_{\lambda\mu}(\hat{r_i}) \tag{A.4}$$

is the multipole electric operator.

In this scheme, the coupling potentials are the matrix elements of the operator $V_C^{\lambda\mu}(R)$ between different excited states. In the collective model, these states are characterized by their angular momentum I and projection M. From the Wigner-Eckart theorem [91]:

$$\langle I'M'|V_C^{\lambda\mu}|IM\rangle = (2I'+1)^{1/2}\langle IM\lambda\mu|I'M'\rangle\langle I'\|V_C^{\lambda}\|I\rangle \tag{A.5}$$

where $\langle IM\lambda\mu|I'M'\rangle$ is just a Clebsh-Gordan coefficient and $\langle I'\|V_C^{\lambda}\|I\rangle$ is the so called *reduced matrix element* for the operator V_C^{λ}. These are given by:

$$\langle I'\|V_C^{\lambda}(R)\|I\rangle = \langle I\|M(E_\lambda)\|I\rangle\frac{\sqrt{4\pi}e^2Z}{2\lambda+1}\begin{cases} R^{\lambda}/R_c^{2\lambda+1} & (R\le R_c) \\ 1/R^{\lambda+1} & (R>R_c)\end{cases} \tag{A.6}$$

The evaluation of $\langle I\|M(E_\lambda)\|I\rangle$ is model dependent.

- **Rotational model**

  In the framework of the rotational model:

  $$\langle I'\|M(E_\lambda)\|I\rangle = \sqrt{2I+1}\langle IK\lambda 0|I'K\rangle\langle\chi|M(E_{\lambda 0})|\chi\rangle \tag{A.7}$$

  where K is the rotational band and $\langle\chi|M(E_{\lambda 0})|\chi\rangle \equiv M_n(E\lambda)$ is the expected value of the electric operator $M(E_{\lambda 0})$ in the intrinsic state of the deformed nucleus. The only information required by FRESCO are the expectation values

$\langle\chi|M(E_{\lambda 0})|\chi\rangle$.

- **Experimentally**, $\langle I'\|M(E_\lambda)\|I\rangle$ can be directly related to the reduced transition probability $B(E\lambda;\, I \longrightarrow I')$ [92]:

$$B(E\lambda;\, I \longrightarrow I') = \frac{1}{2I+1}|\langle I'\|M(E\lambda)\|I\rangle|^2 \tag{A.8}$$

for the off-diagonal matrix elements. For quadrupole deformations, the diagonal matrix elements are related to the experimental quadrupole moment by:

$$Q_2 = \sqrt{\frac{16\pi}{5}}(2I+1)^{-1/2}\langle II20|II\rangle\langle I\|M(E_2)\|I\rangle \tag{A.9}$$

for the diagonal reduced matrix elements.

Nuclear deformations

If $U(R)$ is the potential shape to be deformed, the deformed nuclear potential can be constructed as:

$$V(\xi, \mathbf{R}) = U(R - \delta(\hat{R}')) \tag{A.10}$$

where $\hat{R}'$ are the angular coordinates (θ, ϕ) referred to the intrinsic reference frame. The function δ is normally expanded in multipoles:

$$\delta(\hat{R}') = \sum_\lambda \delta_\lambda Y_{\lambda 0}(\hat{R}') \tag{A.11}$$

If the coupling potential $V(\xi, \mathbf{R})$ is expanded in spherical harmonics, the radial multipoles $V_N^\lambda(R)$ are obtained, whose reduced matrix elements are given by:

$$\langle I'\|V_N^\lambda(R)\|I\rangle = -\frac{\langle I'\|\delta_\lambda\|I\rangle}{\sqrt{4\pi}}\frac{dU(R)}{dR} \tag{A.12}$$

with the same shape for all nuclear multipoles $\lambda > 0$.
The values of $\langle I'\|\delta_\lambda\|I\rangle$ are model dependent.

- **Rotational model**
  In the framework of the rotational model:

$$\langle I'\|\delta_\lambda\|I\rangle = \sqrt{2I+1}\langle IK\lambda 0|I'K\rangle\langle\chi|\delta_\lambda|\chi\rangle \tag{A.13}$$

where K is the projection of the angular momenta I and I' within a rotational model and $\langle\chi|\delta_\lambda|\chi\rangle$ is the expectation value of the operator $\hat{\delta_\lambda}$ in the internal state of the deformed nucleus. Even more, if the mass and charge distributions coincide:

$$\langle I'\|\delta_\lambda\|I\rangle = \frac{4\pi}{3ZeR_0^{\lambda-1}}\langle I'\|M(E_\lambda)\|I\rangle \tag{A.14}$$

where R_0 is an average radius. According to (A.7) and (A.13), the previous relation holds also for the matrix elements in the intrinsic state:

$$\langle\chi\|\delta_\lambda\|\chi\rangle = \frac{4\pi}{3ZeR_0^{\lambda-1}}\langle\chi\|M(E_\lambda)\|\chi\rangle \tag{A.15}$$

In the standard symmetric rotational model, it is not necessary to provide FRESCO with all the matrix elements above. The only information required by FRESCO are the deformation lengths δ_λ, defined as:

$$\delta_\lambda = R_0\beta_\lambda \tag{A.16}$$

where β_λ are the deformation parameters. It is important to note that within the rotational model the nuclear and Coulomb matrix elements are related by:

$$M_n(E\lambda) = \frac{3Z\beta_\lambda R^\lambda}{4\pi} \tag{A.17}$$

Therefore, within this model the knowledge of the deformation parameter and of the nuclear radius gives the fundamental information ($M_n(E\lambda)$ and δ_λ) required by FRESCO to construct the coupling interactions among the states specified in the input file.

References

[1] Stiliaris E., Bohlen H. G., Fröbrich P., Gebauer B., Kolbert D., von Oertzen W., Wilpert M., and Wilpert T. *Phys. Lett. B*, **223**(291), 1989. viii, 2, 9, 25, 26

[2] Khoa D. T., von Oertzen W., Bohlen H. G., and Nuoffer F. *Nucl. Phys. A*, **672**(387), 2000. viii, 14, 18, 26

[3] Put L. W. and Paans A. M. J. *Nucl. Phys. A*, **291**(93), 1977. viii, 19, 27

[4] Goldberg D. A., Smith S. M., and Burdzik G. F. *Phys. Rev. C*, **10**(1362), 1974. viii, 1, 9, 19, 20, 27, 28

[5] Ogoblin A. A. *et al. Phys. Rev. C*, **62**(044601), 2000. viii, 28, 29

[6] Yamaya T., Satoh O., Morita S. M., Kotajima K., Hasegawa K, Shinozuka T., and Fujioka M. *Phys. Rev. C*, **37**(2585), 1988. viii, 36

[7] Airy G. B. *Trans. Camb. Phil. Soc.*, **6**(379), 1838. 1, 7

[8] Goldberg D. A. and Smith S. M. *Phys. Rev. Lett.*, **29**(500), 1972. 1, 9, 19

[9] Goldberg D. A., Smith S. M., Pugh H. G., Roos P. G., and Wall N. S. *Phys. Rev. C*, **7** (1938), 1973. 1, 9, 20, 27

[10] Stokstad R. G., Wieland R. M., Satchler G. R., Fulmer C. B., Hensley D. C., Raman S., Rickertsen L. D., Secondnameell A. H., and Stelson P. H. *Phys. Rev. C*, **20**(655), 1976. 2, 9

[11] Bohlen H. G., Clover M. R., Ingold G., Lettau H., and von Oertzen W. *Z. Phys. A*, **308** (121), 1982.

[12] Bohlen H. G., Chen X. S., Cramer J. G., Fröbrich P., Gebauer B., Lettau H., Miczaika A., von Oertzen W., Ulrich R., and Wilpert T. *Z. Phys. A*, **322**(241), 1985. 2, 9

[13] Bohlen H. G., Stiliaris E., Gebauer B., von Oertzen W., Wilpert M., Wilpert T., Ostrowski A., Khoa D. T., Demyanova A. S., and Oglobib A. A. *Z. Phys. A*, **346**(189), 1993. 2, 9

[14] Bartnitzky G. *et al. Phys. Lett. B*, **365**(23), 1996. 2, 9

[15] Satchler G. R. *Direct Nuclear Reactions*. Oxford: Oxford University Press, 1983. 3, 11, 15, 17, 18, 19, 90, 95

[16] Chamon L. C., Carlson B. V., Gasques L. R., Pereira D., De Conti C., Alvarez M. A. G., Hussein M. S., Candido Ribeiro, Rossi E. S. Jr., and Silva C. P. *Phys. Rev. C.*, **66** (014610), 2002. 3, 30, 31, 32, 33, 95, 96

[17] Pereira D., Lubian J., Oliveira J. R. B., de Sousa D. P., and Chamon L. C. *Phys. Lett. B.*, **670**(330), 2009. 3, 30, 32, 33

[18] Cappuzzello F., Carbone D., Cavallaro M., and Cunsolo A. *MAGNEX: an innovative large acceptance spectrometer for nuclear reaction studies*. Magnets: Types, Uses and Safety. Nova Publisher Inc., New York, 1983. 3, 36, 43, 45, 50

[19] Cavallaro M. *et al. Eur. Phys. J. A*, **48**(59), 2012. 3, 50

[20] Kiss A., Mayer-Böricke C., Rogge M., Turek P., and Wiktor S. *Phys. Rev. Lett*, **37**(18), 1976. 4, 106, 108

[21] Thompson I. J. *Comput. Phys. Rep.*, **7**(167), 1988. 4, 37, 92

[22] Crawley G. M. and Garvey G. T. *Phys. Lett.*, **19**(228), 1965. 4, 37, 99, 100

[23] Brandan M. E. and Satchler G. R. *Phys. Rep.*, **285**(143), 1997. 6, 8, 19, 20, 28

[24] Brandan M. E., Hussein M. S., McVoy K. W., and Satchler G. R. *Comments Nucl. Part. Phys.*, **22**(77), 1996. 8, 21

[25] Satchler G. R. and Love W. G. *Phys. Rep.*, **55**(183), 1979. 11, 18, 31

[26] Fröbrich P. and Lipperheide R. *Theory of Nuclear Reactions*. Clarendon Press, Oxford, 1996. 12

[27] Fuller R.C. *Phys. Rev. C*, **12**(1561), 1975. 13

[28] Hussein M. S. and Mc Voy K. W. *Prog. Part. Nucl. Phys.*, **12**(103), 1984. 15

[29] Feshback H. *Theoretical Nuclear Physics vol II*. New York: Wiley-Interscience, 1992. 18

[30] Khoa D. T., von Oertzen W., and Bohlen H. G. *Phys. Rev. C*, **49**(1652), 1994. 18, 19, 21

[31] Sakuragi Y., Yahiro M., and Kamimura M. *Prog. Theor. Phys. Suppl.*, **89**(136), 1986. 19

[32] Nussenzweig H. M. *Sci. Am.*, **236**(116), 1997. 19

[33] Brandan M. E. and McVoy K. W. *Phys. Rev. C*, **55**(1362), 1997. 20, 21

[34] Khoa D. T. *et al. Phys. Rev. Lett.*, **74**(34), 1995. 21

[35] Khoa D. T., Satchler G. R., and von Oertzen W. *Phys. Rev. C*, **56**(954), 1997. 21, 22, 24, 26

[36] Kondō Y., Brandan M. E., and Satchler G. R. *Nucl. Phys. A*, **637**(175), 1998. 21

[37] Ohkubo S. and Yamashita K. *Phys. Rev. C*, **66**(021301(R)), 2002. 21

[38] Khoa D. T. and von Oertzen W. *Phys. Lett. B*, **304**(8), 1993. 21

[39] Schutz Y. (TAPS Collaboration). *Nucl. Phys. A*, **599**(97c), 1996. 22, 24

[40] Swesty F. D., Lattimer J. M., and Myra E. S. *Astrophys. J.*, **425**(195), 1994. 22

[41] Glendenning N. K. *Compact Stars: Nuclear Physics, Particle Physics and General Relativity*. Berlin: Springer, 2000. 22

[42] Khoa D. T. and von Oertzen W. *Phys. Lett. B*, **342**(6), 1995. 26

[43] Ogoblin A. A., Khoa D. T., Kondō Y., Glukhov Yu A., Dem'yanova A. S., Rozkhov M. V., Satchler G. R., and Goncharov S. A. *Phys. Rev. C*, **57**(1797), 1998. 28

[44] Szilner S., von Oertzen W., Basrak Z., Haas F., and Milin M. *Eur. Phys. J. A*, **13**(273), 2002. 28

[45] Micek S., Majka Z., Rebel H., Gils H. J., and Kewle-Nebenius H. *Nucl. Phys. A*, **435**(621), 1985. 28

[46] Nadasen A *et al. Phys. Rev. C*, **47**(674), 1993.

[47] Nadasen A *et al. Phys. Rev. C*, **52**(1894), 1995. 28

[48] Satchler G. R., Fulmer C. B., Auble R. L., Ball J. B., Bertrand F. E., Erb K. A., Gross E. E., and Hensley D. C. *Phys. Lett. B*, **128**(147), 1983. 28

[49] Khoa D. T., Satchler G. R., and von Oertzen W. *Phys. Rev. C*, **51**(2069), 1995. 28

[50] Carlson B. V. and Hirata D. *Phys. Rev. C.*, **62**(054310), 2000. 32, 96

[51] De Vries H., De Jager C. W., and De Vries C. *At. Data Nucl. Data Tables*, **36**(495), 1987. 32

[52] Nadjakov E. G., Marinova K. P., and Gangrsky Y. P. *At. Data Nucl. Data Tables*, **56** (133), 1994. 32

[53] Hussein M. S., Rego R. A., and Bertulani C. A. *Phys. Rep.*, **201**(279), 1991. 32

[54] Zuo W., Lombardo U., and Schulze H. J. *Phys. Lett. B*, **432**(241), 1998. 32

[55] Pereira D., Linares R., Oliveira J. R. B., Lubian J., Chamon L. C., Gomes P. R. S., Cunsolo A., Cappuzzello F., Cavallaro M., Carbone D., and Foti A. *Phys. Lett. B.*, **710**(426), 2012. 37

[56] Bertulani C. A. and De Conti C. *Phys. Rev. C*, **81**(064603), 2010. 40

[57] Mod. 439. Digital current integrator, Ortec, USA. 44

[58] Mod. V820. 32 channel latching scaler, CAEN S.p.A., Viareggio, Italy. 44

[59] Cunsolo A. *et al. Nucl. Instr. Meth. A*, **481**(48), 2002. 45, 46, 51, 68

[60] Rifuggiato D. *et al. J. Phys.: Conf. Ser.*, **267**(012007), 2011. 45

[61] Enge H. A. *Nucl. Instr. Meth.*, **162**(161), 1979. 45

[62] Enge H. A. *Nucl. Instr. Meth.*, **187**(1), 1981. 49

[63] Carey D. C. *Optics of Charged-Particle Beams.* Harwood, Chur, 1987. 49

[64] Cunsolo A. *et al. Nucl. Instr. Meth. A*, **484**(56), 2002. 49, 51, 52, 70

[65] Cappuzzello F., Carbone D., and Cavallaro M. *Nucl. Instr. Meth. A*, **638**(74), 2011. 50, 72, 75, 80, 82, 88

[66] Lazzaro A *et al. Nucl. Instr. Meth. A*, **570**(192), 2007. 50

[67] Lazzaro A *et al. Nucl. Instr. Meth. A*, **585**(136), 2008. 56

[68] Lazzaro A *et al. Nucl. Instr. Meth. A*, **591**(394), 2008.

[69] Lazzaro A *et al. Nucl. Instr. Meth. A*, **602**(494), 2009. 50

[70] Makino K. and Berz M. *Nucl. Instr. Meth. A*, **427**(338), 1999. 50, 70

[71] Boiano C. *et al. IEEE Trans. Nucl. Sci.*, NS-55(3563), 2008. 51

[72] Cavallaro M. *First Application of the MAGNEX spectrometer: investigation of the 19F(7Li,7Be)19O reaction at 52.2 MeV.* PhD thesis, University of Catania, 2008. 51

[73] Boiano C. *et al. IEEE Trans. Nucl. Sci.*, NS-51(4), 2004. 53

[74] Schmidt B. *Nucl. Instr. Meth. A*, **252**(579), 1986. 53

[75] Boiano C., Bassini R., Pullia A., and Pagano A. *IEEE Trans. Nucl. Sci.*, **51**(1931), 2004. 53

[76] Bordessoule M., Bartol F., Lemonnier M., and Santiard J. C. *Nucl. Instr. Meth. A*, **390** (79), 1997. 54

[77] Mod. V550. Caen readout for analogue multiplexed signals, CAEN S.p.A., Viareggio, Italy. 54

[78] Carbone D., Cappuzzello F., and Cavallaro M. *Eur. Phys. J. A*, **48**(60), 2012. 54, 60

[79] Lazzaro A. PhD thesis, University of Catania, 2003. 56, 70

[80] Lau K. and Pyrlik J. *Nucl. Instr. Meth. A*, **354**(376), 1995. 60

[81] Charpak G., Melchart G., Petersen G., and Sauli F. *Nucl. Instr. Meth.*, **167**(455), 1979. 60

[82] Knoll G. F. *Radiation Detection and Measurement*. John Wiley & Sons, Inc, 2000. 64

[83] Cappuzzello F. *et al. Nucl. Instr. Meth. A*, **621**(419), 2010. 65

[84] Berz M. and Makino K. *COSY INFINITY - Version 8.1*. Michigan State University, East Lensing, USA, 2001. 70

[85] Berz M. *AIP Conf. Proc.*, **249**(456), 1991. 70

[86] Enge H. A. *Rev. Sci. Instr.*, **35**(278), 1964. 70

[87] Lise++: Exotic beam production. URL `http://lise.nscl.msu.edu/lise.html`. 70, 81

[88] Catford W. N. Catkin. 2005. 71, 83

[89] Cavallaro M. *et al. Nucl. Instr. Meth. A*, **637**(77), 2011. 74, 75

[90] Winger J. A., Sherril B. M., and Morrissey D. J. *Nucl. Instr. Meth. B*, **70**(380), 1992. 81

[91] Sakurai J. J. *Meccanica Quantistica Moderna*. Zanichelli Editore S.p.A., 1996. 93, 116

[92] Tamura T. *Reviews of Modern Physics*, **37**(4), 1965. 94, 115, 117

[93] Raman S, Nestor C. W., and Tikkanen P. *At. Data Nucl. Data Tables*, **78**(1), 2001. 96

[94] Lubian J. *et al. Nucl. Phys. A*, **791**(24), 2007. 96, 102

[95] Goldhaber M. and Teller E. *Phys. Rev.*, **74**(1046), 1948. 108

[96] Bohr A. and Mottelson B. R. *Nuclear Structure*. World Scientific, 1999. 109